Aqueous & Non-Aqueous Phase Tracer Migration Through Differing Soil Textures.

By

Anthony Johnson B.Sc. (Hons), M.Sc.

A thesis submitted to the University of Plymouth in partial fulfilment for the degree of

DOCTOR OF PHILOSOPHY

Fluid & Environmental Modelling Group
School of Earth, Ocean and Environmental Sciences

Funded by and in Collaboration with

The National Grid Transco plc

September 2004

Author's Declaration

At no time during the registration for the degree of Doctor of Philosophy has the author been registered for any other University award.

This study was financed with the aid of a studentship from the National Grid Transco plc.

Seminars and conferences were attended throughout the period of study at which work was regularly presented. Consultation with other institutions and industrial contacts took place and several publications have been prepared.

Signed.....................................

Anthony Johnson, September 2004

Acknowledgements

Professional activities.

Publications

Johnson Roy et al., 2003: European Journal of Soil Science: A new method of characterising the void structure, fluid and pollutant transport properties of soils, using the Pore-Cor three-dimensional network.

Johnson, Mathews et al., 2002: Journal of Automation and Management Methods in Chemistry: Construction and Computer Control of an Automated Lysimeter.

Oral Presentations

Plymouth / IGER Colloquim, August 2000, University of Plymouth

UK Soil Physics Group, October 2000, Silsoe, UK

National Grid Project Update 2001, Leatherhead, Surrey, UK

Fluid Interaction Research Group, November 1999, University of Plymouth

International Conference on Environmental Flows, 2001 Dundee, UK

Poster Presentations

RSC UK Research and Development in Analytical Chemistry, April 2000, UMIST

SETAC World Conference, May 2000, Brighton

UK Soil Physics Group, October 2000, Silsoe

Institut de Recherche pour le Developpement (IRD), 2001 Ile de France, Paris

NERC Environmental Diagnostics, 2001 Outcomes

International Conference on Environmental Flows, 2001 Dundee, UK

Attended

I participated and attended regular research meetings in the School of Environmental Science, at the University of Plymouth.

BP Institute of Multi-Phase Flow, 2002, Cambridge, UK

Aqueous & Non-Aqueous Phase Tracer Migration Through Differing Soil Textures.
Anthony Johnson B.Sc. (Hons), M.Sc. & Ph.D.

Abstract

The National Grid Transco Company sponsored this project in order to promote the understanding of NAPL migration through b-horizon soils and retarding effects upon non aqueous species migration. Soil structure and texture was also studied using conservative (Bromide) and non-conservative(Phosphate) tracers. Experimental data was produced using a laboratory ½ metre scale automated lysimeter designed and constructed at Plymouth.

The tracers were compared before oil injection, to calibrate differences in soil texture, and after oil injection to detect any changes in the flow patterns caused by the oil injection. It was found that the Crediton, Sollom and Conway soils respectively offered least resistance to the tracers with the non-conservative tracer behaving much more unpredictably than the conservative tracer. After oil injection it could be seen that the oil had heavily retarded the ability of the tracers to migrate from the injection site. This retardation was identified as analogous to perturbations of the soil structure. Statistical analysis of the data showed that the experiments were all internally self consistent and visible patterns could be seen in the corrected data caused by inclusion of oil in the injection site. Methods of dispersal for the oil and tracer are suggested in the concluding chapter with references to the work of previous authors.

Development of a hazard assessment framework was facilitated by the simulation of soil structures using a pedo transfer function developed at the National Soils Resource Institute. To allow the modelling of soils the Pore-Cor software had an annealed simplex algorithm integrated into the data inversion engine to allow the simulation of 3-D soil structures using 2-D data from pedo transfer functions or experimentally derived water retention curves. An extensive sensitivity analysis upon the model highlighted limitations, due to the data set the current pedo transfer function is based upon. It was suggested that inclusion of choices of different pedo transfer functions could be used to overcome this problem. A suitable framework was derived for the identification of priority soils using a validated computer model.

Experimental data was compared to the simulated data in order to try and develop an understanding of practical upscaling of the data. The use of the "Scaleway" method is discussed in the concluding Chapter.

Index

Index of Figures

Index of Tables

1 Introduction

1.1 Aims

The aims of this project were as follows:

- To enhance the fundamental understanding of the flow of pollutants through soil at scales from 0.2 μm to 0.5m

- To obtain specific information about pollutant flow of interest to the National Grid Transco

- To establish a predictive capability for the extent of migration of insulating oil leaked from the joint bays of high tension underground cables

- To assess the effect of leaked oil on aqueous transport in soil

- To further develop the Pore-Cor void structure model for these and other purposes.

1.2 Background

Part IIA of the Environmental Protection Act 1990 requires environmental regulators to assess the risk of contaminants leaching from soils into groundwater, in order to determine their impact on controlled waters and other receptors (DETR, 1999). The legislation assumes a link between soil and groundwater chemistry, in which rainwater leaches contaminant from soil into the saturated zone. The ability to make reliable predictions of the multiphase flow of hydrocarbon fluids in natural underground reservoirs has long been the subject of intense research and development activity in the oil industry. More recently, as a result of the widespread use of oil, petroleum and other industrial organic chemicals, contamination of groundwater reservoirs has drawn the attention of hydrologists to the analysis of such flow problems. Their interest is motivated by the need to evaluate the risk to groundwater quality following a subsurface spill, (Butts and Jensen 1996). To ensure the continued supply of potable groundwater, scientists and engineers must strive to understand the processes that lead to groundwater contamination and develop methods to remediate existing problems, (Baskaran *et al.*, 1994).

Flow of water and the transport of water-borne solutes through porous materials has already been the subject of considerable study. Due to environmental considerations these processes have become increasingly significant in porous media, and an enormous range of experimental and theoretical studies have been conducted at every scale from microscopic to field and reservoir. Much work conducted at the microscopic level has aimed to characterise the fundamental mechanisms, by which movements within porous solids take place, often using molecular dynamics (Adler and Brenner 1984), (Bernadiner 1998),

1

(Sorbie and Clifford, 1991) and (Thompson and Troian, 1997). Laboratory and field studies have aimed to characterise these mechanisms at length scales ranging from less than one metre to the field scale (Biggar and Nielsen, 1976) & (Bronswijk, Hamminga, and Oostindie 1995).

However the sources of contamination are often immiscible liquids (a liquid that can not be mixed with water) located beneath the ground surface. They are commonly referred to as NAPL, non-aqueous phase liquids. The solubilities of these often toxic compounds are low, but non-zero. Once in the soil they may provide a long-term supply of contamination to local groundwater and infiltrating rainfall, (Baskaran *et al.*, 1994). Those less dense than water, referred to as light NAPL or LNAPL, tend to accumulate at the surface of the water table.

Researchers funded by the petroleum industry have already performed much work on the flow characteristics of NAPL in sandstone. Much less is known about the flow of hydrocarbons, as pollutants, within soil. Consequently much research in this area is still required, for example being able to define the spatial variability and extent of a contaminated area, thus producing better predictive capabilities. These predictive capabilities are required to assist in the pollutant migration risk assessment, and implementation of remediation techniques.

1.3 Objectives

The over arching question posed by this project was "Can pore scale modeling of soil be validated against experiments at core and 0.5m scale, and be used to produce results of national importance?". To answer this question it was necessary to derive information from several sources including experimental and modeled data sources. This was achieved by development of the areas identified in Figure 1.1. Figure 1.1 is a dependency diagram of the project objectives. The overall experimental objective was to be able to achieve reliable determinations of leachates from the soil blocks. This required the automation of a 0.5m lysimeter to achieve a higher resolution than was being achieved in comparable experiments by other workers. The need to extract large intact soil blocks also necessitated the development of a soil extraction protocol using heavy machinery and containment materials.

The experimental results were then used to analyse the predictions of the computer model. The computer model used the latest functions for modelling water retention in English and Welsh soils, combined with raw experimental data where available.
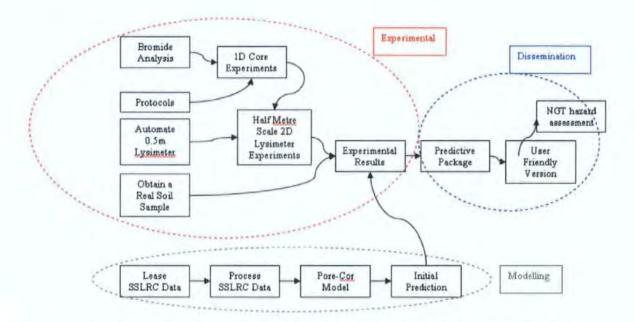
Figure 1.1   Project Flow. NGT = National Grid Transco. SSLRC = Soil Survey and Land Research Centre, University of Cranfield (formerly Soil Survey now NSRI).

Finally the initial model predictions were combined with the experimental results to validate the package. A sensitivity analysis was carried out, and the model used to enhance the environmental impact assessment of National Grid Transco (NGT, formerly the National Grid Company plc).

1.4   Structure of Thesis

Chapter 1 is concerned with a brief introduction to the topic of NAPL migration from point sources, with a description of the mechanisms involved in NAPL migration as discussed in the literature. Fundamental issues are described such as existing theory in multi-phase flow migration, porous media modelling and upscaling theory.

Chapter 2 is a detailed rationale of the project including the project framework, sample extraction and modelling.

Chapter 3 describes the methods that quantitively determined the aqueous and non aqueous tracers applied to a 0.5 m^3 soil block, in the laboratory experiments described in Chapter 4.

Chapter 4 is a description of the design and construction of an automated lysimeter used in the 3-D oil and tracer migration experiments. The experimental procedure involved the development of new experimental apparatus, and development of experimental protocols. Concurrently with the NAPL experiment, an experiment was carried out to assess the impact of the NAPL introduction on the transport path through each soil block.

Chapter 5 shows the results of the data produced by the analysis of the samples carried out in Chapter 4. Data was plotted on a specialist software package for display in a 3-D environment. This discussion involves three dimensional projections of the final NAPL distributions in the differing soil textures, and comparisons of tracer breakthrough patterns when applied to soils of differing textures.

Chapter 6 is a description of the new development in the Pore-Cor three dimensional void network model. The most significant modification is the use of a Boltzmann-annealed simplex to explore parameter space. The void structures which fit various water retention curves are then compared, and their properties used to establish a hazard assessment level, and a ranking of hazard in the event of oil leaks.

Chapter 7, the overview, is a discussion and comparison between the experimental and modelled soil data. It discusses whether any useful conclusions can be drawn from the experiments, and whether the software will be of use to field engineers dealing with NAPL migration. Suggestions for future work are also included in this chapter.

1.5 Applicability of the Project

The National Grid Transco plc (NGT) owns and operates the high-voltage electricity transmission system in England and Wales. This system consists of both overhead power lines and underground power cables for the transmission of electricity at 275kV and 400kV. The 650km of underground cables in England and Wales mainly use a paper-oil insulation system. Layers of paper surround the copper conductor and are impregnated with 'cable oil', a term used for the mixture of dodecylbenzenes (DDB) and mineral oil, commonly termed either as DDB or cable oil. Cable oil is also contained within the central oil duct. Figure 1.2 shows a cross-section of a 275kV cable. Damage to the sheathing around the cable and/or failure at the joints could cause a leakage of the cable oil into the surrounding soil. Such damage requires excavation to make repairs and removal of the soil containing the oil. The latter can be costly, particularly if the cable has to be taken out of service.

Oil Duct (cable oil)

Copper Conductor

Paper Tape Insulation impregnated with cable oil.

Aluminium Sheath

Polyethylene Oversheath
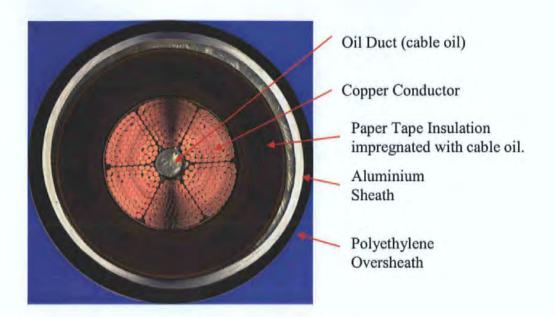
Figure 1.2 **Cross-section through a 275kV Cable.**

Although the cables are buried in the ground, they are subject to accidental damage by third parties or occasional joint failure due to ground movement, which can cause leakage of cable oil. The joints are situated in bays approximately 10m x 3m x 2m (34ft x 10ft x 6ft) in dimension, Figure 1.3.

The cables and joints are encompassed by a sand: cement backfill at a ratio of 20:1, (Cheston, 1997). This acts as a protective shield against some damage, whilst allowing adequate levels of thermal transmissivity, (Day *et al.*, 1994). A concrete slab is placed into the bay below the cable that supports the joints, see Figure 1.4. The diagram shows a cross-section of cables R, Y and B carrying the three phases of the electricity supply. When a joint is located at the lowest point in the hydraulic gradient, accumulation of cable oil may occur, acting as a sub-surface point source.
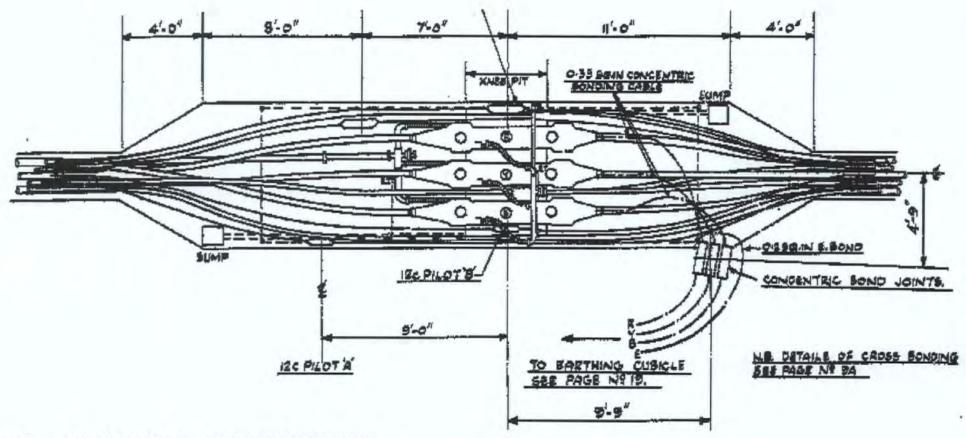
Figure 1.3   Plan of a joint bay for a self-contained oil-filled cable.
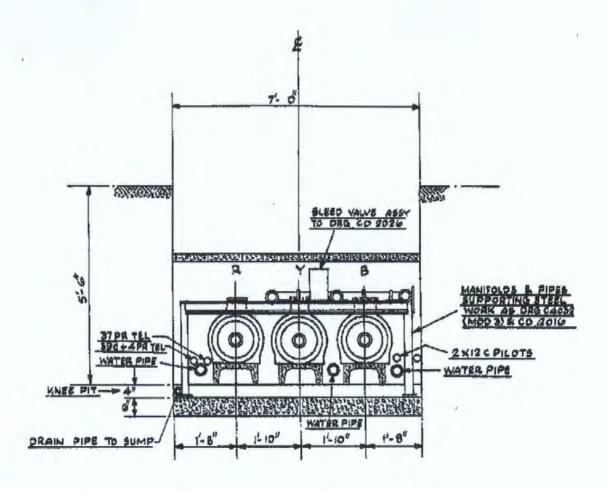
Figure 1.4   Joint bay cross-section for a self-contained oil-filled cable.

The cable oil is stored along the length of the cables in oil-feed tanks. The oil pressures within the cables range from 0 to 6.25 bar in the central oil duct. Any leaks of cable oil are therefore compensated for by an inflow from the oil tanks, that ensures an adequate level of pressure is maintained. Where a leak occurs, losses varying between 20 litres a week and 100 litres a day have been recorded.

1.6   Chemical Characterisation of Cable Oil

Linear alkylbenzenes (LABs) have been produced industrially since the 1960's as the precursor for linear alkylbenzene sulphonates, anionic surfactants most commonly used in commercial detergents. They are also used in the paper, flooring and functional fluid industries, (Gledhill, Saeger, and Trehy 1991). This production of LAB from benzene and petroleum or natural gas based feedstock results in a mixture of homologues with various alkyl chain lengths depending on the type of feedstock used. Each of the alkyl homologues consists of a mixture of isomers in which the phenyl group may be attached to any of the carbon atoms except the terminal one.

The form of linear alkylbenzene used for cable oils is commonly known as dodecylbenzene, which although not being strictly C_{12}, is composed of various lengths of

7

both linear and branched alkylbenzene chains in the C_{10} to C_{13} range, giving it the overall properties of a C_{12} LAB. Linear alkylbenzene has been in use by the NGT since 1990 and has a homologue distribution as shown in Table 1.1. It is composed of approximately 90% linear alkylbenzene and 10% branched alkylbenzene.

Alkylbenzene Chain Length	% Linear Alkylbenzene	% Branched Alkylbenzene	% Total Alkylbenzene
$<C_{10}$	0.4	0.5	0.9
C_{10}	9.0	2.6	11.6
C_{11}	32.0	2.5	34.5
C_{12}	24.7	1.3	26.0
C_{13}	24.6	0.9	25.5
C_{14}	0.9	0.4	1.3
$>C_{14}$	<0.1	0.2	0.2
Total	91.6	8.4	100.0

Table 1.1 Pirelli PG6000D cable oil alkylbenzene homologue distribution

Dodecylbenzene, the C_{12} homologue, has five possible phenyl isomers because the benzene ring may be attached to any of the carbons between C_2 and C_7. The 1-phenyl isomers are not formed (Swisher, Kaeble, and Liu 1961), due to the instability of the intermediate carbonium ion.

A chemical characterisation of DDB cable oil revealed the presence of only hydrogen and carbon, with an average atomic H/C ratio of 2.6 (Rowland, 1996).

A GC-MS (Gas Chromatography – Mass Spectrometry) analysis revealed 18 major components. The mass spectrum of each component was obtained and compared with the best-fit US National Bureau of Standards library spectra. The procedure was used to classify the 18 components into four groups, the decyl-(C_{10}), undecyl-(C_{11}), dodecyl-(C_{12}) and tridecyl-(C_{13}) benzenes. The 1-phenyl isomer was absent, as predicted by (Swisher, Kaeble, and Liu 1961). The resultant GC-MS of DDB cable oil can be seen in Figure 1.5.

The environmental distribution of high molecular weight organic compounds such as LAB's is substantially affected by their physical and chemical properties. The physical

and chemical properties of the cable oil PG6000D supplied by Pirelli are shown in Table 1.2, with properties of water for comparison.

Property	PG6000D linear alkybenzene	Water
Appearance	Clear liquid, no suspended matter	Clear liquid
Density at 20°C (kgl^{-1})	0.86	0.9978
Boiling Point ($^\circ$C)[*1]	278 - 315	100
Kinematic Viscosity (Pas^{-1} at 20°C)	8.1	1.01
Flashpoint ($^\circ$C)	150	-
Aqueous Solubility	Not miscible, 0.01mgl^{-1} 0.041 mgl^{-1}[1]	-
Vapour Pressure (25 $^\circ$C)	4.9 x 10^{-4}[1] mm Hg	23.76 mm Hg
Henry's Law Constant	7.1 x 102 torr^{-1} mol^{-1}[1]	-
Soil Partition Coefficient, K_{oc}	2.2 x 10^{4}[1]	-
Log Octanol : Water Partition Coefficient, K_{ow}	5.72 – 5.75[1]	-

Table 1.2 Comparison of the physical and chemical properties of PG6000D Linear Alkybenzene and water. Source: All PG6000D linear alkybenzene data from Shell Health, Safety & environment data sheets with the exception of: (1) (Gledhill, Saeger, and Trehy 1961). *1 Boiling range taken from European union risk assessment report, Benzene C10-13 Alkyl derivatives EINECS-No:267-051-0.
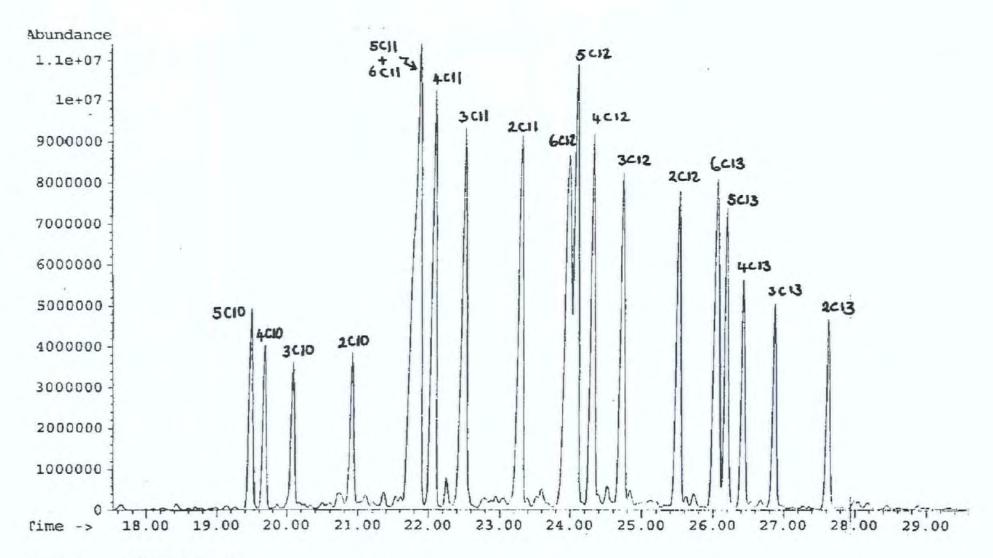
Figure 1.5   GC-MS of Cable Oil

1.7   Darcian Flow

The theory of laminar flow through homogeneous porous media is based on a classic experiment originally performed by Henry Darcy in 1856, and is shown in Figure 1.6 (Scheidegger, 1974).
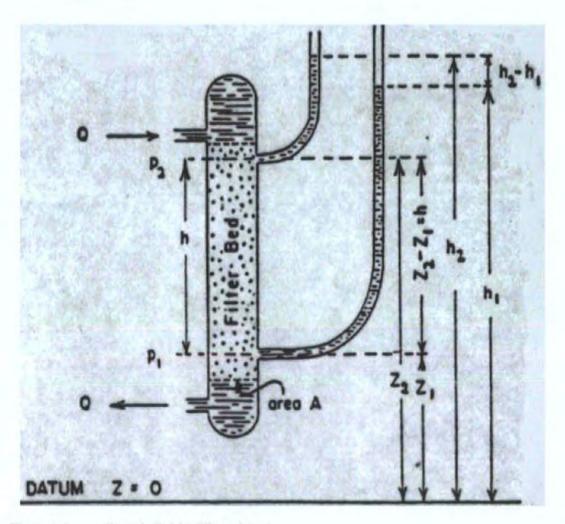
Figure 1.6   Darcy's Original Experiment

A homogeneous filter bed of height h is bounded by horizontal plane areas of equal size A. These areas are congruent so that corresponding points could be connected by vertical straight lines. The filter bed is percolated by an incompressible liquid. If open manometer tubes are attached at the upper and lower boundaries of the filter bed, the liquid rises to the heights h_2 and h_1, respectively above an arbitrary datum level. In the experiment shown above the usual term L is ignored as there is no horizontal change in the pressure heads.

The conductivity of a porous medium for single phase fluids can be expressed by the specific permeability k of the medium defined by Darcy's law, (Equation 1.1).

$$V = -(k/\mu) \ \nabla \wp = -(k/\mu)(\nabla P - \rho g)$$

<div align="right">Equation 1.1</div>

Where $\wp$ is defined by the following equation:

11

$$\wp = P + \rho g z$$

z is the distance measured vertically upward from an arbitrarily chosen datum level, P the hydrostatic pressure, ρ the fluid density, and g the acceleration due to gravity. $\wp$ is measured by a pipe called the piezometer and is indicated as the 'piezometric head' ϕ (dimension of length):

$$\phi = \wp / \rho g = (P / \rho g) + z$$

ϕ is the sum of the 'elevation head' z and the 'pressure head' $P/\rho g$. For a compressible fluid the pressure head is defined by:

$$\int_{P_0}^{P} \frac{dP}{o(P)\, g}$$

where P_0 is the hydrostatic pressure at the datum level. The difference in $\wp$ is equal to the pressure change in the fluid flowing through the porous sample. If $\wp$ is constant everywhere, then the liquid does not flow.

$V = (\delta Q / \delta A)\mathbf{n}$ is the 'filter' or Darcy velocity where $\mathbf{n}$ is the unit normal vector of the surface area δA through which there is a volume flow at the rate δQ.

The porous medium is imagined to be subdivided into a network of small blocks, and Darcy's law is applied to each block. The size of each block must be small enough to approximate V, $\wp$, k, ρ and μ with constant values within each block; but the size of each block must also be large enough for Darcy's law in its macroscopic form to apply in the block. These conditions appear to be satisfied to an acceptable degree in most practical situations, (Dullien, 1992).

In groundwater hydrology and soil mechanics, the only fluid of interest is water and, therefore, the so-called 'hydraulic conductivity' k_H defined as:

$$k_H = k\rho g / \mu$$

Darcy's law can then be written as:

$$V = -k_H \nabla \phi$$

The friction factor (f_P) as defined by equation 1.7, can be used to express the resistance of beds of particles (or fibres) to flow:

$$f_p = \overline{D_P} \nabla \wp / \rho v^2 L$$

as a function of the 'superficial' or 'particle' Reynolds number Re_p:

$$Re_p = \overline{D_p} v \rho / \mu$$

Here $\overline{D_p}$ is some effective average particle or fibre diameter, ρ is the fluid density, and L is the length of the bed in the macroscopic flow direction. Phenomenological models have proved to be particularly useful in the case of packs of fairly uniform and isometric particles or fibres. They relate the transport coefficients of the porous media to grain and packing structure.

Many other different modelling approaches for the treatment of single-phase flow have been tried, which may be broadly categorised into two types of approach. In the first approach the flow inside conduits is analysed, in the other, the flow around solid objects immersed in the fluid is considered. For low and intermediate porosities the conduit flow approach is more appropriate, whereas for very high porosities only the second approach is suitable.

Within the conduit flow approach it is useful to distinguish capillaric and statistical models. The simplest kind of capillary model consists of a bundle of straight cylindrical capillaries of uniform cross-section. Empirical capillary models have resulted in excellent correlations. Channel flow has been treated mostly in the approximation that neglects all but one velocity component, resulting in Hagen-Poiseuille type flow equations.

1.8   Water Retention Models

The relation between the soil water content and the water suction is a fundamental part of the characterisation of the hydraulic properties of a soil, commonly known as water retention. This water retention function is primarily dependent upon the texture or particle-size distribution of the soil and the structure or arrangement of the particles, (Cameron and Klute 1977).

All empirical water retention models use the Laplace equation to relate the capillary pressure p to the pore radius r_i of the i th pore as shown in equation Equation 1.9:

$$r_i = -\frac{4\gamma_i \cos\theta_i}{P}$$

Here γ is the interfacial tension between water and air, θ is the contact angle where the water meniscus touches the solid surface and P is pressure. Various approximations are implicit in the use of this equation. The contact angle and interfacial tension are assumed to have constant values (taken to be 0 degrees and 0.075 Nm^{-1} respectively), i.e. $\theta_i = \theta$ and $\gamma_i = \gamma$ for all i. All pores must be cylindrical as this geometry has a single, invariant contact angle θ. Although much work has been published on the capillary pressure in other shapes of pores (Ma, Mason, and Morrow, 1996), (Tsakiroglou and Payatakes, 1990), in a natural sample it is difficult to measure three-dimensional shape distributions (Cousin, Levitz, and Bruand, 1996). The voids are therefore explicitly or implicitly represented as cylinders, and the percolation and saturated hydraulic conductivity characteristics of each simulated void represent the actual characteristics of a real void of a possibly different shape and size (Garboczi, 1991).

The cylindrical void radius distribution f(r) is defined as:

$$f(r) = \frac{d\theta}{dr}$$

where θ is the volumetric water content. Use of this equation implies that all pores are fully accessible and that they independently experience the external applied pressure ψ. Such behaviour would be observed in a structure that contains aligned capillary tubes, Figure 1.7, in which all the tubes are open to the surface or surfaces at which pressure is applied. In these circumstances, $p_i = \psi$ for all i.
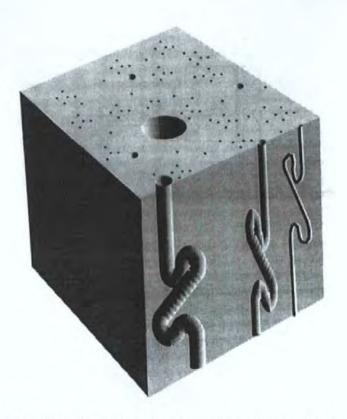
Figure 1.7   **Model of the void structure of soil comprising aligned cylindrical tubes.**

Invoking Equation 1.10 allows the pore radius distribution function f(r) to be transformed into the capillary pressure distribution function g(ψ) by the following expression:

$$g(\psi) = f(r)\frac{dr}{d\psi}$$

Equation 1.11

g(ψ) may be summed to each of a series of j experimentally determined water retention points. If we assume that the voids are in the form of aligned cylindrical tubes, and that there are N_j tubes of radius r_j and length $l\tau$, where l is the sample length and τ is the tortuosity, then

$$\sum_{j=1}^{k} g_j(\psi) = \sum_{j=1}^{k} f_j(r) = \sum_{j=1}^{k} N_j \, \pi \, r_j^2 \, l \, \tau \,.$$

Equation 1.12

To calculate the full distribution of cylinder sizes, it is necessary to estimate the low-tension asymptote. Having done this, a void model based on bundles of capillary tubes, Figure 1.7, can be constructed with properties that exactly match the water retention curve at each experimental point. However, such a model is clearly simplistic, and several other proposals for the distribution function of pore radii f(r) have been made. (Kosugi, 1994) proposed a lognormal function:

$$f(r) = \frac{(\theta_s - \theta_r) r_{max}}{(2\pi)^{1/2} \sigma (r_{max} - r)} \exp\left[\frac{\left\{\ln\left(\frac{r}{r_{max} - r}\right) - \mu\right\}^2}{2\sigma^2}\right]$$

Equation 1.13

where r_{max} is the maximum pore diameter, and θ_r is the water content at which the capillary pressure ψ is infinitely small and the soil's hydraulic conductivity is zero. In practice, however, θ_r is treated as an empirical fitting parameter, with arguable physical significance. The quantity θ_s is the water content at saturation, and because it is measured experimentally it is not treated as a fitting parameter. The mean μ and standard deviation σ are the first and second moments of the pore size distribution function.

The model is based on the assumption that the pore-size distribution of a soil is lognormal because many particle-size distributions in soils are approximately lognormal. The assumption is not supported by experimental evidence, but the model has been found to fit several sets of water retention data.

An expression relating effective saturation S_e to capillary pressure has been derived for this pore radius distribution function:

$$S_e = \frac{1}{2} \; erfc\left[\frac{\ln\{(\psi_c - \psi)/(\psi_c - \psi_0)\} - \sigma^2}{\sqrt{2}\sigma}\right] \; ,$$

Equation 1.14

where ψ_0 is the pressure at the mode of the distribution $f(\psi)$, which corresponds to the point of inflection on the water retention curve. ψ_c is the 'bubbling pressure' at which air intrusion begins. The effective saturation S_e is defined as:

$$S_e = \frac{(\theta - \theta_r)}{(\theta_s - \theta_r)}$$

Equation 1.15

Functions other than the lognormal water retention fitting function have also been widely used. Van Genuchten, 1980 proposed the function:

$$S_e = \left[\frac{1}{1 + (-\alpha\psi)^n}\right]^m$$

Equation 1.16

where α, m, n are fitting parameters.

A model proposed by Brooks and Corey (Bewersdorff *et al.*, 1983), relates the effective saturation to a power function of ψ:

$$S_e = \left(\frac{\psi_c}{\psi}\right)^{\lambda}$$

<div align="right">**Equation 1.17**</div>

where ψ_c and λ are fitting parameters. The Brooks and Corey expression has been found to be equivalent to a general fractal water retention model, (Bird, Perrier, and Rieu 2000). However, this model uses a pore-size distribution based on the first derivative of the water retention curve (Nicholl *et al.*, 1994), and therefore it implicitly includes the structure approximations exemplified by Figure 1.7. Common to all of the functions described above is that they have at most one point of inflexion and can therefore only apply to uni-modal pore size distributions.

1.8.1 Network Models

Since the publications of (Fatt, 1956), there have been many extensions of the network modelling approach. While Fatt used volumeless junctions in the networks, most models now use pore-space descriptions that include junctions characterized by an effective radius, where the junction is referred to as a pore body or a "site" of the lattice. The pore bodies are meant to correspond to the larger void spaces found in natural porous media. The narrow openings that connect adjacent pore bodies are modelled by the capillary tubes of the network model, which are called pore throats or "bonds" of the lattice.

Pore bodies are usually represented by spheres whose size distribution is representative of pore bodies found in the particular porous medium of interest, while the pore throats are usually represented by cylinders or more general conical shapes with an analogous size distribution that is characteristic of the narrow openings that connect the pore bodies. Connectedness is usually characterized by coordination number, which corresponds to the number of bonds that meet at a site.

In the intervening years between Fatt's original publication and this work, a large number of publications have appeared related to network modelling and pore-scale displacement processes. Most of these have appeared in the chemical engineering, petroleum engineering, and physics literature. These include fundamental work in computational methods; theoretical developments, usually involving aspects of percolation theory; and experimental studies, often involving etched-plate micromodels. An excellent reference

for details of various pore-scale processes, including detailed descriptions of many aspects of network models, is the text of (Dullien, 1992).

1.8.2 The Pore-Cor Model

Pore-Cor is a network model of porous media that represents the void space of samples as an array of cubic *pores* connected by cylindrical *throats*, the constricted connections between pores (Figure 1.10). The throats are of variable size, up to the size of the largest pore, or entirely absent. The geometry is further simplified by spacing the features equally in each of the x, y and z directions. Each unit cell of the structure comprises 1000 pores in a 10 x 10 x 10 array, connected by up to 3000 throats, the distance between which is termed the *pore row spacing*. The pore row spacing is used to adjust the porosity of the simulated porous media. Each array of up to 1000 pores and their connecting throats is described as a *unit cell* (Figure 1.10) and for modelling purposes the unit cell repeats infinitely in all directions. Other parameters include the *connectivity*, which is the average *pore co-ordination number* (number of connected throats per pore) and *pore* and *throat skews*, the skew of the pore and throat size distributions respectively.
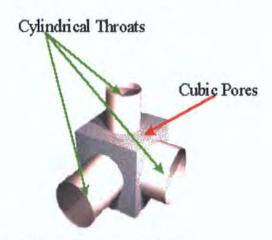
Figure 1.8   **A Pore-Cor Pore with connecting throats**

Each pore can be connected to a maximum of 6 neighbouring pores. Each pore throat pore connection constructs an arc. Pore-Cor allows fluid migration through arcs in each direction except for the +z or vertically upward axis of flow.
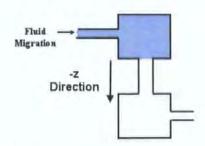
Figure 1.9   **A Pore-Throat-Pore Arc**

The unit cells connect to each other in each direction, thus generating a periodic boundary condition. Fluids, such as air as it displaces water, are intruded from the top face of the unit cell in the $-z$ direction (downwards in Figure 1.10). The periodic boundary condition causes the system into which the fluid intrudes to be a sheet of infinite width and breadth (in the x and y directions), and with thickness the same as one unit cell in the z direction.

Figure 1.10   A unit cell generated by Pore-Cor showing the simulation of Redhill 65 sand. Mercury, shown in grey, has intruded corresponding to an applied pressure sufficient to fill pore diameters up to 100 microns. Empty pores are shown brown and empty throats are shown blue. The volume of the unit cell is 4.8 mm^3.

1.8.3 Calculation of Permeability

A long-standing problem in the study of porous media has been the question of how to calculate the permeability of a solid, using knowledge of the geometry of the void space within it. The absolute permeability k of a porous solid is traditionally defined in terms of Darcy's law. With reference to a cell of the solid of unit volume, this may be written:

$$\left(\frac{dV}{dt}\right)_{cell} = -\frac{kA_{cell}\delta P_{cell}}{\mu l_{cell}}$$

Equation 1.18

where μ is the viscosity of the fluid, $(dV/dt)_{cell}$ is the volumetric flow rate across the cell, $\delta P_{cell}/l_{cell}$ is the pressure gradient across the length l_{cell} of the cell, and A_{cell} is the cross-sectional area.   Many attempts have been made to calculate k from primary parameters such as the diameters, lengths and positions of the pores and throats.   Other workers have described equations based on characteristic parameters such as porosity, the total externally-accessible surface area per unit volume of the solid, the characteristic throat diameter d_c (often loosely referred to as the characteristic pore diameter), the tortuosity, t, and the formation factor F (Matthews *et al.* 1993).

The absence of any arcs in the +z direction is equivalent to applying a non-uniform pressure gradient which causes a pressure decrease across any arc in the -z direction. This is the chief advantage of this type of calculation over those based on resistor networks (Daian and Saliba, 1991). To calculate the arc capacities, the fluid is assumed to be incompressible and flowing in a laminar, non-turbulent fashion. Such flow assumes a parabolic profile of velocity with fluid flowing through a tube taking up a parabolic velocity profile, with maximum flow rate down the centre of the tube. Integration over this profile yields the Poiseuille equation (Equation 1.19), if the flow at the walls is assumed to be zero.

$$\left(\frac{dV}{dt}\right)_{tube} = -\frac{\pi.r_{tube}^{4}.\delta P_{tube}}{8\mu l_{tube}}$$

Equation 1.19

$(dV/dt)_{tube}$ is the volume flow rate, r_{tube} the radius of the tube and $\delta P_{tube} / l_{tube}$ is the pressure gradient along the tube. Poiseuillian flow has been shown to occur for oil displacement in capillaries down to 4-μm in diameter (Templeton, 1954). If Poiseuillian flow is assumed to occur across the whole cell in the -z direction, i.e. from the top to the bottom face of the cell, then

$$\left(\frac{dV}{dt}\right)_{cell;-z} = -\frac{\pi}{8\mu}\Omega(r_{tube;z}^{4})_{cell}\frac{\delta P_{cell}}{l_{cell}}$$

Equation 1.20

Ω is an averaging operator over the whole unit cell operating on the fourth power of the individual radii $r_{tube;z}$ of all tubes lying parallel to the z axis.

Pore-Cor calculates the flow capacity, and hence hydraulic conductivity (an important but difficult feature to model), of the unit cell by using an algorithm written by Dinic (Dinic, 1970). The algorithm calculates the maximum flow capacity of the whole void network using the knowledge of the flow capacity of each pore-throat-pore connection or 'arc'. The mathematical way in which it does this is explained by (Ahuja et al., 1997). Flow is supplied from a 'super-source' to all throats at the top of the unit cell, and occurs in the -z direction, and the ±x and ±y directions.

Ω is defined such that Equation 1.18 is satisfied, and generates a term which is related to the effective Poiseuillian capacity of the cell for flow in the -z direction. Since at this stage of the calculation, all the tube lengths $l_{tube;z}$ are identical and $l_{tube;z} = l_{cell}/\beta$, where β is the

20

number of tubes in the z direction in the unit cell (in this case 10), we can include these lengths in the averaging function, so that

$$\left(\frac{dV}{dt}\right)_{cell;-z} = -\frac{\pi}{8\mu}\Omega\left(\frac{r_{tubes;z}^{4}}{\beta l_{tube;z}}\right)_{cell}\delta P$$

$$= \frac{\pi}{8\mu}\Omega\left(\frac{r_{tube;z}^{4}}{l_{tube;z}}\right)_{cell}\frac{\delta P}{\beta}$$

Equation 1.21

By considering tubes in the $\pm x$ and $\pm y$ directions as well, and comparing with the Darcy equation, Equation 1.9, it follows that

$$k = \frac{\pi}{8\beta}\Omega\left(\frac{r_{tube}^{4}}{l_{tube}}\right)_{cell}\frac{l_{cell}}{A_{cell}}$$

Equation 1.22

Parameterised Navier-Stokes equations are used to correct for the square cross-section of the pore (Matthews *et al.*, 1993), a liquid permeability may be calculated (Schlicting, 1979). The wide range of void sizes in the soil samples generated arc flow capacities over a range of 12 orders of magnitude, and to handle this, the Dinic algorithm was converted from its original integer arithmetic to real arithmetic.

The fit to a particular water retention characteristic does not produce a unique structure. This is partly due to the small size and simplicity of the unit cell. It also arises from the fact that the amount of information contained within a water retention curve alone is insufficient to produce unique solutions (Crawford, Matsui, and Young 1995), (Bird and Dexter 1997). As a result of the non-uniqueness of the unit cell structure, the predicted flow capacity is also not unique. It is therefore necessary to validate the model by a sensitivity analysis, as described in Chapter 6.

1.8.3.1 Void Space Modelling

A percolation algorithm, which assumes intrusion is controlled by the Washburn/Laplace throat diameters, is used to model air intrusion displacing water. Throat lengths are equal to the distance between pore edges, determined by pore size and pore row spacing. Pore row spacing is adjusted, after the pores and throats have been positioned, to model the experimental porosity. Throat length has little effect on simulated intrusion, and therefore the porosity can be modelled independently of air intrusion. Throat size distribution is log/linear, that is equally spaced over a logarithmic scale (Figure 1.11).
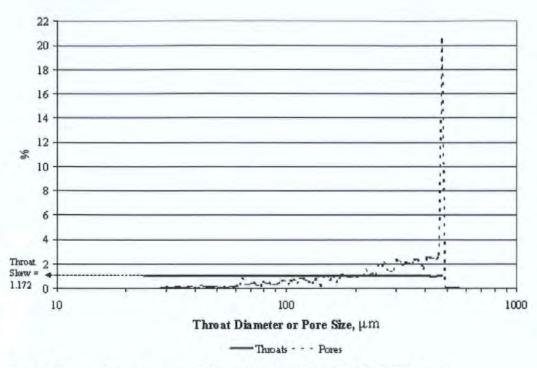
Figure 1.11   **Example pore and throat size distribution for Redhill 65 sand.**

The adjustable parameters are throat diameter range, skew of throat size distribution, pore:throat correlation and pore row spacing. Throat diameter range is calculated from the mercury intrusion pressure range limits and there are 100 throat diameters in each distribution. The pore size distribution, generated from the throat size distribution, may be checked against electron micrographs of the sample. Throat skew is defined as the percentage of the smallest size throats in the log/linear distribution. Figure 1.11 shows a skew of approximately 1% which, with the 99 other sizes, results in an almost uniform distribution. The throats are randomly positioned within the unit cell, following which pores are assigned to the nodes. The random positioning of the throats introduces are degree of randomness to the pore size distribution, which can be seen in the jagged distribution in Figure 1.11. The pore size distribution shown also features a pore skew of 1.2. The pore size distribution is multiplied up by this factor so the smallest pore size of 25 μm, greater than the smallest throat size of 20 μm and then any pore whose size is larger then the original maximum of the range is truncated to this maximum pore size. This results in a frequency peak at the maximum of the pore size distribution, but enables larger porosities to be simulated.

Simulated mercury injection takes place normal to the xy plane of the unit cell at $z = l_{cell}$ in the $-z$ direction, where l_{cell} is the length of the unit cell. An invasion percolation method is used to calculate the fraction of the pore volume occupied at each static pressure (Spearing, M. C. and Matthews, G. P., 1991).

The gradient of the intrusion curve at the point of inflection is governed by connectivity. For simplicity the high curvature regions of the curve above and below the point of inflection are referred to as the upper and lower shoulders respectively. Increasing connectivity shifts the curve to higher throat diameters and makes the upper shoulder too high as a result of increasing the gradient at the point of inflection, Figure 1.12. Breakthrough occurs at larger throat diameters, or lower pressures, because of the increase in routes through the network. This can be countered by increasing the throat skew, but resulting intrusion curves will still possess an exaggeratedly steep upper shoulder.
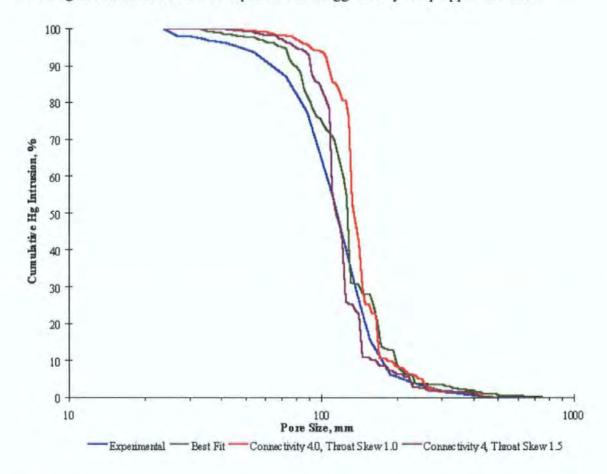
Figure 1.12   Changing connectivity and throat skew.

1.8.3.2 Correlations in Void Size Distributions

The sizes of adjacent pores and throats may affect intrusion and hysteresis. It has been shown that pore:throat size correlation has a weak effect on intrusion, while pore:throat correlation combined with pore:pore correlation has a strong effect (Burganos and Payatakes 1992). It has also been observed that correlation can decrease shielding effects described in the previous section. Figure 1.13 shows the effects of the pore:throat size ratio on hysteresis.
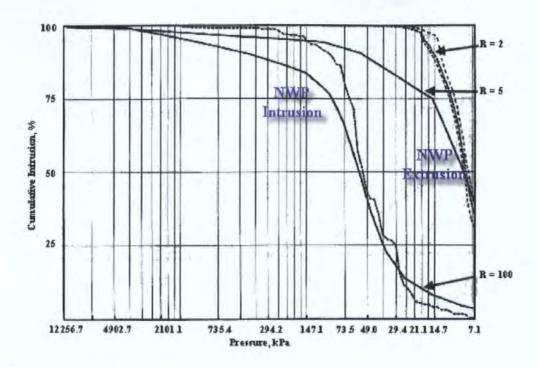
Figure 1.13 Effect on hysteresis of changing the pore:throat size ratio, R. Experimental non-wetting phase(NWP) intrusion and extrusion is shown by the solid lines and modelled results by the dashed lines.

The networks used in Pore-Cor are correlated by setting the size of each pore equal to the diameter of the largest throat entering it. Other types of correlation have also been simulated (Mathews, T. J. et al., 1997; Matthews, G. P. et al., 1995), and the work conducted here extends previous studies into the effects of correlations in the distributions of different sized pores in real porous materials. Figure 1.13 is an example taken from the earlier work. It also provides an indication of the optimum level of fit which could be achieved between experimental and simulated non-wetting phase intrusion, before the incorporation of the simplex algorithm described later in this work.

1.8.3.3 Dead-end Pores

Dead-end, or 'ink bottle', pores, that is pores connected to just one throat, also cause structural hysteresis. A mercury-filled dead end pore can only empty by surface flow of wetting phase along the walls and non-wetting phase withdrawal along the middle of the throat.

1.8.3.4 Tortuosity

For a particle moving through a porous material, for example an ion passing through a membrane, tortuosity is defined as the ratio of the path length taken by a particle to the length of the porous sample. Frequently tortuosity has been assumed to be responsible for discrepancies between predictions and observed behaviour in various porous systems, and as such tends to have been employed largely as a fitting parameter.

24

Pore-Cor allows the calculation of the tortuosity of simulated porous media. This is achieved by simulating 50 weighted random walks, from top to bottom, through the unit cell. A simulated particle is assumed to enter the unit cell at a random location on the top surface. At each pore a random throat is selected, with the choice being weighted by a factor of r^2/l, where r is throat radius and l is throat length. Pore-Cor returns the median value of all the random walks as well as the inter-quartile range.

1.8.4 Other Modelling Approaches

1.8.4.1 Fractal Models

"Fractal Geometry plays two roles. It is the geometry of deterministic chaos and it can also describe the geometry of mountains, clouds and galaxies." Benoit Mandelbrot 1975.

The term "fractal" (from the Latin fractus, meaning an irregular surface) was coined by Benoit Mandelbrot in 1975.

Fractals are non-regular geometric shapes that have the same degree of non-regularity on all scales. The fractal approach to modelling void space in porous media has enjoyed considerable success in recent years (Rappoldt, 1990), (Bird, Bartoli, and Dexter 1996) and (Perrier, Bird, and Rieu 1999).The fractal approach has some favour due to "relatively small numbers of parameters that can define a random fractal porous medium of great complexity and rich structure" Sukop et al., 2001.(Sukop, Perfect, et al. 2001) Figure 1.14 a, b & c are illustrations of the type of structure encountered using different fractal algorithms. Figure 1.14 a) is the classic Sierpinski carpet generated to the 4th iteration.

Increased complexity can be achieved by algorithms which modify the distribution of the pores and solid fractions of the materials.
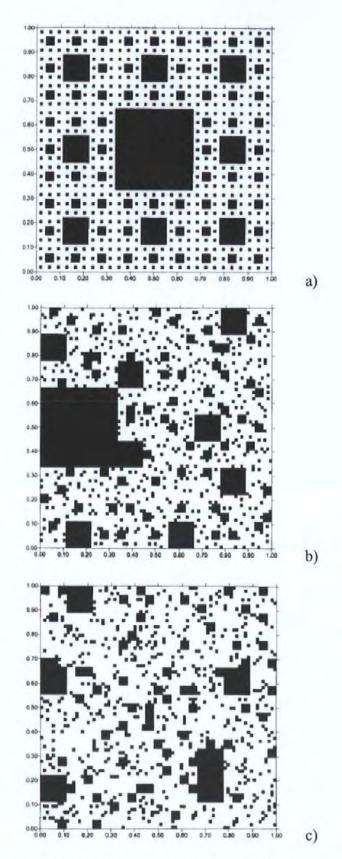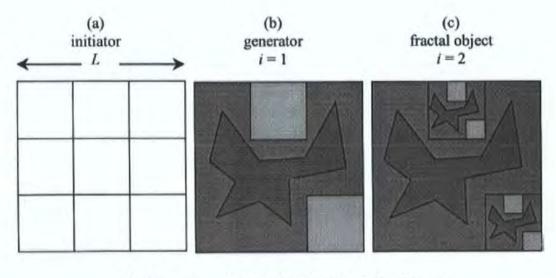
Figure 1.14   Evolution of a Sierpinski carpet, a) generated to the 4th iteration, b) 4th generation Randomized Carpet using the Homogenous algorithm & c) 4th generation using the heterogeneous algorithm (Sukop, Perfect, *et al.* 2001). Pores are indicated by black with white representing the solid fraction of the structure.

Criticisms of the fractal approach include the way that connectivity of the pores is ignored.

(Sukop *et al.,* 2001) circumvented this problem by the computation of retention in

simulated realizations of known fractal porous media using a method that would account for pore connectivity (Perrier, Mullon et al.,1995).

Perrier, Bird et al., 1999 developed the pore-solid fractal (PSF) approach to modelling soil structures. The model is generated in Euclidean space, in 3 basic steps;

1. A defined region of linear size L divided into N equal parts.
2. Generator b divides the N parts into two sets of Nz (light grey) and $N(1-z)$ (dark grey) subregions, determines the location of the Nz subregions also defining the pattern of the $N(1-z)$ subregions.
3. Nz are replaced by a reduced replicate of the generator.

(a)	(b)	(c)
initiator	generator	fractal object
L	$i = 1$	$i = 2$

$d = 2, n = 3, z = 2/9, D = \log2/\log3 = 0.631, Nz = 2$

Figure 1.15   Basic construction of fractal object. Perrier, Bird, et al. 1999.

Development through the iterations constructs a soil model that can then be realistically analysed for properties such as bulk density or porosity. Mass fractals relate the term mass to be the pore or solid volume (assuming uniform density of the solid phase). The model developed in the study by Perrier, Bird et al., 1999 however was found not to be a true mass fractal as it did not have the specific scaling factor of

$$B(r) \alpha \, r^{-D}$$

Here $B(r)$ is number of boxes of size r needed to cover whilst scaling at r^{-D} where D is the fractal of dimension D. The approach employed by Perrier, Bird et al., 1999 extended the functionality of the model to the analysis of the solid phase of the model which was discounted by earlier works.

Perrier, Bird *et al.,* 1999 describe the use of many fractal models as limited in the scope of soil research, specifically citing the Sierpinski Carpet, the Menger Sponge, and the earlier fractal cube as discussed in a review by Rieu and Perrier, 1997. The mass fractals as proposed in the Perrier, Bird *et al.,* 1999 publication represented a step forward by allowing the modelling of more than pore-solid interface, by using a geometric frame to closely associate the pore-solid phase. The problem identified by Perrier *et al* is that a true fractal structure must be iterated *ad infinitum.* This causes the fractal pores or solids to vanish completely from their complementary models. This therefore does not allow the possibility of the modelling of a two-phase medium. An attempt to overcome this was to use two power laws to span the scale range to allow for lower range cut off or infinite iterations.

A quirk in the PSF model allows the simulation of soil structure porosity by using generated parameter values. The porosity of the improved models limiting value function yields a total porosity depending upon the generated parameter values. The parameter values are calculated by the ratio of pore to solid maintained after each iteration.

A key feature when modelling the soil structure using the fractal approach is to maintain a realistic connectivity. For example Figure 1.16 illustrates a mass fractal generated by Perrier that is excessively connected to realistically represent a soil structure. On the other hand the Sierpinski carpets as shown in Figure 1.14 lack any realistically interpore connectivity. A realistic soil structure must be generated by establishing good soil pore structure with a realistic degree of interconnectivity in between each of the pore structures.

Figure 1.16   representation of a random realization of the fractal cube considered by Rieu and Sposito (1991), fragmented by a Voronoï tessellation. In this example the fractal set is associated to the solid phase.

1.8.4.2   Wavelet Analysis

Wavelets are a mathematical framework for hierarchically decomposing signals, images and more geometrically complex data into components that represent information in different scales.   Wavelet theory was developed during the 1970's by the adaptation of time series analysis in order to assist engineers in their quantitative spacial predictions.

Unlike Fourier representations, wavelets are well suited for representing localized events, as the basis functions are themselves local. Wavelet transforms are particularly useful for detecting changes of finite (but possibly unknown) duration, such as edges, transients, etc. They are a useful tool when attempting to analyze data sets for features or the detection of abnormalities in the data.
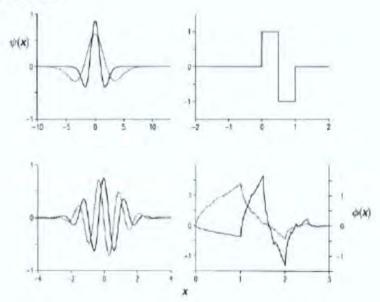
Figure 1.17   Wavelet Functions, Top Left: Mexican Hat with two dilations, Bottom left:Morlet wavelet, composing complex real (solid) and imaginary (dashed) parts, Top right: Haar Wavelet, a first difference operator and Daubechie's wavelet (solid) and associated scaling function lark, 1999.

A wavelet function must have three properties:

The mean is zero,

$$\int_{-\infty}^{\infty} \psi(x)dx = 0,$$

<div align="right">

Equation 1.24
</div>

The squared norm is 1, i.e.

$$\int |\psi(x)|^2 \, dx = 1$$

<div align="right">

Equation 1.25
</div>

The third property of the wavelet will be that of rapid damping so it only operates on a local level. This characteristic is also known as compact support. Condition two means that the wavelet only takes non-zero values over a narrow interval.   This property is

illustrated by the so-called 'Mexican hat' wavelet function in Figure 1.18 a. The wavelet transform is an integral transform, that is to say a wavelet coefficient is obtained by integrating the product of a wavelet with the data. It is clear that a wavelet coefficient, because of the compact support of the wavelet, will only respond to the data over a finite interval, and so gives a localized description of the data's variability.

In order to analyse data over a transect it is necessary to shift the wavelet (translate it) as in Figure 1.18 b. Furthermore, the scale at which a wavelet coefficient describes the data may be changed by shrinking or dilating the wavelet function Figure 1.18 c. A basic wavelet function may be obtained with the following equation:

$$\psi_{\lambda,x}(u) = \frac{1}{\sqrt{\lambda}} \psi\left(\frac{u-x}{\lambda}\right), \qquad \lambda > 0, \ x \in \Re,$$

Equation 1.26

Function $\psi_{(\lambda,x)}$ using Equation 1.26 where $\Re$ denotes a set of real numbers, the parameter λ is the 'scale parameter' of the wavelet and controls dilation. The parameter x determines the location of the wavelet.
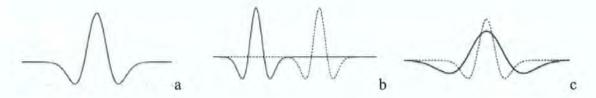
Figure 1.18   **Wavelets Produced by Wavelet Equation. a) 'Mexican Hat' wavelet, b) translation and c) dilation.**

More recently Lark, 2001 has shown how the location of changes in variance may be detected statistically using wavelet coefficients. Wavelet analysis requires substantial numbers of regularly sampled data. This inevitably limits the scope for its application to environmental variables which must be measured directly by field sampling and laboratory analysis. For this reason Lark, 2001 suggested that wavelet analysis might be most useful for the analysis of cheaper data obtained using sensors, excluding it from further work here.

1.9   Pedo-Transfer Functions.

It is possible, but time consuming, to measure the hydraulic properties of soil from small granules up to field scale. For larger areas or to save time, pedotransfer functions are used (Wopereis *et al.*, 1993). These are generally empirical relationships that allow the hydraulic properties of a given soil to be predicted from more widely available data, usually texture (percent sand, silt and clay), bulk density and organic carbon (OC) content.

Pedo-transfer functions may be used to predict properties, e.g., water content at a particular matric potential (e.g., Pidgeon, 1972; van den Berg et al., 1997) or available water capacity (e.g. Batjes, 1996). Other pedo transfer functions have been developed to predict the parameters of equations, such as those of (Brooks and Corey, 1964) and (van Genuchten, 1980), which describe the water-release curve, e.g. (Rawls, Brakensiek, and Saxton 1993). The latter type of pedo-transfer function is more suitable for modelling purposes as they describe the whole of the water release curve.

There are two main types of pedo-transfer function (PTF), "class" and "continuous". A class PTF is used to predict the hydraulic properties of a textural class, for example, silty clay loam, or sandy clay. Wosten, Finke, and Jansen (1995) describe class PTFs as "cheap and easy to use" because only the textural class has to be determined. However, they have limitations "because the approach only provides one average hydraulic characteristic for each texture class", even though there may be a considerable range of characteristics within a single textural class.

A continuous PTF is used to predict the soil hydraulic characteristics from other, more readily available data. Wosten, Finke, and Jansen (1995) make the key point that the indirect methods (i.e., PTFs) cannot exist without the direct methods (i.e., field sampling/lab measurements) because only direct measurements create the database from which indirect methods are derived. This is a strong argument for the development of more physically based, rather than empirical, methods to derive soil hydraulic properties on a large scale. However, these are still at an early stage of development.

Water release curves are also affected by soil structure, and often by mineralogy. The strong weathering and leaching processes in large areas of the tropics cause loss of Ca, Mg, Na and K, and accumulation of Fe and Al. The processes tend to create particular mineralogies and soil structure, which are less common in temperate regions. The weathering processes have been going on for long periods of time, uninterrupted by ice ages. In temperate regions, glacial action over large areas in the Quaternary period will have contributed to the larger amounts of silty soils. As mineralogy is not normally taken into account in PTFs, a third possible type of PTF is suggested: a "soil class" PTF. This could be derived for a major soil class on the basis that within a major soil class or group, the range of structure, mineralogy and texture might be expected to be narrower than for soils as a whole. This may be an over simplification in the case of soils that show marked changes in texture with depth, particularly cambisols.

Most of the pedo-transfer functions to predict Brooks and Corey (BC) or van Genuchten (vG) parameters have been developed using extensive databases for the soils of temperate regions. Van den Berg et al. (1997) noted that the often empirical relationships to predict available water capacity derived for the soils of temperate regions "appeared to be inadequate for Ferralsols and related soils, which are dominated by low activity clays". They derived a PTF specifically for Ferralsols and related soils. Only this PTF, and those of Tomasella and Hodnett, (1998) and Tomasella et al., (2000) for Brazilian soils, have been derived exclusively using data for tropical soils. Regardless of the methodology used to develop it, any pedo-transfer function is likely to give less accurate or possibly even very poor predictions if used outside the range of soils from whose data they were derived. The pedo-transfer function of Rawls, Brakensiek, and Logsdon (1982) is valid for soils with a clay content of 5–60% and a sand content of 5–70%, but some kaolinitic tropical soils, particularly Ferralsols, can have clay contents of 70–90%. This might suggest, from a temperate soils viewpoint, that they are "heavy" clays, with a low permeability and a moderate to high available water capacity. However, most have a low bulk density (0.9 – 1.2 g/cm^3), are highly permeable because of their microaggregated structure, and have a low available water capacity.

For high clay content Amazonian oxisols, the very low available water capacity was confirmed by field soil moisture observations by (Hodnett et al., 1995) who warned that PTFs derived for the soils of temperate regions should be applied with great caution to these tropical soils. (Tomasella et al., 2000) showed that a PTF derived using solely Brazilian soil data and tested on an independent data set of Brazilian soils, gave markedly better predictions than PTFs derived using temperate soils data. Performance was evaluated using the approach described by (Tietje, 1996).

Within the test data set, some of the data were outside the range of textural validity of the "temperate soil" PTFs tested, but the new PTF outperformed the former, even when tested within the range of validity of the data. The evaluation of a PTF using data that fall outside its range of validity may seem inappropriate. However, models have been developed which require soil water-release data worldwide, but in the near absence of PTFs developed for tropical soils, there is little alternative but to apply established temperate soil PTFs, regardless of their validity or suitability. It is important, therefore, to evaluate how well the PTFs will perform when applied outside the range of the data that were used to derive them. The silt content of the soils in the Brazilian data set used by (Tomasella et al., 2000)

were very low, when compared to that of temperate soils, and it was noted that the prediction errors for the temperate PTFs decreased with increasing silt content, while those of the "tropical" PTF increased. The better predictions of the Brazilian soil PTF even within the range of textural validity of the temperate PTFs also suggest that there may be differences between temperate and tropical soils caused by factors other than texture.

This thesis utilised a pedo-transfer function (PTF) developed at the National Soils Resources Institute (NSRI), UK (Mayr and Jarvis, 1999). The PTF is based on a least squares regression analysis of a very large data set of English and Welsh soils.

$$\theta = \theta_s (\psi/a)^{-1/b} \qquad \theta < \theta_i$$

Equation 1.27

$$\theta = \theta_s - \frac{\theta_s \psi^2 (1 - \theta_i/\theta_s)}{a^2 (\theta_i/\theta_s)^{-2b}} \qquad \theta \geq \theta_i$$

Equation 1.28

θ represents soil water content, ψ soil water pressure head, θs soil water content at saturation and a, b are fitting parameters. The soils represented by this PTF are those of relevance to NGC as the power distribution hardware found in this country transects the soils that are used to derive this equation.

1.10 Migration at the Pore Scale

The research undertaken in this project is partly concerned with relative permeability (i.e. how does permeability / conductivity in one fluid vary in the presence of another fluid).

Dullien (1992) has investigated the multiphase flow of immiscible fluids in porous media. A large proportion of this work has been concerned with the traditional three-phase movement, with all experimental results cited referring to changes in permeability with water saturation. This is shown diagrammatically in Figure 1.19. Figure 1.17 illustrates the different flow patterns encountered by different sequential introduction of immiscible fluids into the same flow cell. Flow regimes of immiscible fluids illustrated are

a) Two zone flow where there is strong segregation between the 2 fluids as they are introduced at different angles.

b) Fluid II introduced at 3 points form surface films around the structures, with the first fluid passing around. Fluid II is flowing in only sectors where surface films are closest together, where fluid I has lower disruptive capability.

c) Fluid II is introduced between two streams of Fluid I. Fluid II is contained within the streams of fluid I and flows straight to sink without interacting with the flow cell.

d) Fluid I and fluid II are introduced into the same flow path and a chaotic mixing flow takes place as neither fluid can gain an area of preferential flow from the other.

The research in this project is concerned with changes in the permeability of water in an oil saturated, pre-wetted sample, (as shown in Figure 1.20), rather than the changes in permeability through water saturation. Water NAPL interaction flow during the experimental trials was monitored using Bromide and Phosphate tracers.
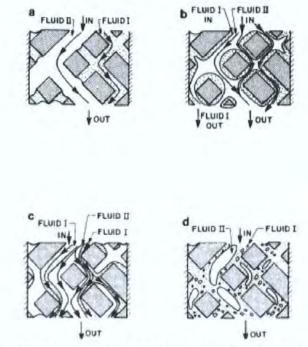
Figure 1.19   **Two-dimensional representation of three-dimensional co-current steady two-phase flow in porous media, (Dullien, 1992).**

Darcy's law can also be adapted for steady and unsteady multiphase flow in porous media, (Dullien, 1998). It has been widely assumed in the literature that the effective permeabilities in a sample of the porous medium do not depend on the viscosities of the fluids. The idea behind this assumption is that the two fluids flow in separate channels, similar to the case of Figure 1.19 a, and therefore the viscosity of Fluid I has no effect on the flow of Fluid II, and vice versa.

34
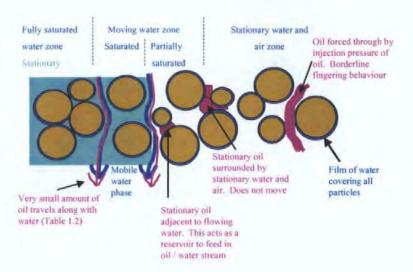
Figure 1.20 Schematic diagram showing the possible oil flow movements within sand and soil depending on the degree of water saturation. Soil shown in brown, moving oil shown in dark blue, stationary water shown in light blue, oil shown in purple and remaining colourless area represents air.

In certain instances a gas phase may also be present in immiscible displacement in porous media. One such instance involves the mobilisation of oil blobs that are surrounded by water and trapped in the pores by capillary forces. Trapping of oil blobs happens regularly in a water wet oil reservoir after water flooding and it can also happen in the soil in the course of attempted cleanup operations, (Dullien 1992).

It was demonstrated that if the water is drained from a porous medium containing trapped residual oil, the oil blobs start spreading spontaneously immediately after they have been contacted by the air, Figure 1.21. The phenomenon of spreading oil blobs has resulted in the recovery of a very high percentage of residual oil, because films thus formed drain under the influence of gravity on the surface of the thick water films and oil is produced at the low end of this medium. This work is described in more detail in the publications by Dullien.
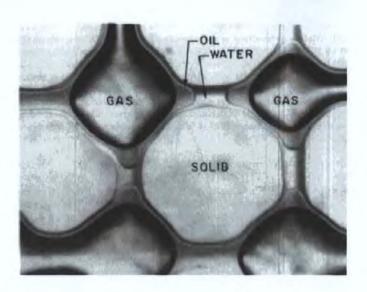
Figure 1.21 Spontaneous spreading of NAPL blobs on the surface on connate water in a capillary micromodel after being contacted by air, from Dullien (1998).

(Lenormand, Touboul, and Zarcone 1988) determined that immiscible displacements in porous media with both capillary and viscous effects could be characterised by two dimensionless numbers, the viscosity ratio $M = \mu_2/\mu_1$ and the capillary number C:

$$C = \frac{q\mu_2}{A\gamma \cos\theta}$$

<div align="right">Equation 1.29</div>

where q is the flow rate, μ_1 is the viscosity of the wetting fluid i.e. water, μ_2 is the viscosity of the non-wetting fluid, A is the cross-sectional area of the sample, γ is the interfacial tension and θ is the contact angle. They describe how for certain values of C and M, either viscous or capillary forces dominate and displacement takes one of the basic forms: (a) viscous fingering, (b) capillary fingering, or (c) stable displacement.

By applying the equations above, it is possible to determine values for log C and log M. The log M value uses the bulk viscosities of cable oil and water, from Table 1.2, 8.1×10^{-3} Pa s^{-1} and 1.01×10^{-3} Pa s^{-1} respectively. This results in a log M value of 0.84. In order to calculate the capillary number, a number of assumptions have been made. The first is the value of q, the flow rate of oil. The interfacial tension is assumed to be approximately 0.1Nm^{-1} and θ is believed to be 140° (assumed to be equivalent to mercury against air in sandstone). Using these assumptions a log C value of -5.1 is calculated for cable oil against water. If however, the contact angle is closer to 90° then the log C will be higher than -5.1. By doing similar calculations for cable oil against air, a log M value of 2.58 can be obtained.

Using the diagram in Figure 1.22 it is possible to determine the region in which cable oil infiltrating from a typically unsaturated soil would fall. Based on the value of the viscosity ratio M, three zones can be distinguished. Zone I, at very low M, where viscous forces injected in the non-wetting fluid are negligible in comparison with viscous forces in the wetting fluid. Zone II is the transition zone, where the viscous pressure drops in both fluids and plays a significant role. Zone III at very large M, where the viscous pressure drop in the wetting fluid is negligible.

The flow in this study is in the transition zone of Figure 1.22, intermediately between flow controlled by viscous and capillary forces. Although there seems to be a stable front separating the liquids, the region behind the front is not saturated with the more viscous fluid. Instead, it comprises a complex network of preferential flow routes. In addition, there is the possibility that the front will extend by viscous or capillary fingering at some positions. The behaviour of the oil against both water and oil in the two-phase system, is on the borderline between fingering and stable front saturation, and can be termed 'partial fingering'.
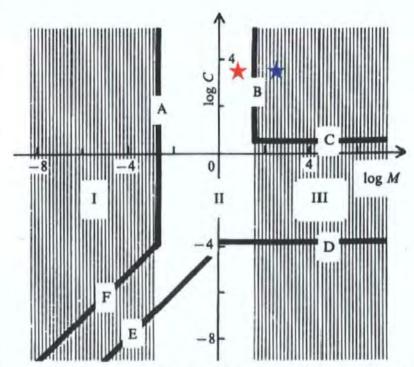
Figure 1.22   Schematic representation of the three zones where the different viscous forces are acting, (adapted from Lenormand *et al.* (1988)). The red star represents oil displacing water and the blue star represents oil displacing air.

(Lenormand, Touboul, and Zarcone 1988) studied the flow using simulations on two-dimensional networks, comprising 25 x 25 nodes and 100 x 100 nodes. Arbitrary void size distributions and connectivities were used. They simulated the two-phase flow of various

combinations of liquids. These are shown in Figure 1.23, which also shows the respective values of log C and log M.

(a)   (b)   (c)   (d)   (e)
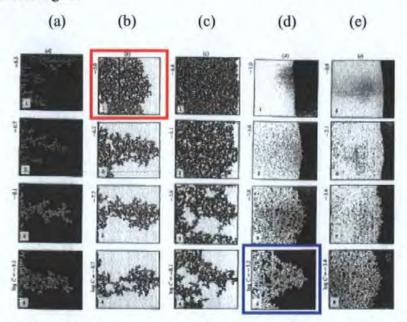
Figure 1.23 (a) Air (white) displacing a very viscous oil at various C at log M = -4.7: from viscous fingering (1) to capillary fingering (4). (b) Mercury (black) displacing hexane at log M = 0.7. (c) Mercury (black) displacing air at log M = 1.9. (d) Glucose solutions (white) displacing oil at log M = 2.0 and various C: from stable displacement towards capillary fingering. (e) Glucose solution (white) displacing oil at log M = 2.9 and various C: from stable displacement towards capillary fingering, from Lenormand et al. (1988).

The red highlighted cell most closely relates to the calculated C and M values for oil against water in this study and the blue cell represents oil against air.

Despite many years of research and the fact that the microscopic laws of fluid dynamics are well known, macroscopic multiphase flow in porous media is still difficult to predict (Hilfer, 1998). Microscopic and macroscopic descriptions of multiphase fluid flow in porous media differ considerably from each other and both have their characteristic problems, (Dullien, 1992). Hilfer, (1998) states that 'a microscopic description fails because it is generally impossible and not interesting to known the detailed microstructure and flow patterns on the pore scale'.

Three phase flow in a porous medium is very difficult to predict. There are no measurements of the contact angle of oil on wetted solid, but it can be reasonably assumed to be closer to 90° than, say, mercury on sandstone (130°). If the angle is assumed to be, say, 120° this makes little difference to the value of log C. It changes from –5.1 to –5.5 (see Section 1.5 for the calculation of the equation) and therefore the general predicted behaviour is virtually the same.

It is also worthwhile to calculate the dimensionless Reynolds number R, the ratio between inertial and viscous forces in a channel by using Equation 1.30,

$$R = \frac{\rho V d}{\mu}$$

<div align="right">**Equation 1.30**</div>

where V is the calculation of the flow velocity and d is the diameter of the channel (or capillary). For this study, R was calculated to be of the order of 10^{-8}, which represents creeping flow. These two calculations are assumed to represent the flow movement, and this will be tested during the investigation. However, it must be noted that the scale of the experiments conducted throughout this study are at least three orders of magnitude greater than pore scale, which these calculations represent. There are also major differences between the simulated flows in two dimensions, and the actual flow in the complex three-dimensional networks of natural samples.

1.11 Upscaling Methods and Approaches

Figure 1.24 illustrates the modelling and experimental domains encountered in porous media. On the horizontal axis are the general approaches categorized as the use of purely mathematical equations towards the left of the diagram, with purely experimental methods towards the right of the diagram. The vertical axis shows the scale of system size, ranging from the molecular level ~ 10 nm to reservoir scale ~ 10 km. Below the continuum limit it is essential to consider the explicit void structures within the porous medium in order to explain the behaviour of fluids within the substance. Above the continuum limit, parameters which assume an effectively homogenous structure may be used, such as permeability, and these parameters may be calculated by theories based on a continuum assumption, such as effective medium theory. The waviness of the continuum limit represents the uncertainty of its exact position.
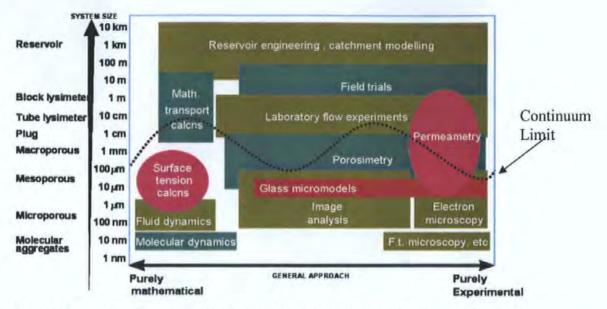
Figure 1.24   Upscaling and applicability of Pore-Cor across the Continuum Threshold.

Primary inputs into any porous network model are the physical descriptions of the media, which are typically in the form of physical data, such as porosity and permeability. Models are commonly built as realizations constrained to data of different types and scales. These models are often generated at high levels of resolution because it is well established that fine scale features can impact reservoir performance significantly. Because the high level of detail significantly exceeds the capabilities of standard models, procedures are required to coarsen the media's description to scales more suitable for flow computation. Such procedures are commonly referred to as upscaling techniques. There are a variety of different approaches for upscaling models for contaminant migration simulation. A key issue with any upscaling procedure is how well the coarsened (upscaled) model replicates important aspects of the fine scale flow behaviour such as total injection or average pressure or saturation throughout the reservoir, and breakthrough times of injected fluids. Additional issues are the degree of coarsening achievable by a given method, and the level of robustness of the coarse scale model i.e. its applicability to models with different global boundary conditions or sampling locations. In common with many other workers, in this project we upscale from below the continuum limit to above the continuum limit.

Another insight into upscaling across the continuum limit is given by Figure 1.25. This is a schematic diagram showing the different values of a property, such as permeability, when averaged over different scales. At the smallest length scale on the left, almost down to the molecular scale, the *Y-axis* variability of the property is great, and the averaging at a particular length scale is very difficult to predict. As the length over which the averaging takes place is increased, the average of the property in a non-fractal substance usually becomes more stable. Ultimately one reaches the scale corresponding to the representative

elementary volume of the substance, at which the average remains constant with respect to changes in scale. In terms of porous media, this would be an ensemble of pores and throats representative of the whole porous structure. Therefore the property can be upscaled from this minimum length scale to a higher scale, as shown in the figure. At a higher length scale still, new levels of heterogeneity become apparent and make the average more variable again. In terms of porous soil, this might be worm holes or fissures. For a natural non-fractal porous medium, the length over which upscaling can actually take place is often very small. So in practice, upscaling is usually extended to a longer length scale and the higher level heterogeneities, such as worm holes and fissures, are ignored. The averaging final levels out at the relative elementary volume for that property, or the smallest unit that can be upscaled to preserve the behaviour of the property. When uncertainty begins to fluctuate (representing imperfections in the medium) the use of the property becomes less valid and should be used with caution.
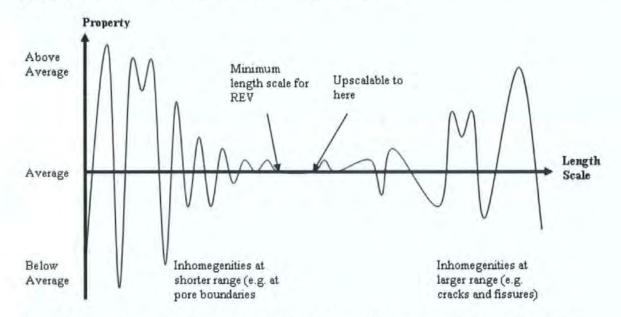
Figure 1.25   Variability of a property which can be upscaled over a specified range. See Section 7.4.2, P177 for a detailed discussion and suggested use of "The Scaleway" in upscaling properties.

1.12 Preferential Flow

Having considered upscaling, we now consider phenomena observable at a larger, scale just at the top of the continuum limit. The most important of these is preferential flow where large portions of a flow-conducting solid matrix, often including regions of immobile water, are bypassed by the mobile water fraction. The phenomenon is a matter of concern because it can facilitate the rapid transport of nutrients and chemicals away from the surface to groundwaters, resulting in less productive soils and pollution of drinking water.

Three main types of preferential flow have been identified (Miyazaki, 1993). The first is *bypass* flow, which may develop in a heterogeneous substrate, such as cracked or stony soil, if highly permeable macropores extend to the soil surface or the water pressure within them is positive, (Beven and Germann, 1982). (Flury *et al.,* 1994) pointed out that structured soils represented a greater risk to groundwater than homogeneous soils in transporting soluble pollutants, because of the bypassing of the majority of the soil matrix, and they concluded that preferential flow should be considered the rule rather than the exception.

The second type of preferential flow is *fingering* flow, which is the progress of unstable wetting fronts through a porous substrate. Fingering has been shown to develop in sandy soils in less hydrophobic areas, and is possibly correlated to particle size (Dekker and Ritsema, 1994) and (Ritsema and Dekker, 1994). Raats, (1973) showed how fingering may develop if the velocity of a wetting front increases with depth, and demonstrated with the use of a Green and Ampt model, several scenarios in which this might take place. Subsequently Hendrickx, Dekker, and Boersma (1993) used these criteria to demonstrate how fingering developing from a water repellent surface layer may result in six to thirteen times as much solute being transported to groundwater compared with transport from a wettable surface. Baker and Hillel, (1990) showed that fingering might arise at the interface between two layers of homogeneous sand when the bottom layer is coarser than the top layer. Kung, (1990), identified a third form of preferential flow, *funnel* flow, which takes place along inclined textural discontinuities.

It has also been demonstrated that preferential flow may occur even when there is no discernible structural cause for such behaviour. In a dye tracing experiment on field plots (Ghodrati and Jury, 1990), encountered considerable preferential flow, but were unable to identify the source other than to suggest that areas conducting greater flow were more likely to have higher permeabilities than surrounding, dryer areas.

Some form of preferential flow may also develop in samples which are much more homogeneous than those used in this study - i.e. samples with particles or features of only a single primary size. Even in this type of sample, heterogeneities can be introduced to the void phase by the packing process. It has been suggested that water in such samples flows in rivulets or small streams (Porter, 1968a). These rivulets may randomly meet and coalesce to form larger rivulets, or alternatively large rivulets may divide. Experiments conducted on random packing of uniform spheres, Raschig rings, Intalox saddles and Pall

rings appear to support this theory (Porter, 1968a). Porter, Barnet, and Templeman (1968), demonstrate a possible method for predicting the number of rivulets at a given depth. This has also been interpreted to imply that increasing sample depth may be accompanied by a decrease in the total number of rivulets, and an increase in the volume of water being transmitted by individual rivulets (Dexter, 1995).

1.13 Non-Aqueous Phase Liquid Flow in Natural Systems

Six main constituents affect NAPL migration in the subsurface; (i) the volume of NAPL released, (ii) the area of infiltration, (iii) the time duration of release, (iv) the properties of the NAPL, (v) the properties of the media, and (vi) the subsurface flow conditions, (Mercer and Cohen, 1990).

The principles of multiphase flow in natural systems have long been known to petroleum engineers, and involve the flow of water and other immiscible liquids. Schwille (1967) demonstrated that non-aqueous phase liquids (NAPL) such as organic solvents and other petroleum-based products could be divided into two categories depending on their density relative to water. Immiscible liquids, both those less dense than water (LNAPL), including cable oil, and more dense than water (DNAPL) are heavier than water and infiltrate into the ground at a rate dependent on the type of soil and the NAPL characteristics.

Whether the NAPL reaches the water table or not depends upon the spilled volume and the retention capacity of the soil. If the retention capacity is exceeded in the unsaturated zone, the fate of the NAPL becomes largely dependent on its density. A light immiscible liquid will tend to form a thin pool (lens) on the surface of the water table. Equation 1.27 shows a schematic representation of LNAPL infiltration. Upon reaching a layer which it cannot penetrate, lateral spreading will occur, following not necessarily the direction of groundwater flow but the local topography of the layer, (Thomson et al., 1992). As the water table fluctuates in response to local pumping or seasonal recharge and discharge, the lens of LNAPL can become smeared over a larger region, (Templeton, 1954).
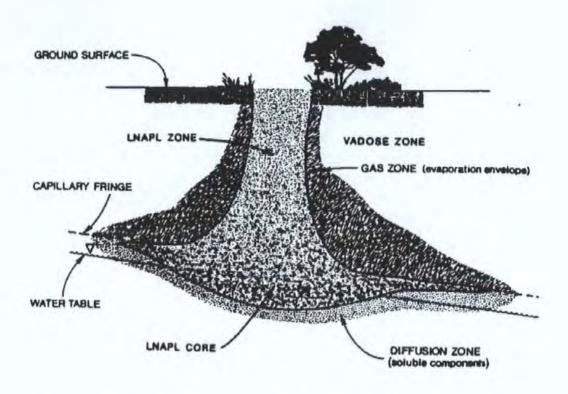
Figure 1.26   Schematic LNAPL infiltration (modified from (Pinder and Abriola, 1986)).

When introduced into the subsurface, gravity causes the NAPL to migrate downwards through the vadose zone as a distinct liquid. This vertical migration is also accompanied to some extent by lateral spreading due to the effect of capillary forces, and to the spatial variability of the medium, (layering). As the NAPL progresses downwards through the vadose zone, it leaves residuals trapped in the pore spaces. This entrapment is due to surface tension effects. In addition to migration of NAPL, some of the immiscible fluid may volatise and form vapour extending beyond the NAPL, (Mercer and Cohen 1990).

One of the reasons that only a limited number of comprehensive models have been developed is the complex physical and chemical nature of hydrocarbon contamination. The spreading of contaminants depends on many factors, such as volume of leakage, type of hydrocarbon product, hydrogeological conditions, hydraulic properties, and geological heterogeneity. A complex interaction between gravity and viscous and capillary forces determine the movement of the individual phases. The flow processes are further complicated by chemical and biological reactions within the two phases, (Host-Madsen and Hogh Jensen, 1992).

1.13.1 Multiphase Flow in soils

(Leverett, 1941) was one of the first researchers to explain the importance of capillarity in the field of petroleum reservoir mechanics. (Brooks and Corey, 1964) and (van

Genuchten, 1995) built on this work to develop models for the relationship between water saturation and the capillary pressure at the air-water interface.

Some numerical model studies of NAPL flow within soils do exist. Three dimensional, three-phase flow models have been developed by (Faust *et al.* 1989) and by (Letniowski, 1989). Both of these models assume a passive air phase, implying that the air phase is infinitely mobile. (Faust, Guswa, and Mercer 1989) applied their model to DNAPL from chemical landfills near New York.

One of the first series of experiments was carried out at the Swiss Federal Institute of Technology in Zurich in the late 1970's and early 1980's. In these two dimensional, three phase flow experiments, fluid pressures and saturations were measured simultaneously using embedded ceramic probes connected to pressure transducers and gamma-ray attention, respectively, (Schiegg, 1990). More recently, (Parker *et al.* 1991) performed saturation-capillary pressure experiments for air-water, air-oil and oil-water two phase systems in a sandy porous medium to validate the use of scaled multiphase versions of the Brooks-Corey and van Genuchten retention functions.

(Osborne and Sykes, 1986) have been some of the few who attempted to model a field contamination scenario. However the model under-predicted the NAPL migration, a failure which was attributed to the uncertainties in the input data. Nevertheless, their efforts illustrate the utility of mathematical models in focusing future site investigations and evaluating the effectiveness of various remediation proposals.

Many studies have concluded that preferential water and solute movement in undisturbed field soils is caused primarily by extreme variability in the sizes, shapes, connectivity and distributions of soil pores, and by fingering, wetting front instability, or funnelled flow at soil layer or horizon boundaries (Baker and Hillel 1990) & (Kung 1980). Because of this, (Bouma and Wösten,1979) have suggested that accurate representations of preferential flow behaviour can only be obtained from intact soil cores and blocks that contain major soil horizons or their boundaries. (Beven and Germann, 1982) suggested that representative elementary volumes (REV) that encompass macropore variability may approach or exceed $1m^3$, whereas $1cm^3$ volumes may suffice to represent micropore variability.

Field observations by Poulsen and Keuper, (1992), found that the migration and distribution of hydrocarbon contaminants are dominated by capillary forces and governed by the bedded structure of the sands. Detailed excavation and sampling revealed an extremely heterogeneous distribution of residual contaminant at the millimetre scale. They also discovered that a slow release of contaminant penetrated further than a ponded release.

(Dawe *et al.*, 1992) in an experimental study found that heterogeneities and the rate dependence of capillary forces have a significant effect on oil recovery. These studies show that the presence of heterogeneities can radically alter the pattern of migration and even the type of flow that develops. These results suggest that heterogeneity effects should not be ignored.

(Butts & Jensen, 1996) obtained results using selection of differentially textured sands packed in a flume. They discovered that the initial distribution of oil in the fine sand appears to follow a diffusion type flow. There appears to be significant horizontal spreading as the oil front reaches the slightly wetter soil above the boundary and the vertical oil permeability decreases. The low oil permeability in the fine sand close to the interface, caused by the increased water saturation, will reduce the vertical oil flux. Secondly, a capillary barrier effect may occur, causing the oil to form fingers at the point of breakthrough. Once formed, these fingers migrate downwards, the meandering pathway apparently caused by small-scale heterogeneities within the coarse layer, Figure 1.27.

Fine sand layer

Coarse sand layer
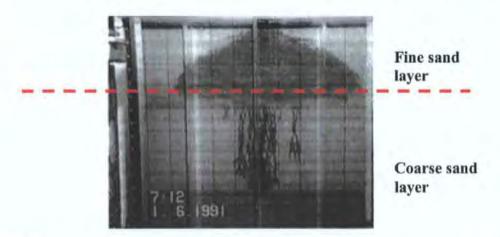
Figure 1.27   **Oil distribution in a layered sand, showing fingering in the coarse layer, modified from (Butts and Jensen 1996).**

(Jalbert, 2003) found that PCE (tetrachloroethene) distribution would also flow in discrete fingers or lobes. Results were obtained using gamma radiation analysis, as shown in Figure 1.28.
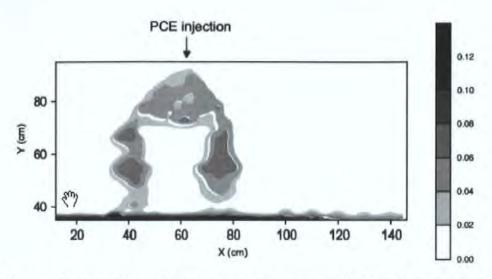
Figure 1.28   Tetrochlorethene (PCE) simulated spill, (Jalbert et al, 2003). Numbers indicate PCE concentration as recorded by gamma attenution.

1.13.2 Two Dimensional Laboratory Studies of NAPL

In 2-D experimental models, flow is constrained in only one direction. Typically, an experimental cell is used, with one dimension much smaller than the other two. For a 2-D study an experimental cell is used orientated vertically, it is assumed that fluid flow is parallel to the walls of the apparatus and fluid saturations are uniform throughout the cross section horizontally.

Numerous 2-D studies have been conducted in recent years. One of the first researchers to investigate NAPL migration in the subsurface was (Schwille, 1988). Numerous laboratory tank studies were performed for homogeneous, heterogeneous, and fractured media using chlorinated hydrocarbons. One study concentrated on the flow in layered sand, where lateral groundwater flow had little effect on the pollutant plume. Another experiment observed that a DNAPL migrated downwards in a broad group of small flow paths and that the presence of a water table had little effect, when studied using a fractured media. This work was later extended by (Kueper *et al.,* 1989) who studied the effect on migration using various bands of sand.

(Illangasekare, Armbruster, and Yates, 1995) noted that initial water saturation had a major impact on the flow of NAPL. In the unsaturated region, the fine sand layer trapped the NAPL, whereas in the saturated region the fine sand acted as a barrier to NAPL flow. In both cases, significant lateral flow of the DNAPL was observed.

(Parker et al., 1991) established a LNAPL lens and introduced pulses of water at the sand surface under gravitational forces. The water table was then raised to induce LNAPL

trapping in the saturated region. It was found that the proposed model overestimated the degree of oil drainage, vertical penetration, and lateral spreading that was observed.

Host-Madsen and Hogh Jensen, (1992) undertook a similar study, in which derived pressure-saturation and relative permeability relationships were predicted using parametric models. These were then compared to experimental data. Sand was packed into a Plexiglas tank and filled with water to establish a horizontal water table. LNAPL was added near the surface via a pump, simulating a point source at depth. They discovered that the flow of oil is characterised by a rapid spreading down through the unsaturated zone and a slower horizontal spreading within the capillary fringe. They also noted that the oil displaced the water phase at high concentrations.

A study by Pantazidou and Sitar, (1993) looked at the migration of kerosene in a variable saturated sand tank. The tank was fitted with porous disk pressure ports to provide aqueous and non-aqueous phase pressure data. It was found that LNAPL migration ceased after encountering the capillary fringe; the majority of LNAPL was located in a pancake-shaped lens pooled on the tension-saturation region. Water table fluctuations were found to spread the NAPL over a larger area with some LNAPL being trapped below the water surface.

Van Geel and Sykes (1994) investigated liquid pressure and saturation distribution during LNAPL migration through homogeneous, variably saturated sand. They found an increase in water pressure prior to the arrival of the advancing LNAPL front, which did not correspond with an increase in water saturation.

Another study investigated the oil infiltration from 15mm diameter point sources, into boxes (25cm x 25cm x 24cm) filled with sand or glass beads, (Simmons et al., 1992). It was found that transmission oil and mineral oil infiltrated differently; the transmission oil infiltrated uniformly into the glass beads, whereas mineral oil displayed channelling behaviour. Similar results were found for the sand although the channelling was more horizontally pronounced with a dendritic pattern. Additionally, they noted that the oils displaced substantial amounts of water from the plume.

Other studies have also been conducted on sand filled tanks. Many of these studies have concentrated on solvent flushing (van Geel and Sykes, 1994), although some researchers have investigated lens geometry (Schroth et al., 1995), and further studies have looked at

remediation strategies (Illangasekare, Armbruster, and Yates 1995), (van Geel and Sykes 1997). A general review of other two-dimensional NAPL experiments can be found in Chevalier and Peterson, (1999).

2 Project rationale, and under-pinning experimental and theoretical developments.

2.1 Introduction

This chapter explains aspects of the project rationale and developments to under-pin the rationale with regard to choice of soil type, experimental method and the reasons for further development of the Pore-Cor computer model.

2.1.1 Choice of Soils

There are innumerable soil types, so choice had to be based on a robust rationale. Experimental logistics had also to be considered, as the soil samples were expensive and difficult to extract, and time consuming to analyse. It was therefore decided to draw a transect across the soil diagram and select four soil types of varying texture (varying % sand, silt and clay content), which would also be of interest to National Grid Transco (NGT) formerly the National Grid Company plc. This region is highlighted by blue dashes in Figure 2.1. Regions outside the range of the pedo-transfer function used are not gradually encountered in England and Wales and are shown in grey. Figure 2.1 shows the distribution of the soil types chosen. All soils were extracted from sites in England and Wales. The sandiest soil was the Crediton series soil located at De Bathe cross, North Devon. This soil has already been used in several experiments and was therefore used to calibrate the experimental protocol. The subsequent experiments then used the parameters established by this calibration experiment. Other soils were the Conway Series (Silty Clay, Wales), Clifton (Sandy clay loam, Cheshire UK) and Sollom (Clay loam, Cheshire, UK), all shown red in Figure 2.1.
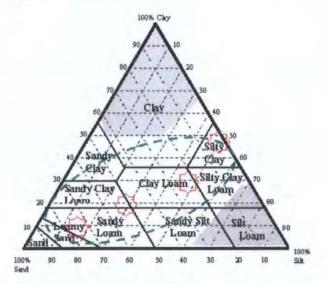
Figure 2.1   Distribution of the soil samples, from left to right: Crediton, Sollom, Clifton & Conway.

2.1.2 Desk Investigation and Sample Location.

Any remediation or hazard assessment scheme relies on accurate predictions of NAPL dispersion patterns in the relevant soil texture. Of these, a previous survey for the NGT carried out by the NSRI (National Soil Research Institute formerly the Soil Survey of England and Wales) detailed soils that were found to lie in suitable locations for extraction. The Crediton series soil used to calibrate our experimental apparatus was easily accessible. For the other soil types, access had to be granted by local landowners. Once soil locations and landowners were identified they could be approached and samples extracted.

2.1.3 NSRI Data, Soil Map and Soil Locations.

The NGT provided transect details of several of their underground pipeline routes. The routes identified several soil types that the underground cable would be lain through. A list of soils was then compiled, and their details and properties ordered from the NSRI. To calibrate the experimental protocols a known soil of the Crediton series was used. The Crediton soil is a sandy loam, which has been classified as a stony member of the Crediton series, located at De Bathe Cross, near IGER North Wyke, Devon, UK. This soil has been used in other investigations and consequently its soil characteristics are already well established, (Peat *et al.*, 2000), and (Holden *et al.*, 1995). Table 2.1 shows some of the soil characteristics for the Crediton soil.

Analysis	Crediton
Horizon	B
Depth (cm)	30-100
"600μm – 2mm" (w/w%)	16.97
"212μm – 600μm" (w/w%)	31.86
"106μm - 212μm" (w/w%)	4.27
"63μm - 106μm" (w/w%)	26.52
"20μm – 63μm" (w/w%)	5.19
"2μm – 20μm" (w/w%)	7.44
"< 2μm" (w/w%)	7.75
Organic Carbon Content (%)	0.3
pH	5.7

Table 2.1   Characteristics of Crediton Soil.

The geographical location of the soil data was supplied in the format shown in Table 2.2. The appropriate Ordnance Survey tile was identified from the Northing and Easting and the corresponding OS map location identified. Plotted on this map were the boundaries of soil types encountered in the area. Difficulties in selecting suitable soil samples included the charting of the soil at a resolution at which a series could be identified. At the time of writing very few maps of a sufficient resolution were in existence.

SERIES NAME	EAST 10M	NORTH 10M
CONWAY	269610	229290
CONWAY	326130	313370
CONWAY	326130	313370
SOLLOM	346630	404560
SOLLOM	346630	404560
CLIFTON	400160	306210

Table 2.2   **Soil Locations**

This restricted the areas available for sample identification and extraction. Table 2.3 lists the characteristics of the soils involved in this study.

Series Name	Parent Material	Major soil Goup	Surface Texture	Subsoil Character	Topography	Natural Drainage
Clifton Series		Surface water Gley	Sandy loam to loam	Grey-Brown clay to clay loam,rust mottled, passing to grey sandy clay loam-blocky and prismatic in structure	Slightly undulating slopes less than 2 degrees	Poor
Conway Series	Alluvium shales	Gley non calcerous			Slightly undulating slopes less than 2 degrees	Poor
Sollom Complex		Podzol	Peaty or humose loamy sand to sandy loam	Brownish grey structureless sand	Slightly undulating slopes less than 2 degrees	Poor

Table 2.3   **Soil characteristics, source NSRI map legend**

Figure 2.2 & Figure 2.3 are views of sample site and location with soil marked on the corresponding Ordinance Survey map in green. In this example it can be seen that the Conway series soil lies along the low area of a river valley. The flat area between the ridges shown in the diagram was the sample location. Photographer orientation is indicated with a red arrow on the OS map below. During initial fieldwork reconnaissance, auger samples of the soils were taken and brought back to the lab for analysis and identification.

Figure 2.2   Conway Valley in Wales.
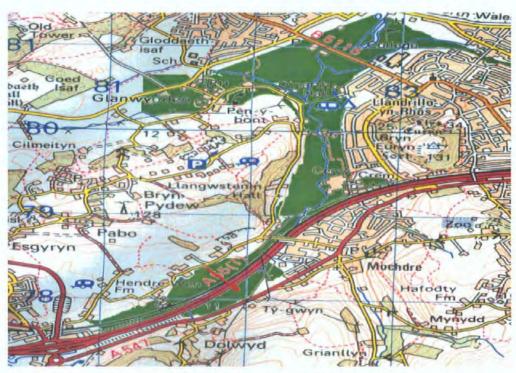
Figure 2.3   OS Map of Conway Valley North Wales. Soil distribution marked in green. Location and orientation of Photographer is marked by the red arrow on the map. Reproduced under licence.

2.2   Development of an Environmental Impact Prediction Software Package.

The water retention properties of soil, as measured on sand beds and porous plates in a laboratory, are important characteristics. However, the curves are difficult to obtain, exhibit a range of shapes, and do not always approach the expected asymptotes of differential pressure or tension. Therefore much work has been carried out to parameterize the curves, using equations proposed by for example (van Genuchten, 1980), (Chu, 1994), and (Kosugi, 1994). Such parameterization can achieve four useful objectives:

(i) it can reveal trends in the parameters across a range of soil samples,

(ii) these trends can themselves be fitted by some form of multiple regression and formed into a pedo-transfer function,

53

(iii) the pedo-transfer function can then be used, with caution, to fill in missing points in water retention curves or to correct outliers, and then

(iv) other properties can be calculated from the parameters, notably saturated and unsaturated hydraulic conductivity.

Such an approach has proved to be immensely useful. However, there are four underlying problems. The first is that the parameterization is based on an arbitrary choice of mathematical equation, typically one that produces a sigmoid water retention curve. Such curves overlook subtle effects such as concentric or layered zones of different void sizes, which tend to produce an angled stepped rather than sigmoidal shape. Other soils, such as some volcanic soils, can generate a two-step water retention curve, which can also be missed by an inflexible fitting function. The second problem is that the parameters obtained relate to the mathematical equation, but do not often have a direct relationship to any observable property of the soil structure. The third is that in some of the chosen equations, the fitting parameters are not entirely orthogonal, so that more than one set of parameters could fit the same curve. Finally, no three-dimensional network of voids is generated, and correspondingly no account is taken of the shielding or shadowing of large voids by the smaller connections through which they are accessed. The calculation of other properties therefore relies on the implicit assumption that all voids within the soil are fully accessible. The only void geometries that satisfy this accessibility requirement are a bundle of straight, unconnected tubes connecting the water source and sink (the straight capillaric approximation), or a bundle of such tubes that are tortuous (the tortuous capillaric approximation), or a single tube of a radius which gives properties that are approximate averages of those of the experimental sample (the effective hydraulic radius approximation).

Previous work carried out by Peat *et al.* (2000), demonstrated how water retention curves could be parameterized in a different way, using parameters that define the geometry of a three-dimensional network. The network comprised an infinite array of connected unit cells with periodic boundary conditions, each unit cell contained up to 1000 cubic pores connected by up to 3000 cylindrical throats. The geometry of the unit cell was adjusted so that the void network had the same porosity and water retention characteristics as the experimental sample. The fitted geometric parameters, such as connectivity, could then be used for objectives (i) and (iv) above – i.e. to reveal subtle trends for different soils, and to predict other properties. Objectives (ii) and (iii) were deliberately eschewed; pedo-transfer functions could be avoided and fit directly to raw data where such data is available, and the

absence or wide scatter of water retention measurements are directly reflected in the error limits of the derived parameters.

However, the parameterization in this approach is still arbitrary. The void network is a gross over-simplification of an actual soil structure, and very few characteristics of it are adjustable. Nevertheless this approach represents an important step closer to reality, for four reasons:

(i) the shielding effects mentioned above are taken into account,

(ii) a picture of the void structure can be generated, and 'toured' in virtual-reality,

(iii) the geometric parameters are actually or potentially verifiable by experiment, and

(iv) the resulting structure can be manipulated, either by introducing different fluids, or by geometric transformations which represent perturbations such as compaction.

Peat *et al.*, (2000) illustrated that for a specific soil sample the Pore-Cor network model produces saturated and unsaturated hydraulic conductivities with a much more realistic absolute value and trend than models that ignore shielding effects. A final stage should then be a comparison of the simulated results with reality, but as yet suitable data does not exist. Instead, the best available results are based on an approach by Mualem, (1976) which implicitly ignores shielding effects, and which is therefore less realistic than our own model. The Mualem approach is known to be inaccurate for the calculation of saturated hydraulic conductivities, and is therefore usually used only for the calculation of unsaturated hydraulic conductivities. Nevertheless a comparison was made between the saturated hydraulic conductivities, as detailed in Chapter 6.

2.2.1 Development of a software package usable for the NGT

The NGT required an easy to use field-deployable environmental impact assessment software package. Figure 2.4 represents a flow chart of predicted use and data generation for the software package. The numbers refer to the description paragraph of each process.
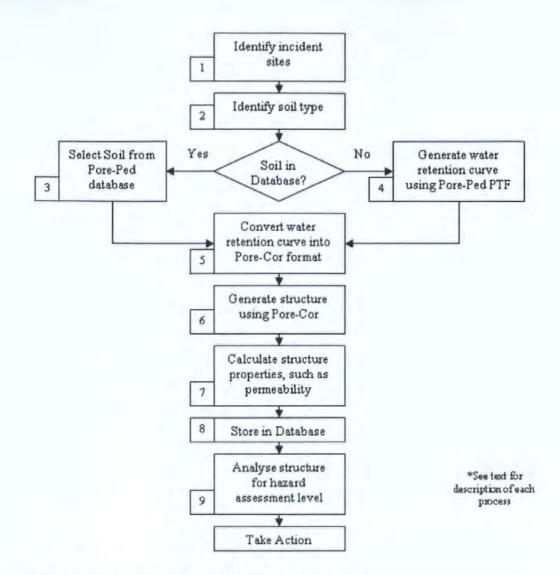
Figure 2.4   **Flow Chart for expected use of the interface.**

[1] All sites of cable junction boxes were listed for this project by NGT. Such a listing allowed all the sites to be ranked for hazard assessment purposes, or, if an actual leak were to occur at one of the sites, for pre-modelled data to be readily accessed.

[2] The soil at each site was then identified by the procedure already described in section 2.1.3. For this study, the soil types corresponding to four sites were studied in detail, as described in section 2.1.1. In a parallel study by Bodurtha, some 1200 sites and their soils were identified for hazard assessment purposes.

After identification of an incident by NGT, the location would lead to the soil type. Following soil identification the user can query the Pore-Ped database for existing experimental data.

[3]   If the soil is present in the database then raw experimental data can be converted directly into a Pore-Cor file. Figure 2.5 is a screen shot of the soil database, showing a soil

56

from the UNSODA data set compiled in the US (Nemes, Schaap, *et al.*, 2001). This soil can then be loaded into the Pore-Ped main screen as shown in Figure 2.6.
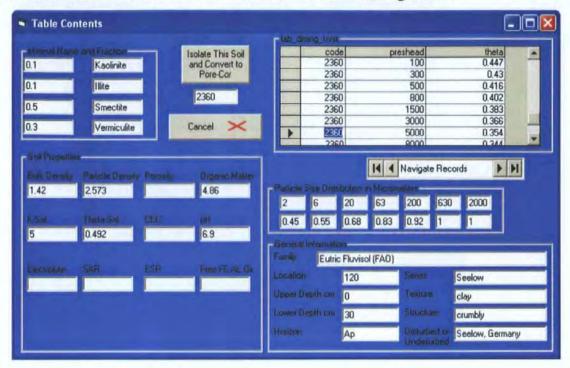
Figure 2.5   **The Pore-Ped database access screen.**

[4]   If a soil was not present in the database, a graphical interface can be used to generate a water retention curve for a required soil texture based on a standard ternary phase diagram Figure 2.6. Each axis represents the % of sand, silt and clay content of the soil, with organic carbon and bulk density properties entered using the drop-down boxes on the right hand side of the console. When a mouse pointer is clicked within the triangular diagram boundary, the appropriate texture is automatically generated, along with a PTF water retention distribution for the required density and organic carbon content. If no experimental data exists then the soil series can be simulated using the NSRI pedo-transfer functions developed by (Mayr, 1999) as shown in Equation 1.27 & Equation 1.28. From this a Pore-Cor intrusion curve can be generated.
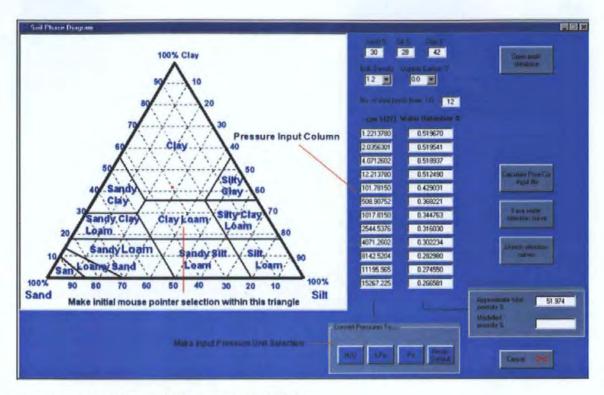
Figure 2.6   The Pore-Ped soil modelling Interface

[5]   The water retention curve is then used to calculate the air intrusion curve:

$$A_i = W_{max} - W_i$$

Equation 2.1

where A_i is air intruded at the ith point, W_{max} is the max water retention and W_i is the water retention at the ith point, Figure 2.7 and Figure 2.8.
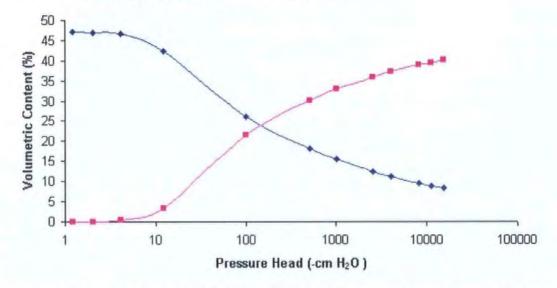
Figure 2.7   Air intrusion (pink) with diminishing water content (blue) at increasing suction.

Figure 2.8 Converting the water retention curve to a Pore-Cor usable format.

[6] Using the data file produced by Pore-Ped, Pore-Cor is then used to generate a corresponding structure. Figure 2.9 shows the Pore-Cor user interface.
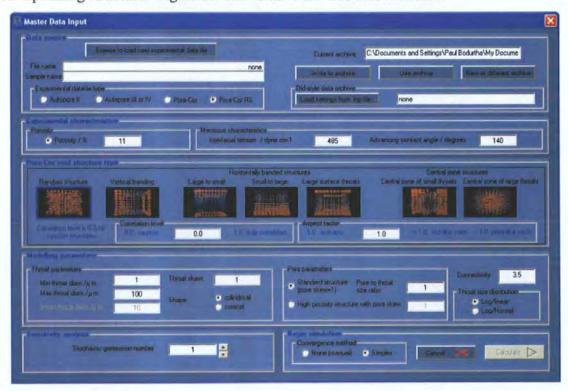
Figure 2.9 The Pore-Cor master console.

Chapter 6 contains detailed analysis of calculations and interpretation of the Pore-Cor structures.

[7]   The hydraulic conductivities and other properties of the structures are then calculated for later assessment. The Pore-Cor model produces parameters which relate directly to the geometry of the simulated fitting network.

[8]   The parameters can then be stored in a database for use and reporting. The database developed in this project is very sophisticated in terms of its ability to store and regenerate models, and to output summaries of data in various forms. The analysis of each soil required many stochastic generations. So the database was an essential component of the success of this project. It was also vital for the study of the 1200 soils in the consecutive study by Bodurtha, 2003.
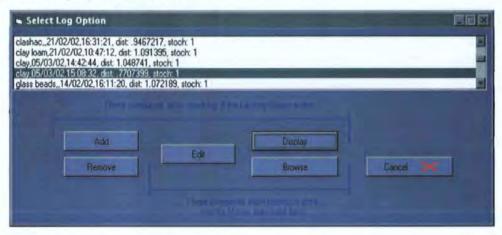
Figure 2.10   The database control panel

The user can utilise the database by selecting a sample which has been previously run and stored in the database, which can then be immediately loaded for examination, and further processing for the study of further characteristics. Such further characteristics include occlusion by a non-wetting fluid, compaction, colloid and permeability of different gases and hydraulic conductivity of liquids. Figure 2.10 and Figure 2.11 are screenshots of the database control panel and interface screen. The controls on the latter change according to the operational mode chosen on the control panel.
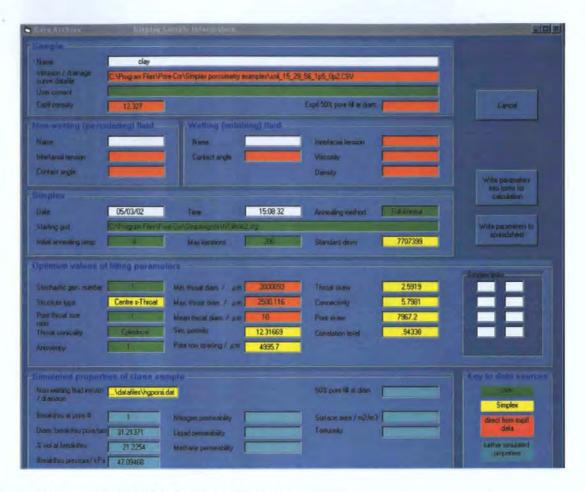
Figure 2.11   The Pore-Cor database data screen.

[9]   After analysis, appropriate remedial action or prioritisation could then be made.

2.3   Analysis of Laboratory Soil Samples

2.3.1 Introduction

The ability to measure, model and predict the movement of pollutants in soil is important for environmental and health reasons. However, many studies use samples of soil which are extracted from a site and then re-packed into experimental cells (typically cubes or cylinders). Such re-packing alters both the density and structure of the soil. It is not usually possible to re-pack a soil sample to its natural density as the laboratory containers do not have the same lateral compressive force as the ground the soil is extracted from. Although there are few studies of the effect of reducing the density of a soil sample, as in the present study, the reverse effect, compaction, is well known.

Compaction affects water, heat, and gas exchange and consequently hydraulic properties of the soil. (Schafer *et al.*, 1992) stated that "significant knowledge gaps exist in the description and modelling of soil compaction behaviour, in relating soil compaction to biological and physical responses and to conservation of soil and water resources".

Soil pollutants are in the form of both aqueous phase liquids, and non-aqueous phase species (NAPL). Aqueous phase pollutants include nutrients such as phosphate and nitrate species, which when mismanaged cause eutrophication. Since these and other aqueous phase pollutants tend to have a reservoir and exchange capacity with soil, which can confuse the effects of re-packing, a conservative tracer was used in this study, namely bromide which has a well established methodology associated with it (Butters, Jury, and Ernst, 1989); (Bowman *et al.*, 1994)).

2.3.2 Extraction of 0.5m Soil Blocks

Four 0.5m blocks of soil were isolated and extracted for study in the automated lysimeter. After removal of topsoil, each block was extracted undisturbed by excavating a trench approximately 2m wide around a column, slightly larger than 0.5m x 0.5m, using a mechanical digger. The sample container was slid over the column in the middle of the pit and excess soil removed as the container was moved down the column. The polycarbonate container had its joints previously sealed with an epoxy gel. Figure 2.12 is a schematic representation of the extraction pit excavated during soil extraction.
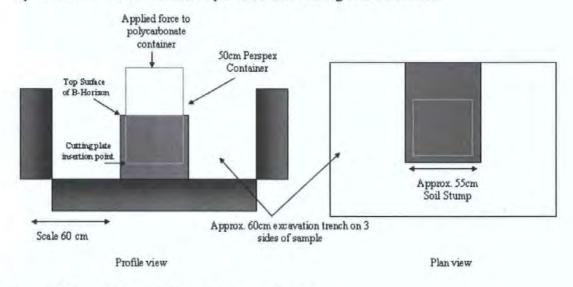
Figure 2.12   **Schematic View of the excavation Pit**

A metal base plate was then inserted beneath the container at the depth that the soil was to be extracted. The soil block was then extracted and transported to the laboratory and mounted on the automated lysimeter. The join between the polycarbonate box and aluminium collection plate was sealed with more epoxy resin. Figure 2.13 a, b, c & d illustrate stages of soil extraction. An area of approximately $3m^2$ was prepared in this way. The soil column was then isolated in the centre of this area, to a size slightly larger than the dimensions of the container.

Phase I
Isolation Of The Soil Block

a) A-Horizon stripped, 1ˢᵗ trench excavated. b) Cutting plate inserted, block isolated.

Phase II
Removal Of The Soil Block

c) Block cut and isolated from ground. d) Block removed from ground.

Figure 2.13   a, b, c, & d. Stages of soil block extraction.

Figure 2.14 shows the Crediton soil sample after the extraction of the soil block. The block was wrapped in thick plastic sheeting to prevent any excess shrinkage or swelling due to water loss or water gain. The soil blocks were monitored for any biological activity with any visible biological agents being removed. The soil blocks were stored for a maximum period of around six months. When unwrapped and mounted they were still moist at the top, with no visible signs of shrinkage or swelling such as large cracks or fissures in the soil samples faces.

Figure 2.14   The extracted soil block awaiting mounting onto the lysimeter.

2.4   Development of Experimental Protocol Using Soil Core Experiments

Samples of Crediton series soil (Crediton series, DeBathe Cross, North Wyke, Devon, UK) were compared in the laboratory. Cores of 50mm diameter were extracted intact using a tractor mounted steel cylinder corer. Experiments in the 0.5m lysimeter could only be carried out once, due to the difficulties of soil extraction, and contamination history of the soil within the lysimeter. An experimental protocol for the elution experiments was therefore developed using 50mm diameter cores.

The primary consideration was to ensure tracer movement through the soil column sample body and not at the soil sample container interface. To achieve this, a barrier was placed between the soil column and its housing. A multi-layered barrier was the most effective type, (personal communication with Haygarth & Whalley; 2000). The soil column housing was first cut lengthways in half. The exposed soil surface was then covered with a layer of heated petroleum jelly. The petroleum jelly penetrates the surface pores along the column length and provides a hydrophobic barrier. When the surface was completely sealed a thin layer of sheet 'cling film' was overlain on the surface of the now solid petroleum jelly, forming an impermeable seal. The casing was then replaced, as it was needed as a structural support for the column. This process was then repeated for the other side of the column ensuring all water flow takes place through the sample body. Cable ties were used to hold the core assembly together, and to fix a nylon mesh (mesh size 0.25 mm) across the base of the sample. The mesh prevented the sample falling out from the bottom of the column but allowed the free flow of fluid. A 1cm layer of fine sand (>98% SiO_2, Redhill Sand) was added to the top of the soil column, to ensure tracer was distributed evenly across the top of the column.

2.4.1   Sample Saturation

The sample was saturated, with a mixture of top-down and bottom-up saturation regimes. The bottom 30 cm of the sample was soaked for 20 hours in a bucket of distilled water. The sample was then removed and placed into a vertical stand clamp. The sample was allowed to gravity drain, which caused the bottom of the sample to have a lower saturation than the central or upper zones of the sample. A peristaltic pump was used to pump Milli-Q water on to the sample surface. The flow rate was decided upon when the sample reached a flux equilibrium, i.e. one drop in /one drop out. The combination that achieved this was an Isomatic *Fixo* 8 roller peristaltic pump. The pump had an r.p.m of 40, with Elkay peristaltic tubing (I.D. 0.020) producing a flow rate of 16.2 ml hour $^{-1}$. Once

saturation had been assumed to be complete (a steady flow from the bottom of the soil column), equilibration was achieved at an introduction rate of 16.2 ml hour^{-1}. The experiment could then proceed.

2.4.2 Experimental Procedure

A bromide tracer was produced by dissolving 1 g of KBr (AnalaR grade, BDH) in 1 litre of Milli-Q. When the sample preparation had been completed, the core was mounted in a stand clamp with the experimental set-up shown in the Figure 2.15. The tracer was introduced at the top of the sample using a syringe. The tracer was 1ml in volume. During the experimental period of 2000 minutes, rainfall was applied continuously. Samples were collected every 20 minutes by a rotary auto sampler. The samples were then analysed using a Skalar air segmented flow analyser described in Chapter 3.

Water introduction 16.2 ml/h

Eluate Collection

Reservoir

Sample
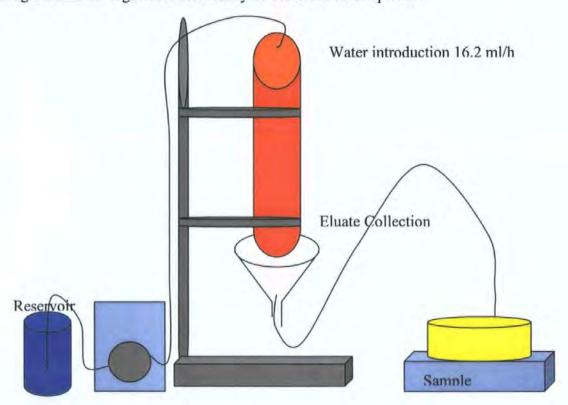
Figure 2.15   **Core experiment apparatus, (Blue reservoir, Grey peristaltic pump, Orange Soil Core, Yellow sample collector).**

2.4.3 Results

The column experiment showed that the bulk of the Br$^-$ appeared at the bottom of the column between 400 and 800 minutes at a maximum concentration of 34.31 mg l^{-1} Br$^-$. The bulk of the bromide had passed through the column within 12 hours of being introduced into the top of the column. Figure 2.16 is a typical plot of the concentration of bromide plotted against the time the sample was taken in minutes (x-axis).
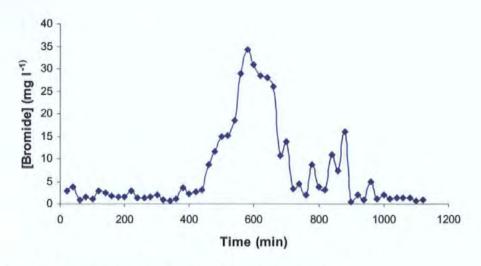
Figure 2.16   **Br⁻ breakthrough for Crediton column Experiment.**

The results show a clear breakthrough curve for the Crediton series core experiment.

2.4.4 Summary

Taking into account lateral dispersion effects and texture differences, it was decided to run the 0.5m block experiments over a 40 hour period. For a rain agent the MilliQ was unsuitable. It may strip sorbed phosphate particles from the surface of any clay present in the soil, as well as mobilising the already aqueous phosphates in the soil. It was therefore decided to use a less ionic negative solution in the 0.5m block experiments. It was decided that tap water would provide a good suitable supply of constant quality water. Consequentially nitrate could not be studied. Phosphate is an important topical contaminant and is not found in tap water at detectable limits (using the Skalar, detection limit <2 ppb), so could be studied.

3 Analytical Methods

3.1 Introduction

This chapter describes the design of suitable analytical methods for determining (1) oil distributions in laboratory mounted soil blocks and (2) bromide and phosphate tracer concentrations in leachate samples from soil blocks. The determinations took place in two distinct matrices:

1. The oil was analysed within the soil matrix.

2. The phosphate and bromide tracers were analysed in aqueous solution.

The experiment was conducted over three stages. The 1st stage was the wetting of the soil and introduction of Bromide and Phosphate tracers in a highly concentrated aqueous slug at the surface of the soil block, as illustrated in Figure 3.1.
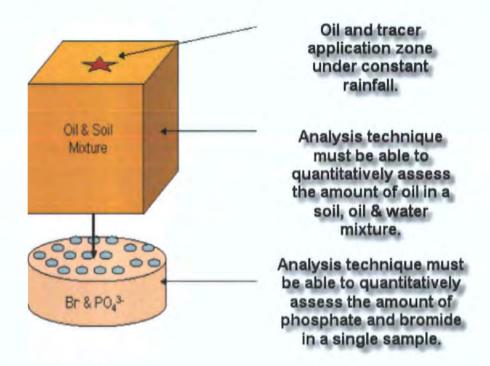
Figure 3.1   Sources of analytical samples

These samples were then collected Table 3.1: [1&2] and analysed. The 2nd stage of the experiment was the introduction of a cable oil sample into the soil block. This was left for 8 hours under rainfall when the 3rd and final stage was the introduction of a second set of tracers [3]. Figure 3.2 indicates the structure of the experimental period.
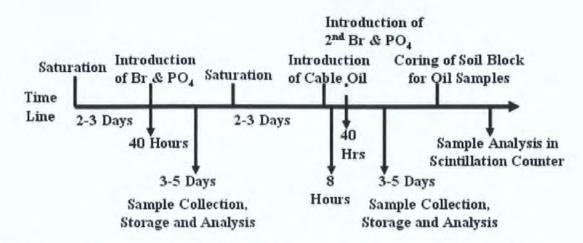
Figure 3.2   Experimental Timeline and points of introduction of tracers into the soil bock

Factors such as sample throughput[4], sample preparation, reliability, sample storage and cost must be considered when choosing an appropriate analytical method. The manifold must give consistent results, and calibration must be consistent.

Problem Number	Problem Name	Comments
1	Sample Storage	No Degradation
2	Sample Tracking	Sample Loss, Mixing
3	Reproducibility	Consistent Calibrations
4	Throughput	Rapid Analysis Desired
5	Economics	Inexpensive Reagents
6	Disposal	No Disposal Issues

Table 3.1   Addressing Problems to be overcome. Numbers relate to superscript numbers in the text.

The reagents must not be costly [5] as large volumes of sample are to be analysed and the reagents must not cause a hazard when being disposed of [6].

Laboratory instrumentation can provide reliable, multi-parameter detection but raises the question of sample storage, an area of great importance, as an incorrect storage protocol leads to poor data and invalid models. Several authors have reported studies on the examination of sample container preparation, cleaning protocols and sample capture methods (e.g. Gardolinski *et al.*, 2000, Maher and Woo, 1998). Sample preservation protocols should be chosen to minimise the processes that can alter the physico-chemical forms of target species during storage. In this study samples were generated in batches of several hundred. Apart from logistical considerations and tracking of samples the storage time had to be kept to a minimum. For this reason rapid, automated sample analysis was a desired feature of the experimental protocol.

Section 3.2 discusses the analysis of oil in soil cores. Section 3.3 discusses the analysis of aqueous samples for bromide collected from the base of the soil block using the automated lysimeter as described in Chapter 4. Section 3.3 also discusses the analysis of phosphate in aqueous samples collected from the base of the soil block.

3.2   Determination of oil in soil blocks

3.2.1   Overview of techniques

This section discusses the various extraction and analytical techniques necessary for reliably determining the quantity of cable oil in soil samples. The chosen techniques are then applied to the determination of cable oil in selected samples. The analytical methods used in this study had to satisfy several criteria. In conjunction with an appropriate extraction technique, they had to quantify oil accurately and unambiguously in highly water-saturated sand, with the capability of also determining oil in soils. Each soil block would have 250 samples to be studied, so the method had to be relatively rapid and simple. The method chosen for laboratory experiments was scintillation counting of a radio-labelled analogue. Previous studies utilising sand columns have used total organic carbon (TOC) analysers. However TOC analysis is unsuitable for the quantification of oil in soil because each soil sample is unique and has a variable organic content.

Microwave assisted Soxhlet extraction, as specified in the US Standard Methods for the Examination of Water and Wastewater and used by (Garcia, 2003) proved to be too slow for large numbers of samples. Despite optimization and the use of dual extraction chambers as shown in Figure 3.3 the typical time ranged from 2 hours up to 24 hours depending on the extent to which the soil had been exposed to the organic compounds within it.
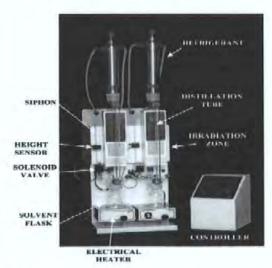
Figure 3.3   A Optimized MASE (microwave assisted Soxhlet Extractor), J.L. Luque-Garcia (2003).

Accelerated Solvent Extraction (ASE) works on the same principal as Soxhlet extraction. ASE accelerates the extraction of solid matrices by using solvents at elevated temperatures and pressures. Increased temperature accelerates the extraction kinetics, while elevated pressure keeps the solvent below its boiling point. The time taken for analysis and the level of solvent consumption are reduced compared to the Soxhlet method, representing a significant advantage over the latter technique. Studies have found the ASE technique to be erratic, partly because of variable instrument parameters and operator dependence. Many of the solvents for oil, including 1, 1, 2-trichlorotrifluoroethane and dichloromethane are difficult to use for safety and environmental reasons. This therefore limited the extraction methods available for the study.

Technique	Advantages	Disadvantages
Liquid Scintillation Counting	Specific to DDB, Quick, Small standard deviation in results	Uses ^{14}C.
Fluorometry	Quick, Small standard deviation in results	Uses a large volume of solvent
FTIR	Low Extraction	Large deviation in results
Gas Chromotography	Highly accurate, Qualitative analysis	No direct method on quantification
Soxhlet	General high extraction efficiency	Takes a long time
Accelerated Solvent Extraction	High extraction efficiency	Costly, High standard deviation
Shaking	Quick	Reasonable extraction efficiency (lower than ASE and Soxhlet)
Sonification	Fairly quick	Reasonable extraction efficiency (lower than ASE and Soxhlet)
Total Organic Carbon	Requires no solvent extraction	Does not work on soils

Table 3.2   Advantages and disadvantages of techniques used for the determination of oil in soil.

Therefore a more suitable technique utilising a radio labelled compound was employed. A radio labelled analogue of do-decyl benzene (DDB) was introduced into the soil blocks, and its dispersion measured using a scintillation counter. This required no extraction or solvents to be used and is therefore a more environmentally friendly technique. It was specific to the C_{14} introduced into the soil, with very little background interference from organic carbon content of the soil. The scintillation and oil synthesis procedure are detailed in section 3.2.3.

3.2.2 Principles of Scintillation Counting

A scintillator is a substance which emits a weak light flash or scintillation, of a short duration, when struck by an ionising particle. The intensity of the scintillation depends on the energy of the particle dissipated in the scintillator. A photomultiplier tube - a device that is sensitive to weak light signals and converts them into amplified electrical pulses - is used to detect the scintillations. Figure 3.4 shows a schematic diagram of a scintillation counter.

The scintillation shines on the photocathode of the tube and causes the emission of photoelectrons. These electrons are accelerated by the potential applied between the electrodes of the photomultiplier. The accelerated beam of electrons impinges on a sequence of electrodes, or dynodes, at each of which secondary electron multiplication occurs, producing successive amplification of the electron current. The overall multiplication factor or gain M of the photomultiplier depends on the number of dynode stages and on the applied potential. The electrical pulses from the anode of the photomultiplier are fed to electronic circuits for amplification, pulse-amplitude measurement, data analysis and recording.

Where radioactive samples are used, a scintillation cocktail is added to the radioactive sample to convert the energy of the radioactive decay particle into visible light. This can then be detected by the scintillation counter. The light is emitted from the liquid scintillation vial in all directions and is 'directed' onto two photo-multiplier tubes that convert the light into a measurable electrical pulse.

beta-particle (energy W)

reflector
scintillator
scintillation photons
photocathode

photo-electrons
photomultiplier

secondary electrons

dynode 2

dynode 1

dynode 14
anode

anode pulse

electronic circuits
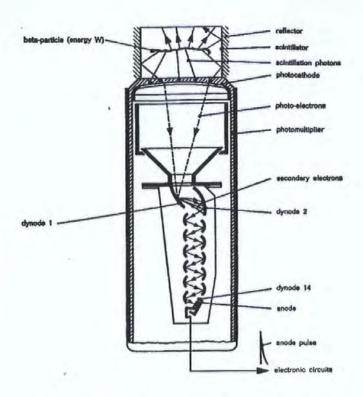
Figure 3.4 **Schematic diagram of a scintillation counter showing the stages of conversion of beta-particle energy into scintillation photons, photo-electrons, secondary electrons and anode pulse, (adapted from Birks, 1974).**

The pulses from the photo-multiplier tube are analysed, converted into digital form and stored. The data accumulated in the multi-channel analyser over the counting time of the sample is then used to determine the Counts Per Minute (CPM), of radioactive decay in the sample. CPM is the total number of pulses in the channels of the multi-channel analyser divided by the total time in minutes for obtaining the counts. The number per minute or counting rate of the pulses is the same as that of the original scintillations detected, and this is determined by the number of Disintegrations Per Minute (DPM), or activity of the source of ionising radiation. This can then be converted into concentration using a calibration curve.

3.2.3 Instrumentation and Procedures

The scintillation counter used in this study was the Beckman LS 6500 Scintillation System. This instrument is designed to provide highly accurate, automated counting of the level of radioactivity in a sample. It can hold up to 300 vials at any one time. The vials used throughout this study were 40mL in volume and made of clear polyethylene with a polyethylene cap. The scintillation cocktail used for this study is Sigma-Fluor LSC Cocktail for non-aqueous samples, (Sigma-Aldrich Company, Dorset, UK).

In order to apply scintillation counting to the analysis of 'cable oil' concentration it was necessary to produce a radio-labelled version of cable oil. This ensured that the analysis would be compound specific. The oil was synthesised by a Friedel Crafts reaction.

Figure 3.5   Alkylation process.

This method of synthesis (Figure 3.5) utilises an alkyl halide as the alkylating agent together with a metal halide catalyst, aluminium chloride. The metal-halide catalyst functions much as it does in halogenation reactions; that is, it provides a source of a positively charged substituting agent, which in this case is the carbonium ion. There are several factors that need to be considered when using this reaction. A large excess of benzene is needed to limit the reaction to monosubstitution because the introduction of one alkyl substituent activates the ring towards secondary substitution. The second limitation of the reaction is the penchant for the alkylating reagent to give rearrangement products. This is actually an advantage in this study as cable oil has a range of products. The last complication of the alkylation process is that the products often isomerise. A GC-MS analysis of the synthesised product produced a chemical fingerprint which could then be compared to the original Cable Oil GC-MS to ensure a comparable structure.

A two litre three-necked flask with a separatory funnel, a mechanical stirrer and a reflux condenser were fixed together. Attached to the top of the condenser, a tube led to an inverted funnel that dipped below the surface of 320 mL of benzene (including 100 μCi of ^{14}C-labelled benzene), and 8g of anhydrous aluminium chloride were placed in the flask and stirred. A mixture of 136 mL of benzene and 114 mL of bromo-undecane was then incorporated drop-wise into the flask. The flask was warmed to 80 °C on a water bath. When this mixture had increased in weight, it was poured onto ice. Washing the mixture successively with dilute sodium hydroxide solution and water, and then drying with anhydrous magnesium sulphate, removed the upper hydrocarbon layer. The remaining compound was distilled through a well-lagged fractionating column. The excess benzene passed over first, followed by the dodecylbenzene.

The radio-labelled version of cable oil was analysed by GC-MS to verify that the substance produced conformed to the chemical characterisation of cable oil, Figure 3.6. A study of the resulting compound (Rowland, 1996) determined that the synthesised cable oil is a

close enough match to the original cable oil to be used in the analysis. The main difference between the compound shown in Figure 3.6 and the analysis of actual cable oil, is that the radio-labelled version does not have the same spread of chain lengths. The synthesised version only had C_{11} chain lengths, whilst the original contained a mixture of chain lengths between C_{10} and C_{14}. However, the synthesised compound contained a mixture of both branched and linear alkyl chains, like the original.
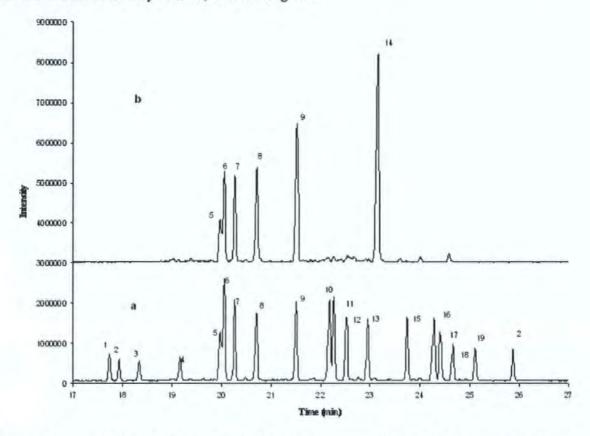
Figure 3.6 **GC-MS of Cable Oil a) and b) Radio-Labelled DDB.(Rowland, 1996). The numbers refer to the order that the peak was produced by the GC-MS. Top is analogue bottom is real Cable oil sample.**

3.2.4 Calibration Graph

The use of the liquid scintillation counter does not specifically require calibration because the samples are compared to each other, and are measured in relation to each other in terms of disintegrations per minute (DPM). Nevertheless, putting a known concentration of cable oil into the scintillation counter can be used to derive a calibration curve. Figure 3.7 shows a typical calibration curve for the scintillation counter.
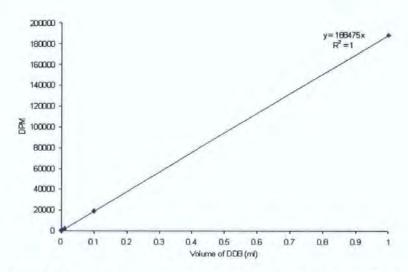
Figure 3.7 **A typical calibration curve for the scintillation counter using 14C cable oil.**

Quenching is the reduction of the pulse voltage by material present in the sample or scintillation mixture. The scintillation counter used for this study automatically corrects for quenching.

3.2.5 Reproducibility

After testing the extraction efficiency it was necessary to test the reproducibility of results obtained from the scintillation counter. With the scintillation counter used in this study it is possible to make the same rack of samples run continuously. By doing this it is possible to determine the reproducibility. Averages of 12 samples were taken which produced a relative standard deviation of 1.55%.

3.3 Determination of Bromide & Phosphate in Soil Leachate – Air Segmented Continuous Flow Analysis.

The aqueous samples produced by the automated lysimeter described in Chapter 4 were analysed for tracers introduced into the soil block. The tracers to be determined in this study were bromide and phosphate. These species were chosen for their contrasting behaviour in the soil matrix. Bromide is a conservative tracer due to its low level of interaction with the soil mineralogy, whereas phosphate is known as a non-conservative tracer, due to its tendency to bind and interact with the soil components particularly by adsorption onto clay particles.

Several analytical methods are available for the determination of dissolved species in soil leachate e.g. inductively coupled plasma-atomic emission spectroscopy (ICP-AES), inductively coupled plasma-mass spectrometry (ICP-MS), high-pressure liquid chromatography and titrimetry. Each of these methods has associated advantages and disadvantages. For example the utilization of atomic spectrometric methods, gives high accuracy and good detection limits, with the drawbacks of only moderate sample

throughput and high instrument maintenance and setup/ optimization time and high running costs. A low cost technique such as titrimetry, is reliable, but lacks the rapidity of other automated methods. The main methods for the determination of bromide and phosphate are spectrophotometry and ion chromatography. As such a method using spectrophotometry has been utilised in this study as described below.

Air segmented flow analysis (SFA) has found a wide range of applications in research (Gardolinski, 2001), routine analysis and the teaching of analytical chemistry. Its inherent versatility has allowed it to be adapted to the different detection systems of electrochemistry, molecular spectroscopy and atomic spectroscopy, using a wide variety of manifold configurations. SFA systems have also been designed to dilute or preconcentrate the analyte; to perform separations based on solvent extraction, ion exchange, gas diffusion or dialysis; and to prepare unstable reagents in situ. Figure 3.10 is a diagram of the segmented flow stream, with air preventing diffusion of the reaction along the reagent stream.
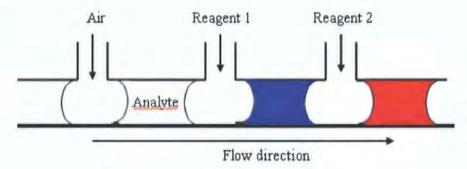
Figure 3.8   Schematic of segmented reagent stream

Air segmented flow analysis is based on the injection of a known quantity of liquid analyte into a reagent stream separated by air bubbles. The injected sample forms a zone that is transported towards a detector continuously recording absorbency at a given wavelength. The Skalar SAN^{plus} systems air bubbles prevent diffusion of the analyte within the manifold reagent stream. Each segment is then an isolated micro reaction.
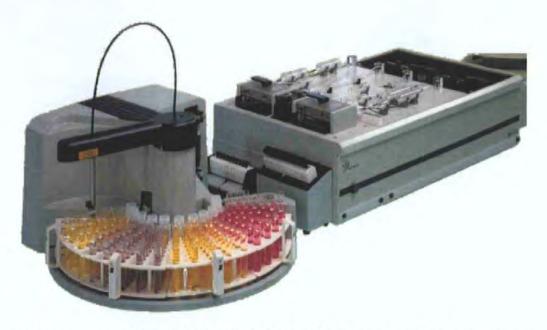
Figure 3.9 Photograph of the main Skalar SAN^{plus} chemistry unit, with autosampler.

An advantage of the Skalar SAN^{plus} system is the multi-analyte capability. In this study phosphate and bromide were analysed simultaneously from the same sample. Other species such as nitrate, nitrite or silicate can be determined with the addition of other manifolds to the base chemistry unit.

Parameter	Specification
Lamp	Halogen, 6V / 10W cooled
Spectral range	340-1100 nm
Optical path length	50 mm
Concentration range (reported)	20-100 μg L^{-1} P 1-50 mg L^{-1} Br
Sample time	60 s
Wash time	60 s
Injected air	30 bubbles/min
Sample through-put	30 samples/h

Table 3.3 Specifications of instrument parameters on the CFA manifold for the determination of Br$^-$ & PO$_4^{3-}$.

This unit (SA 4000) consists of a 4-channel module holder and two 16 channel proportioning pumps. Separate chemistry modules and detectors with automatic background correction (6250 Matrix) were used for each analyte. Incorporating a robotic autosampler enhances the analysis capabilities, with a sample capacity of 140 samples. The computer also corrects for baseline drift by analysing a known standard at an interval defined by the user, using this data to auto calculate and correct all results for baseline drift.

77

3.3.1 Experimental Determination of Bromide

The chemistry used for the SFA manifold is based upon the stepwise conversion of bromide to bromate, which when combined with rosaniline forms tetrabromorosaniline; a method introduced by (Hunter & Goldspink, 1956). This method is not subject to interferences from other common halides. Bromide is quantitatively oxidised to bromate in a sodium orthophosphate buffer solution; Equation 3.1.

$$Br^- + 3ClO^- \longrightarrow BrO_3^- + 3Cl^-$$

Equation 3.1   Oxidation of Bromide.

The oxidation is carried out in the presence of hypochlorite. In an acid alcoholic solution bromate quantitatively yields six equivalents of bromine in an excess of bromide; Equation 3.2.

$$BrO_3^- + 5Br^- + 6H^+ \longrightarrow 3Br_2 + 3H_2O$$

Equation 3.2   Br reduction yielding six equivalents Br.

A red solution is formed by bromine substitution in rosaniline ($C_{20}H_{20}ClN_3$) decolourised by acid. Subtracting the absorbance at a reference wavelength 660 nm from the absorbance at the analyte wavelength (570 nm) corrected for refractive index effects.

3.3.1.1 Reagents

All solutions were prepared in ultra-pure water (Milli-Q, Millipore Corporation) and all reagents were of AnalaR (or equivalent) grade and were purchased from BDH, UK unless indicated otherwise. Standards in the range of $10 - 50$ mg L^{-1} were prepared by serial dilution of a stock 1000 mg L^{-1} solution of KBr (1.10469 g in 1 L of Milli-Q). FFD6 and Brij 35 are nutrient free detergents supplied by Skalar UK.

The bromide reagent streams were:
1. hydrochloric acid (50 mL L^{-1} and 3mL L^{-1} Brij 35% (Skalar))
2. sodium dihydrogen-orthophosphate solution (200 g L^{-1} NaH_2PO_4)
3. sodium hydroxide solution (28 g L^{-1} NaOH & 3 mL L^{-1} FFD6 (Skalar))
4. hypochlorite solution (low in bromine < 10 ppm)
5. 50% sodium formate solution (50 g 0.1 L^{-1})
6. propan-2-ol
7. sulphuric acid solution (3.5M) (195 mL L^{-1} H_2SO_4)
8. stock solution bromide molybdate (150 mg L^{-1} KBr, ammonium molybdate 3g L^{-1} ($NH_4)_6Mo_7O_{24}.4H_2O$).

9. Fuchsine solution (Fuchsine basic 30 mg 0.5 L^{-1} $C_{20}H_{20}ClN_3$ & 28 mL H_2SO_4 0.5 L^{-1}).

10. Sulphuric acid solution (7M, 389 mL L^{-1} H_2SO_4.)

The final colour reagent was produced fresh each day by mixing 100mL bromide molybdate[8], 500 mL fuchsine solution[9] and 400 mL sulphuric acid[10]. The solution should be stored in a dark bottle.

3.3.1.2 Manifold Design and Reagent Addition Procedure

Each sample was acidified with hydrochloric acid solution in order to produce Br$^-$ anions. This was then dialysed against a sodium orthophosphate solution. The dialyser utilised a membrane of <2 µm pore size as well as heating the acid/sample solution at 90 $^{\circ}$C through an in-line reaction chamber. The membrane permitted the diffusion of chloride and bromide ions into the buffer stream.

Additional chloride ions were added by sodium hypochlorite addition, which aids the oxidation of any metals present in a low valency state, ensuring all bromide is available for the reaction. The excess chloride ions were then removed by the sodium formate solution. The stream was passed through a reaction coil heated to 60 ^{0}C by a continuously circulated water jacket. At this point a resample was taken and the excess sample transferred to the waste outlet. Colour reagent (acidified rosaniline) was added and allowed to pass through a short reaction coil before propan-2-ol (100%) and H_2SO_4 (7 M) were added in turn. Figure 3.10 is a diagram of the bromide manifold and reagent addition

procedure.
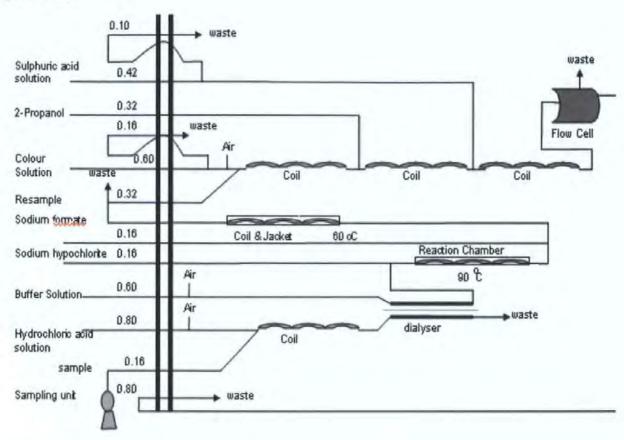
Figure 3.10   Schematic Representation of the Bromide Manifold

3.3.2 Manifold Performance

The software was pre-programmed with the standards to be used. The highest standard concentration was set to a maximum absorbance of approximately 2500 counts. The absorbance values for the known standards were then used to calculate the absorbance found from the unknown samples.

The first peak observed in the output trace in Figure 3.11, the tracer or highest expected concentration is used to calibrate the linear range of the analysis. This peak is encountered after approximately 1250 seconds. Therefore it takes twenty minutes approximately for each sample to move from the injection point to the detector. For flow analysis this is an extremely long residence time and is due to the slow kinetics of the reaction.
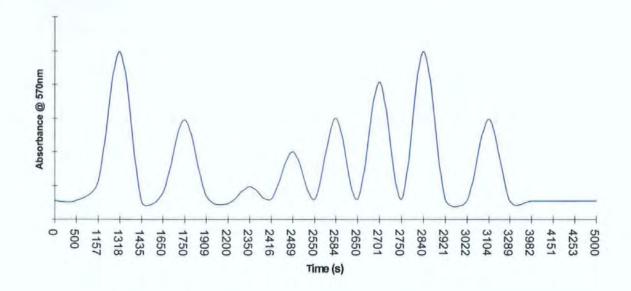
Figure 3.11   An output trace from the flow analyser.

As the runtime for a full carousel (140 samples) was 5 hours, the instrument automatic baseline correction facility was used by analysing a control sample (typically every 10th sample) to correct for drift. Drift is caused by wearing of the peristaltic tubing during the experiment, changes in temperature of the reagents and degradation in air of the reagents.

3.3.2.1   Linearity

The bromide manifold had an acceptable linear range of 1 - 120 mg L^{-1}. Figure 3.12 is a calibration of the bromide SFA manifold up to 120 mg L^{-1}.

$$y = 30.066x$$
$$R^2 = 0.9989$$
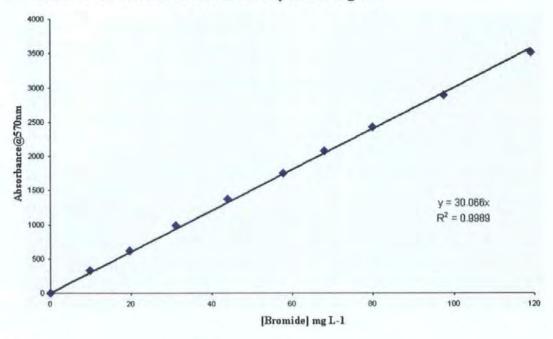
Figure 3.12   Linear range of the Skalar Bromide Manifold.

The lower end of the linear range was affected by the age of reagent pump tubing and the age of the dialyser membrane. Due to the length of the manifold the demands on the pump tubing were much greater and any wearing of a tubing in a section of the manifold would quickly cause the manifold reagent streams to become imbalanced. This fault was easily

81

and rapidly resolved by replacing the tubing. The dialyser membrane, after a prolonged set of determinations, affected the quality of baseline developed. This was due to a build up of colloidal material on the membrane surface. The membrane was therefore replaced or cleaned after every run.

3.3.2.2 Throughput

The robotic auto-sampler and online calibration, at regular intervals throughout the analysis, provided the instrument with the ability to analyse bromide and phosphate simultaneously, and auto-calculate and correct the results; providing a throughput of about 140 samples every 8 h. The duration of the analysis can be several hours and if many samples are being analysed shadow effects, e.g. a build up of analyte in the system, sorption or precipitation onto the walls of the manifold, may cause a drift in the baseline. To overcome this a control was re-analysed every 10 samples to give a fixed point for sample correction.

The complexity of the manifold meant that careful observation of the peristaltic pump tubing had to be maintained and replaced when necessary. It was also observed that precipitation increased over time in the reaction coil immediately after colour reagent was added to the sample stream. This however was easily removed after each analysis by flushing with 0.5 M sodium hydroxide solution.

3.3.2.3 Analysis of Soil Leachate Samples

A detailed discussion of the analysis and interpretation of the bromide results is given in Chapter 5. However shown below in Figure 3.13 are the breakthrough curves for each of the soil blocks analysed. The flux rate is calculated by multiplying the concentration of bromide by the volume of the sample analysed.
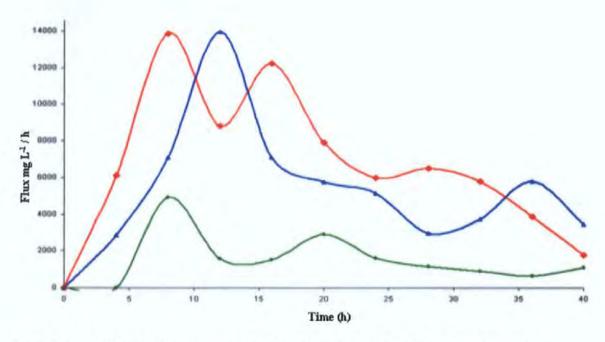
Figure 3.13   Bromide Breakthrough Curves (red Crediton , blue Sollom, green Conway)

As shown in Figure 3.13 the bromide breakthrough curves clearly show fluctuations in the concentration of bromide leached from the soil block. The sandiest soil (Crediton) is the quickest to breakthrough (8 hours maximum peak) followed by the Sollom soil (12 hours maximum peak) and then the Conway soil (8 hours maximum), which is the soil with the highest clay content. Although the Conway soil achieved maximum value earlier than the Sollom soil it had a much lower flux value (approx. 4000 mg L^{-1}/h compared to 14000 mg L^{-1}/h Sollom). This suggests that water (and therefore bromide) is being retained by the clay soil.

3.3.3 Experimental Determination of Phosphate

Phosphorus in soil water leachate and runoff occurs in both dissolved and particulate forms (Rege and Fogler, 1987). Dissolved species are considered from an operational standpoint to be the fraction that passes through a 0.45 μm filter membrane. The dissolved fraction contains compounds such as orthophosphates, inositol phosphates, nucleic acids, sugars and condensed phosphates. The arbitrary nature of the operationally defined 0.45 μm filtration process means that some colloidal phosphorus will be present in the dissolved fraction.

Total dissolved phosphorus (TDP) can be operationally divided into phosphorus compounds that are molybdate reactive, i.e. dissolved reactive phosphorus (DRP), and unreactive forms of phosphorus including dissolved condensed phosphorus (DCP) and dissolved organic phosphorus (DOP).

Traditional methods to determine total phosphorus (TP) and TDP involve sample heating or autoclaving with peroxydisulphate alone or with acid peroxydisulphate (Ahmed *et al.* 1993). These methods may give incomplete recoveries for some samples, and the use of nitric - sulphuric or nitric-sulphuric-perchloric acid mixtures may be required (Sharma and Yortsos, 1987). However these methods although generally accepted as being analytically reliable, involve extensive sample handling and lengthy digestion times of up to 2 hours, making them tedious when large numbers of samples are to be analysed. The majority of manual and automated methods of phosphate determination are based on the spectrophotometric determination of phosphorus as phosphomolybdenum blue.

Many modifications of this method have been reported, usually involving use of reductants such as tin(II) chloride, ascorbic acid, 1-amino-2-napththol-4-sulphonic acid, sodium sulphite, hydrazine sulphate, or combinations thereof (Broberg, 1988); or different acid strengths in attempts to improve selectivity and stability of the chromophore produced (Armstrong, 1972). The most widely-used methods for batch and automated analyses are based on the method of (Murphy, 1962) which utilise ascorbic acid reduction with a potassium antimonyl tartrate catalyst. The method suffers little interference from silica, which is, however, a common problem in many other phosphomolybdenum blue based procedures. Ascorbic acid is preferred to tin(II) chloride as the reducing agent in batch analysis because the reaction is less salt and temperature sensitive and a more stable chromophore is produced (Harwood, 1974).

3.3.3.1 Reagents

The phosphorus reagent streams were:

1. ammonium molybdate solution comprising 230 mg L^{-1} potassium antimony tartrate, 6 g L^{-1} ammonium molybdate, 69.4 mL L^{-1} sulphuric acid and 2 mL L^{-1} FFD6 (Skalar).

2. The ascorbic acid solution contained 11 g L^{-1} ascorbic acid, 60 mL L^{-1} acetone and 2 mL L^{-1} FFD6.

3.3.3.2 Manifold Design and Reagent Addition Procedure

Phosphate addition procedure involved the addition of ammonium molybdate and then potassium antimony tartrate to the sample stream under acidified conditions; Equation 3.3.

$$PO_4^{3-} + 12MoO_4^{2-} + 27H^+ \longrightarrow H_3PO_4(MoO_3)_{12} + 12 H_2O$$

12-phosphomolybdic acid

Equation 3.3   Production of phosphomolybdic acid intermediate

This forms an antimony phosphomolybdate complex. This complex is reduced to an intensely blue-coloured complex by ascorbic acid Equation 3.4.

$$H_3PO_4(MoO_3)_{12} \xrightarrow{\text{Reduction}} \text{Phosphomolybdenum Blue}$$

Equation 3.4   Final reduction producing phosphomolybdenum blue.

Figure 3.14 is a schematic representation of the Phosphate continuous flow analyser manifold.
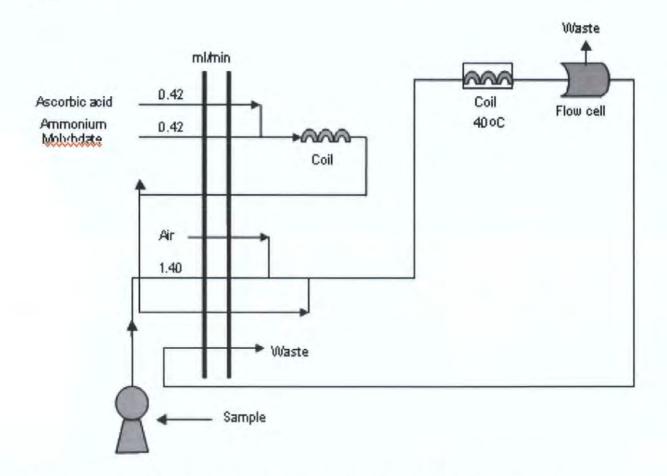
Figure 3.14   A schematic representation of the phosphate manifold and Reagent Stream.

3.3.4 Manifold Performance

The software is pre-programmed with the standards to be used. The absorbance values for the known standards were then used to calculate the absorbance found from the unknown samples. A typical calibration produced by a set of known standards is shown in Figure 3.15. Subtracting the absorbance at a reference wavelength (1100 nm) from the absorbance at the analyte wavelength (880 nm) eliminated refractive index effects.
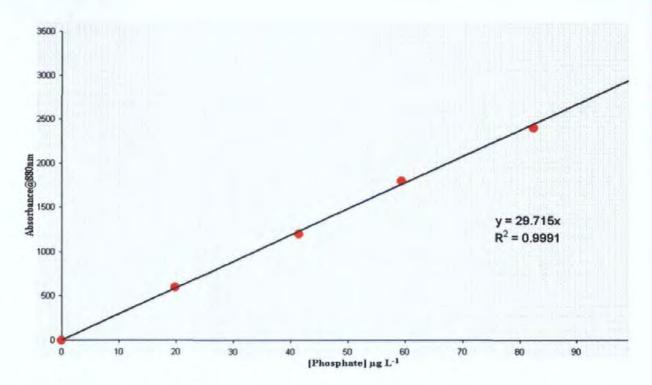
Figure 3.15   Typical calibration from the Phosphate CFA manifold.

The simple layout of the phosphate manifold made it much more robust than the bromide manifold. However it was essential for the manifold to be flushed for at least 20 min with distilled water or 0.5 M HCl, after prolonged use as the molybdenum blue would precipitate onto the tubing, requiring all tubing to be replaced.

3.3.4.1 Linearity

The linearity for the phosphate channel was from 2 μg L^{-1} up to 200 μg L^{-1} (Gardolinski, 2001).

3.3.4.2 Throughput

Analysis time for the phosphate manifold alone would was 2 minutes per sample. However due to running in parallel with the bromide channel the total batch throughput was restricted to the speed of the slowest manifold i.e. bromide.

3.3.4.3 Analysis of Soil Leachate Samples

Phosphate results are discussed further in Chapter 5. However Figure 3.16 shows the breakthrough curves for the phosphate tracer as analysed and converted into flux rates. Unlike the bromide curves, the phosphate curves appear to have much more unpredictable behaviour.

86
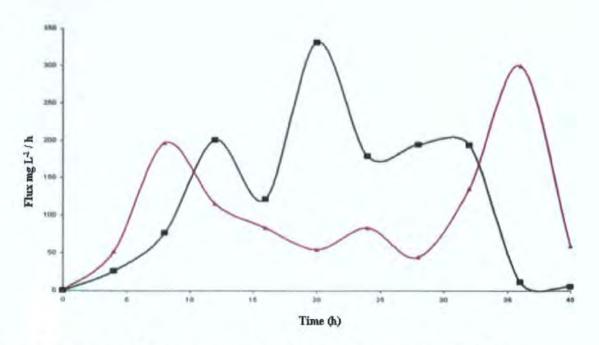
Figure 3.16   Phosphate Breakthrough curves for (black Crediton and purple Sollom)

The Crediton phosphate sample is markedly slower than the bromide to be eluated from the soil block. The Sollom soil series however has a faster initial peak (8 hours as compared with 12 hours for PO_4^{3-} in the Crediton soil), with both soils having a second successive higher peak (20 hours Crediton and 36 hours Sollom). This increased complexity of behaviour is described in further detail in Chapter 5. The increase in phosphate soil interaction complexity is due to the higher interaction of the phosphate with the soil than the bromide which is a conservative tracer. It should also be noted the much lower flux rate at which the phosphate is released from the soil block, when compared to the bromide despite the same initial mass being applied to the surface of the block. This suggests that a lot more phosphate is retained in the soil matrix, sorbing or binding to the mineral structure of the soil.

3.4   Summary

This chapter has been concerned with the development of protocols and suitable analytical techniques to analyse:

i)   Oil, soil and water mixtures for the quantitative determination of oil concentration

ii)   Aqueous leachate samples for the determination of bromide and phosphate tracer concentrations

The high sample output of the automated lysimeter (described in Chapter 4) required rapid and reliable analysis of hundreds of samples. During each experiment the automated lysimeter was capable of generating 2000 aqueous samples and 250 soil samples per block. Therefore rapidity and robustness of the analytical apparatus was paramount. The regular

calibration of the instruments and automated data processing allowed the data to be interpreted and processed quickly and with confidence.

Each of the problems as listed in Table 3.4 has been overcome. Sample storage was solved by the use of high throughput analytical methods. The samples could be loaded directly into the SFA carousel in preparation for analysis. Tracking needs were greatly reduced as sample storage was dispensed with.

Problems	Solution Found	Comments
Sample Storage	✓	No Long Term Storage
Sample Tracking	✓	No Need as Not Stored
Reproducibility	✓	Consistent Calibrations
Throughput	✓	Satisfactory Throughput
Economics	✓	Inexpensive Reagents
Disposal	✓	No Harmful Chemicals*

*The radiolabel used in the oil tracer, was at a low enough level to dispose of in general refuse, providing adequate documentation was kept.

Table 3.4   Problems Encountered and solutions found indicated by a tick in the central column.

All reagents were easily disposed of. The phosphate and bromide reagent streams were disposed of through a drainage system into the main drain. The radio labelled soil and scintillation samples were disposed of as regular refuse, providing regular records were taken.

Coupling the automated sample collection with a series of automated analytical methods allowed large amounts of data to be produced which is of the best quality available.

4 Design, construction and automation of a precision 3-D lysimeter (Johnson, Mathews, *et al.*, 2003)

4.1 Objectives

Large scale lysimeter experiments can suffer from loss of resolution due to sample homogenisation at the point of collection. The objective of this study was to construct an apparatus which produced results at high spatial precisions and was capable of handling a large number of samples generated by such an investigation.

4.2 Design of the automated lysimeter

A well established technique for characterising preferential water and solute movement is the use of instrumented intact soil cores or blocks (Lewis, 1990), (Isensee, 1992) and (Tindall, 1992). Inherent in the successful use of this method, however, are several difficult and critically important steps, including the choice of block size, the use of effective techniques for isolating, transporting and storing the block, and the instrumentation of the block with appropriate, effective solution delivery, collection and monitoring systems.

In this project an apparatus was constructed for measuring the effects of NAPL injection and subsequent 2-dimensional flow of LNAPL through a half metre soil block. This experiment was accompanied by an investigation of the effects of the LNAPL on the conductivity of the soil to the aqueous tracers orthophosphate and bromide. These are non-conservative and conservative tracers respectively. Many experiments were performed using soil cores, concentrating on vertical flow without measuring lateral movement. The half metre cube allowed a suitable amount of lateral migration to take place, while remaining at the laboratory scale to control the environmental variables encountered. It also avoided the danger of releasing NAPL in the field, which is normally hazardous for health and safety reasons. The scale is of practical use for those wishing to upscale properties for purposes such as waste management and pollution prediction.

Rainfall was delivered to the surface of the soil block using a rainfall simulator, and sample collected at the base of the soil block using a precision-machined collection plate. The rainfall provided the soil block with a steady supply of water to establish flow channels within the block and to allow the investigation of L-NAPL behaviour under these conditions as it dispersed through the soil block. Time domain reflectometry probes (TDR) were used for non-destructive in-situ measurement of volumetric water content.

89

In each of the soil types, tracer (bromide and phosphate) migration was studied prior to and after oil injection.

4.3 Design and Construction of the lysimeter

The purpose of the apparatus was to provide a superior temporal and spatial analysis of leachates from large intact soil blocks, under controlled laboratory conditions, with the objective of generating sufficient experimental data to validate mechanistic models developed to predict pollutant movement through soils. The lysimeter was constructed of square section steel tubing, with the soil block located in the centre of the rig and the rainfall applicator directly above it. Figure 4.1 is the design view of the lysimeter.
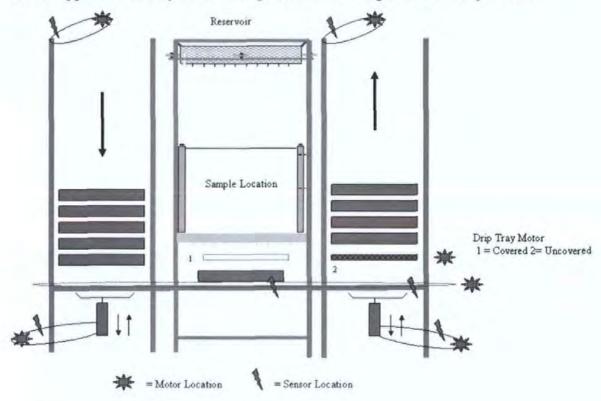
Figure 4.1   Diagram of automated lysimeter

4.3.1 Eluate Collection

With regard to sample collection other researchers have used apparatus such as ceramic plates (Butcher and Gauthier, 1994) and plastic or metal grids like open trays (Dexter 1995); (Andreini and Steenhuis 1990) but none have reported the use of automated sample collection. Figure 4.2 shows the top view of the collection plate, which was precision machined from anodised aluminium by computer numerate control (CNC). Square funnels with an edge of 38mm length were machined into the block in a 10x10 array.

Figure 4.2   **Sample Collection plate top view.**

Well-defined boundaries reduced the possibility of sampling ambiguity between collection funnels. Each square funnel was filled with glass wool to prevent movement of the soil into the funnels. To prevent samples being biased by edge effects, the machined lysimeter plate had four drainage channels running along each side of the plate. They were 63mm in width and isolated the central zone of the soil block from which experimental samples were taken. Any water entering the edge channel was removed to waste. The drainage channels left an active surface 380mm x 380mm, from which the soil eluates could be collected.

4.3.2 Rainfall Distribution

A method of applying water to the surface of the soil block was required that gave an even distribution over the sample surface. Studies conducted by other authors using spray nozzles found that the uniformity of application deteriorated with horizontal distance from the nozzle (Chow and Harbaugh, 1965). Therefore it is now more common in the laboratory to use an array of needles.

The rainfall simulator comprised a square reservoir constructed from PVC with dimensions 451 x 451 x 114 mm, Figure 4.3. An adjustable constant-head device was used to supply the water in this apparatus, although other workers have regulated the supply in a closed supply system (Chow, 1965); (Romkens, 1975). It was found that the syringe needle array had to overlap the sample, as discussed below.

The mechanism for providing a degree of x-y translation to the rainfall delivery system took the form of an electric motor that turned a vertical brass rod, upon which a cam was mounted. The cam turned within a PVC ring attached to an edge of the rainfall reservoir,

which was supported on roller-ball bearings running on horizontal metal plates. This arrangement could be connected to a similar cam on the other side of the apparatus via a chain drive, Figure 4.3. Other workers have used more complicated stepper motor arrangements (Romkens, 1975), but these do not produce greater uniformity than the apparatus described here.
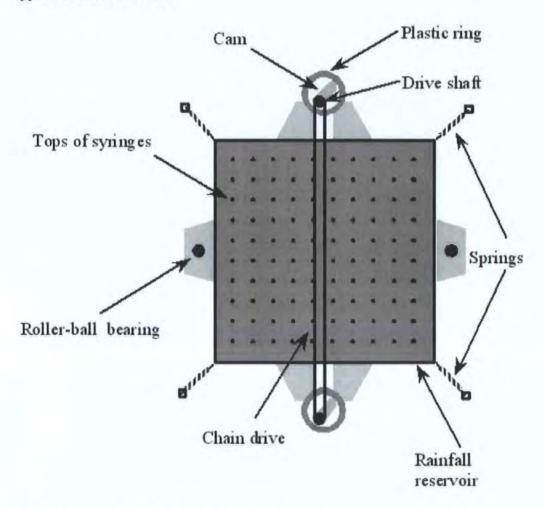
Figure 4.3   Rainfall Simulator from a top down view

(Mathews, 1999) discovered that the choice of needle gauge size was crucial with this type of rainfall simulator. They discovered that where the diameter of the needles was too small it proved impossible to keep the needles flowing. Where the needles were too large, a flow equivalent to rainfall of more than 20 mm an hour was generated. The needles used were 23G needles (I.D. 0.318mm, Richards, Leicester, UK). Needles that did not flow, due to inconsistencies in the manufacturing process, were replaced with new ones, producing an application rate of 6.4 mm h^{-1}. All 100 needles flowed constantly, unaided, over two days, with uniformity discussed below in section 4.2.1.3.

4.3.3 Uniformity of Application

(Mathews, 1997) study with the addition of a second cam, an increase of the needle array to 12 x 12 and the introduction of the 2 mm mesh showed that the rainfall simulator had a

relative standard deviation of 8.8%. This compares favourably with the results achieved by other researchers, Table 4.1. The introduction of a larger array of needles prevented the edge regions from drying out.

Workers	RSD %	Uniformity Coefficient, %
Mathews and Matthews (1999)	8.8	93.04
Bowman et al. (1994)	n/a	>98.00[1]
Dexter (1995)	19.0	-
Phillips et al. (1995)	11.6 – 22.4	-
Romkens et al. (1995)	8.5[2]	-
Andreini & Steenhuis (1990)	n/a	94.08 [3]

Table 4.1   Homogeneity of application of various rainfall simulators.

[1] No details given except that this figure is for rainfall rates in the approximate range 5-25 mm hour^{-1}.
[2] Average of five figures carried out at five different rainfall rates.
[3] Average of four figures each of which is an average of the 'before' and 'after' values for an experiment.

4.3.4 Automation of the lysimeter

Sample collection utilised 6 electric motors (M1 to M6) of varying type (220V DC and 24V AC, Parvalux, Brighton, U.K.), Figure 4.1 illustrating the motor locations. Heavy-duty electric breaks were added to the tower lifting and lowering motors, as the weight of the loaded sample trays would otherwise have caused slippage when the power was released. The main lifting motors were 220 V D.C. and therefore power was converted from 240 V mains A.C. using a series of rectifiers. Logic level operations to activate the motors were isolated from the high voltage circuitry to allow computer control of the equipment. Figure 4.4 is a schematic layout of all the interface circuitry. Motor activation/deactivation and sensor signals were processed by a DIO24 TTL card (Digital input / output card, National Instruments, UK) feeding signals to a specially written PC-based LabVIEW™ software (National Instruments) virtual console. This console could be run manually or set to automatic operation.

The palettes moved from being stored on the left of the apparatus to the sampling area underneath the soil sample, and after a user defined time (usually 4 hours) the samples were moved to the right storage tower.

The arrows indicated in Figure 4.1 show the movement path of sample palettes around the apparatus.
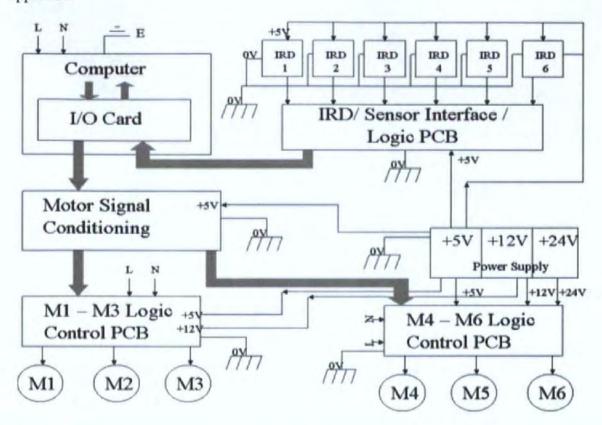
Figure 4.4   A Schematic layout of the circuitry, IRD = Infra-Red Detector, M=Motor.

Figure 4.5   Photograph of the circuit as described in the above schematic

Palettes were tracked using infrared sensors, which were triggered by the palette movement through the infrared detection beams. Infrared sensors were also used to monitor tray position by counting chain links, as shown in Figure 4.6.

Figure 4.6   Infra red measurement sensor

Funnels protruded from the base of the machined grid lysimeter plate. To prevent cross contamination of samples a drip tray was automatically inserted under the funnels during palette changeover and then removed when the sample palette was in position. Palette movement was achieved by a series of chain belts into which the sample trays were mounted. Each sample palette comprised a stout PVC tray with the gripping areas machined out of plate steel and attached to the corners of the palette. The upper surface of each palette was drilled with a 10x10 grid of holes to hold sample collection vials. The cylindrical glass vials (BDH, UK) were 30ml in volume and 25mm in diameter. The centre of each vial was located below a funnel through which soil eluate could flow.

The computer interface was booted up before power was applied to the lysimeter, as this set the control logic of the motors, which is an important safety feature.

4.3.5 Time Domain Reflectometry

Determination of moisture content is crucial in any migration study. Soil water content is a key variable in most types of soil study including agricultural water management and hydrological modelling.

The standard method of measuring the volumetric water content of a soil sample is the thermogravimetric method. This consists of determining the weight loss after a specified time of oven drying at 105 °C and relating it to the volume of water for a given measurement. This method is time consuming and destructive to the sampled soil. It cannot therefore be used for repetitive measurements at exactly the same location. However, this method is invaluable for calibration of alternative, less intrusive methods.

Other techniques for in situ measurements of volumetric water content include neutron probe and gamma attenuation methods. These approaches are non-destructive, except for the initial installation of tubes and comparatively fast. However, both methods involve radiation that has a consequential environmental impact and was therefore considered unsuitable for these experiments. Moreover, neutron probes require soil-specific calibration, and ordinary field gamma probes are relatively imprecise (Roth *et al.*, 1990).

Time Domain Reflectometry (TDR) has become a popular and recognised method of measuring the water content of soil. The use of TDR for measuring soil water content was originally proposed by Davis and Chudobiak, (1975) and subsequently used in later studies by Davis and Annan, (1977) and Topp, Davis, and Annan, (1980). The technique is based on measuring the velocity of a pulse, which travels along an electromagnetic transmission line as a guided wave. The pulse velocity is used to calculate the dielectric constant of soil, which is dominated by the contribution from soil water. Free water has a dielectric constant about 20 times greater than that of mineral matter, and so the effect of the mineral matter on the pulse velocity is small, (Whalley, 1993). Cable oil has a dielectric constant of 2 (Horvath, 2000). A comprehensive review of its development is given by (Gardner *et al.*, 1991).

The principle of TDR is that a high frequency electromagnetic pulse is fed into the soil between two metal rods. Part of the pulse is reflected back up through the soil from the bottom of the rods, and the time interval between the incident and reflected pulses is measured, (Smith and Mullins, 1991). Topp, Davis, and Annan, (1980) determined a third order polynomial relationship between dielectric constant, ε_c, and volumetric water content θ, for which they gave an error estimate of 0.013 for θ.

$$\theta = -5.3 \times 10^{-2} + 2.92 \times 10^{-2}\varepsilon_c - 5.5 \times 10^{-4}\varepsilon_c^2 + 4.3 \times 10^{-6}\varepsilon_c^3$$

Equation 4.1

The main advantage of this calibration equation is that it does not require the determination of any additional soil parameters. The dielectric constants were calculated from the pulse velocity assuming that the imaginary part of the dielectric constant was negligible. The calibration suggested by (Topp *et al.*, 1980) was widely accepted and thought to be substantially independent of soil type (Whalley, 1993).

Pairs of TDR probes, in the form of 3 mm diameter stainless steel welding rods (Rightons, Plymouth, Devon, U.K.) spaced 20 mm apart and connected to the Tektronix 1502C cable tester, were inserted through holes drilled in the sample container at various depths

throughout the samples. At each depth two pairs of probes of two different lengths were inserted, one pair of length 100 mm the other of 300 mm. The pairs of TDR probes were located at depths shown in Figure 4.7 from the base of the sample. This arrangement allowed monitoring of the water content across the whole width of the sample and also across the region closest to the edge of the container directly over the edge flow channels of the grid lysimeter.
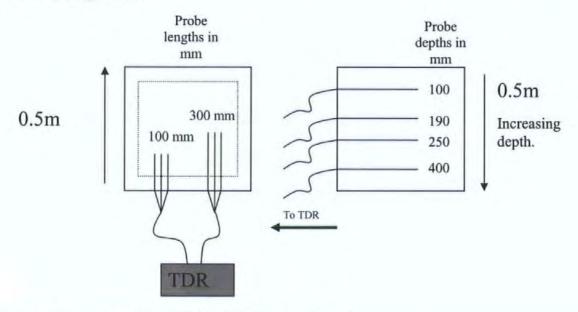
Figure 4.7   **Location of TDR tridents in each soil sample**

Figure 4.8 shows the TDR probes installed into a sample block.
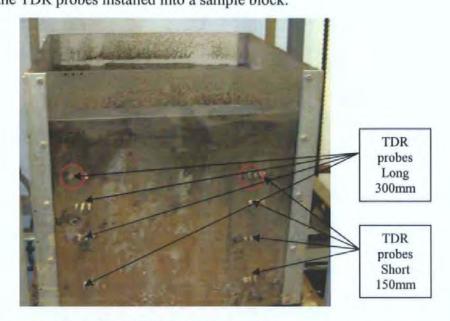
Figure 4.8   **A saturated soil sample with TDR probes mounted.**

4.4   Experiment Protocols for the Lysimeter

4.4.1   Extraction and preparation of soil blocks

The 2-dimensional investigation necessitated the extraction of 0.5 m^3 cubic soil blocks, as described in section 2.3.2. The experiments were conducted to observe the effect of soil

texture on oil distribution in three half-metre cubes. The experiment also investigated the affect the oil has on the transmissive properties of the soil block to Br^- and PO_4^{3-} (orthophosphate) tracers. Each of the experiments involved the analysis of a tracer pre-oil injection, oil injection and post-oil tracer analysis.

Saturation of the sample took place prior to commencement of a transport experiment. The sample was typically saturated over a period of three to four days using the rainfall simulator. The TDR probes revealed when a consistent saturation level had been reached. Rainfall was continuous throughout the duration of the experiment at a rate of approximately 6.4 mm h^{-1}.

It was thought unnecessary to completely saturate the sample from the bottom up, as none of the soils were taken from areas where the water table aggressively filled the extraction sites. Complete saturation of the sample may have lead to uncharacteristic movement in the soil blocks and disruption of preferential flow pathways. Saturation was deemed to be complete when water flowed from the base funnels. When the number of base funnels flowing stabilised and the TDR probes were stable the experiment could commence. During bromide application it was important that any disturbance to the flow regime was kept to a minimum. This was complicated by the requirement that the individual needles needed to be 'primed', pumping water through to remove trapped air. Priming of the needles was carried out by injecting a small amount of water into any blocked needles, using a hypodermic syringe.

4.4.2 Water Flow Velocities

Water flow velocities were measured by collecting water samples every 4 hours from underneath the collection grid, using the automated sample collection. Figure 4.9 shows a sample tray underlying the lysimeter collection area. The samples were then analysed for bromide and orthophosphate.

Figure 4.9   Sample Collector and collection tray

4.4.3 Oil Tracer Analysis

Details of oil synthesis and the analysis technique were described in Chapter 3. The oil injection took place on the surface of the soil by means of a 68 mm diameter plastic pipe inserted into the middle of the container. The pipe was pushed 3cm down into the sample, to prevent oil moving laterally on the sample surface. Oil was then poured into the tube. For each of the experiments, 75 mL of oil was used. After 8 hours the second tracer analysis experiment began, repeating the above procedure. For the oil analysis sampling was undertaken using a 2 cm internal diameter steel gouge auger (Van Walt Limited, Haslemere, Surrey, U.K). Figure 4.10 is a plan view of the sampling regime.
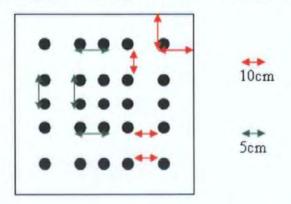
Figure 4.10   The sampling Regime for the soil cores

The auger was twisted into the sample removing a 2cm core from the sample block. The sample was removed in sections, weighed into 5 g samples and stored in glass vials (with a volume of 28.25 mL) until analysis was performed. A sampling grid comprising 250 sample points was utilised in the augering process. From each augered column 10 samples were taken at 5cm depths. A total of twenty five columns were removed from each soil block. Analysis, as described in Chapter 3, was carried out using a Beckman LS500 scintillation counter.

4.4.4 Aqueous Tracer Analysis

A combined tracer was produced by dissolving 1.2 g of KBr (AnalaR grade, BDH, UK) and 3.4 g K_2HPO_4 in 100 mL of water. This concentrated solution was applied to the surface of the soil block using a 68 mm plastic drainage pipe pushed 3cm into the sample. The migration of Br^- and PO_4^{3-} tracers was measured over the 0.5 metres vertical distance of the soil block. In this investigation an air segmented flow analyser (Skalar SAN^{plus}® Skalar, Breda, Holland) was used to determine Br^- and PO_4^{3-} concentrations, as detailed in section 3.3. Samples were collected in 25mm x 70mm disposable glass sample vials (BDH, UK).

4.4.5 Lysimeter Testing and the Effects of Re-Packing On Soil Samples.

4.4.5.1 Experimental Preparation

Although all of the 0.5 m samples were extracted intact, it was considered appropriate to check the extent of repacking. So a repacked 0.5 m cube sample was also studied. For the repacking experiment a quantity of the Crediton series soil was transported back to the laboratory. The dry soil was loaded into the container, and hand-compacted in layers with a 10 cm^2 hand pommel. Each layer was no more than 7 cm in depth. The preceding layer was 'keyed' into the next by raking the surface of the compacted layer. Samples were then loaded onto the specially constructed automated lysimeter. The samples were mounted and saturated from the bottom up. Bottom up saturation was used in this experiment for compatibility for field trials conducted at Cranfield by the NGT, which were using bottom up saturation. This saturation would not effect later analysis as in this study a bulk breakthrough was being collected and no recording of preferential flow paths using the machined plate was undertaken. A conservative bromide tracer was introduced and the leachate collected from the base of the soil block using a rotary autosampler.

4.4.5.2 Results

The breakthrough curves for Crediton intact and repacked soil are shown in Figure 4.11. The intact Crediton sample was found to have an extremely asymmetric breakthrough curve. The maximum concentration of 22 mg L^{-1} bromide eluted at the base of the soil block was reached at the 1000 minute mark for the intact Crediton sample. The sample distance was traversed by the bulk of the bromide tracer within the 120-2500 minute time period. The Crediton repacked sample took approximately twice this amount of time and shows a more extended curve. The repacked sample reached a higher bromide concentration of 24 mg L^{-1} at 2100 minutes, with the bulk of the tracer passing through the base of the sample between 1300 and 3000 minutes.
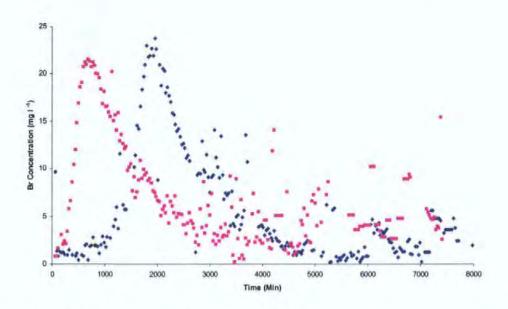
Figure 4.11 **Bromide breakthrough for Crediton Repacked (blue) and intact (pink).**

4.4.5.3 Derived Protocol

As demonstrated, the samples must be extracted intact and with minimum disturbance to the soil body, otherwise disruptions to the matrix will greatly affect the results of the experiments.

As shown in Figure 4.11 a large change in soil properties was observed. The symmetrical breakthrough curve found in the repacked sample took a much longer time to breakthrough the soil block. The breakthrough pattern is smoothly ramped either side of the crest, unlike the intact sample which rises rapidly and tails slowly, with a few peaks and spikes. This delay illustrates the break up of the naturally formed preferential flow channels that the repacking has removed.

From this experiment, it was shown that the bromide could be satisfactorily analysed, and a timescale for the experiments was established, with a 40 hour (2400 mins) experimental window for the tracer analysis, that would ensure recovery of most of the applied tracers. The analysis technique was also found to be practical for analysing large numbers of samples easily. A detailed discussion of analytical techniques can be found in Chapter 3.

The system developed for the analysis of leachates from soil blocks has given an improved experimental capability, allowing the monitoring of 3-dimensional tracer movement through soil blocks, over extended time periods.

The apparatus has given the capability to closely monitor and log rainfall rates, permeation rates through the block, with flexible sampling intervals.

4.5 Summary

In relation to the objective stated at the start of this Chapter (section 4.1), the apparatus constructed fulfilled all of the specifications required. The apparatus provided sample collection facilities, water saturation monitoring, rainfall application and precision distribution of leachates. This allowed close monitoring of leachates from the base of the block and when combined with the techniques described in Chapter 3, would give precise results of the tracer behaviour in soil blocks. The main points of progress are outlined in the bullet points below:

- Rainfall distribution was found to be dispensed evenly and unbiased using the apparatus designed by (Mathews et al, 1997).

- A suitable rainfall agent was found of consistent quality.

- Sample automation was found to be an efficient method of gathering a large volume of samples for later analysis at regular intervals.

- The TDR probes were found to be a reliable method for measuring the volumetric water content of the soils. This allowed the monitoring of sample saturation throughout the experimental period.

- A suitable timescale for the assessment of the migration of aqueous tracers through the soil block was found with a reliable timescale for delays due to differences in soil textures.

- It was shown that it was necessary to use intact soil samples. Looking at the experimental results shown in Figure 4.11, it was shown that disruption of the soil sample by repacking, alters the breakthrough characteristics of the soil.

5 Results of 2-Dimensional Tracer Analysis

5.1 Objectives

The experimental protocols and apparatus outlined in Chapter 4 were used to determine the following hypotheses:

1) Soil texture determines the rate at which aqueous and non-aqueous tracers penetrate a soil body. Conservative and non-conservative tracers were used to ascertain the extent of the retardation caused by

   i. Mineralogical properties (simply % clay content)

   ii. Physical structure (% sand, silt and clay)

2) NAPL present in a soil matrix retards the migration of aqueous species through that soil matrix.

In this study we were concerned with the effects of an LNAPL or more specifically dodecylbenzene on the migration of tracers through the soil block. We therefore analysed three different soil textures with a tracer study, firstly without oil in the tracer injection zone and secondly with oil introduced into the injection zone 8 hours before tracer injection.

5.2 Introduction

The experimental rationale was to use the Crediton series soil as a 'known' to calibrate the experimental protocol and assess the results of the analytical techniques. This was completed successfully and analysis of the extracted soil samples was continued. However one of the final soil samples proved problematic. The Clifton series soil when saturated became impermeable, with water collecting on the surface of the sample. This water collected and took several hours to reduce in level. This sample could therefore not be analysed using the protocol that was followed for the previous soil samples. Figure 5.1 is a photograph taken during this experiment showing the ponding on the surface of the Clifton soil.
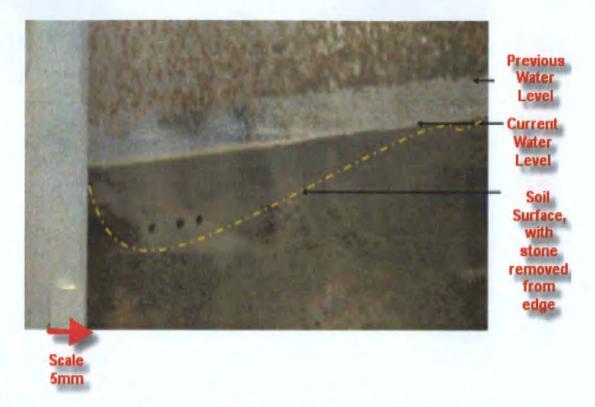
Figure 5.1   Excess surface water on Sollom sample, the length of the arrow is 5mm.

The results for the other soils will be displayed in turn with flow rates, aqueous tracers and oil distributions respectively.

5.3   Experimental Results

5.3.1 Saturation

Saturation levels were monitored closely throughout the experimental period using time domain reflectometry probes (TDR). Figure 5.2 to Figure 5.7 shows the change in volumetric water content during the experiments. The Conway soil pre oil injection was the longest to settle climbing until 20 hours with a short rise at 36 hours. This must have been due to inadequate pre-saturation, despite several days of simulated rainfall prior to the start of the experiment. During all the other experiments, volumetric water contents remained within ±5% of their initial value. The top probes at 10 cm depth were markedly more saturated than the remaining probes, approximately 49% saturation on average. The remaining probes at depths of 20, 30 and 40 cm remained at consistent saturation for the duration of the experiment.
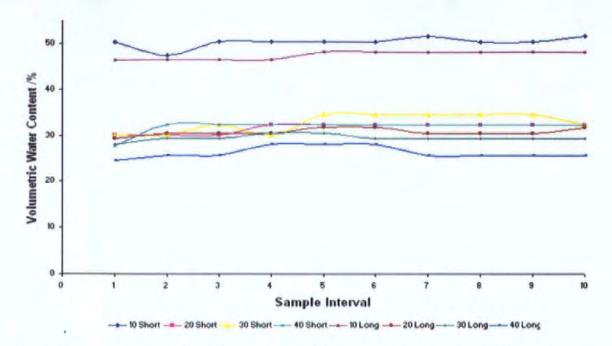
Figure 5.2 Crediton TDR probes reading pre-oil injection. The x axis units in this and the following figures are the sampling intervals, during the experimental duration of 40 hours.
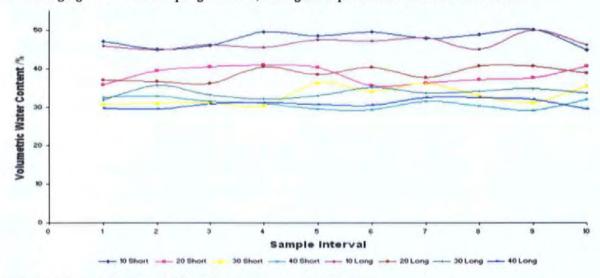
Figure 5.3 Crediton TDR probe readings post oil injection.
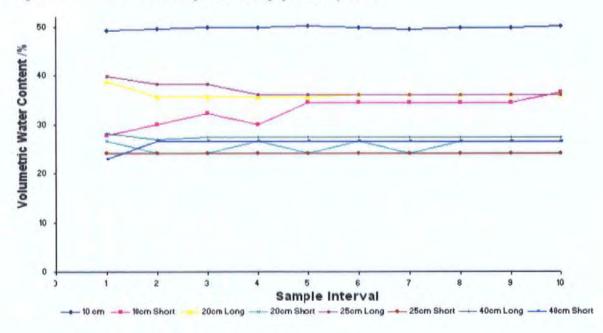
Figure 5.4 Sollom TDR probe readings pre oil injection.

105
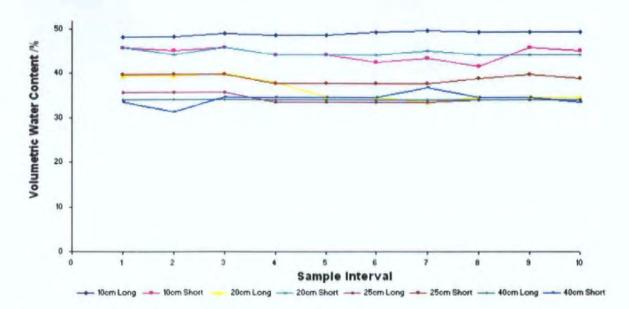
Figure 5.5   Sollom TDR probe readings post oil injection.
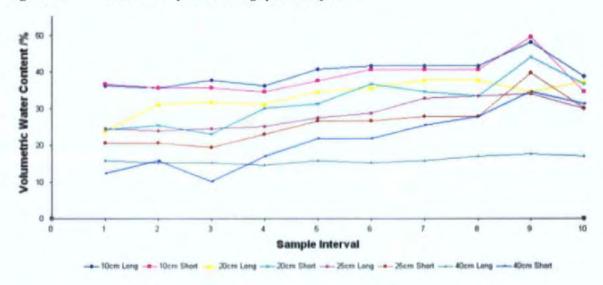
Figure 5.6   Conway TDR probe readings pre oil injection.
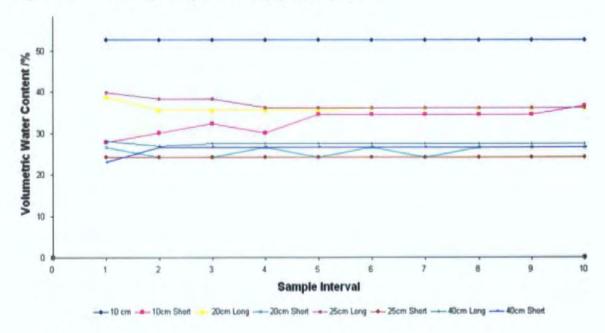
Figure 5.7   Conway TDR probe readings post oil injection.

The least saturated zone was near the base of each soil block, due to gravity drainage, and the most saturated zone was at 10 cm depth. Localised areas of ponding formed intermittently on the surface of the blocks, but then dissipated.

5.4 Eluate Flow Distributions

Eluate distributions were recorded by weighing each vial as it was removed from the sample tray, prior to analysis for aqueous phase tracers. Table 5.1 and Figure 5.8 show the percentage number of funnels flowing for the flow rates shown in the left-hand column. The values are for 1000 samples taken during the 40 hour time frame of the experiments. The flow rates were measured in mL over a 1 hour period.

mL/h	Crediton Pre Oil	Crediton Post Oil	Sollom Pre Oil	Sollom Post Oil	Conway Pre Oil	Conway Post Oil
0	72.61	74.21	49	37	90	83
< 0.1	0.6	1.5	0.0	0.0	0.1	0.8
0.11 - 0.3	0.9	2.2	0.1	0.2	0.1	1.1
0.31 - 0.5	1.7	1.6	1.1	2.0	0.1	1.2
0.51 - 0.75	1.8	1.8	4.6	3.0	0.1	0.9
0.76 - 1	1.6	1.1	3.6	3.0	0.3	0.6
1.1 - 1.25	2.1	1.8	3.7	3.6	1.4	0.8
1.26 - 2.5	4.3	4.0	8.8	16.1	3.5	2.2
2.6 - 5	4.3	6.0	11.3	15.4	2.2	3.1
5.1 - 10	10.1	5.8	17.5	19.5	2.8	6.3
10.1 - 20	0.0	0.0	0.0	0.0	0.0	0.0

Table 5.1   Percentages of flowing funnels for each experiment.

The Crediton soil had 72.6 % of funnels with zero flow increasing to 74.2 % of funnels not flowing after oil injection. For the Crediton Pre oil sample the largest flow range was in the 5.1 – 10 mL/h. After oil injection the flow rates recorded dropped to distributions in the 1.26-2.5 mL/h, 2.6-5 mL/h, and 5.1 – 10 mL/h ranges with values of 4.0, 6.0 and 5.8% respectively.

The Sollom soil sample had 49% of funnels with no flow in the 0 mL/h range pre oil injection whereas after oil injection 37% of funnels were in the 0 mL/h range. The Sollom pre oil injection flow rates were most commonly in the 5.1-10 mL/h range, as were the post oil injection flow rates.

The Conway soil had the least amount of funnels flowing with 90% of the funnels pre oil injection not flowing. After oil injection this dropped to 83%. The most frequently flowing funnels were found in the 1.26-2.5 mL/h whereas after oil injection the Conway soil showed the highest 6.3% of flow rates in the 5.1-10 mL/h.
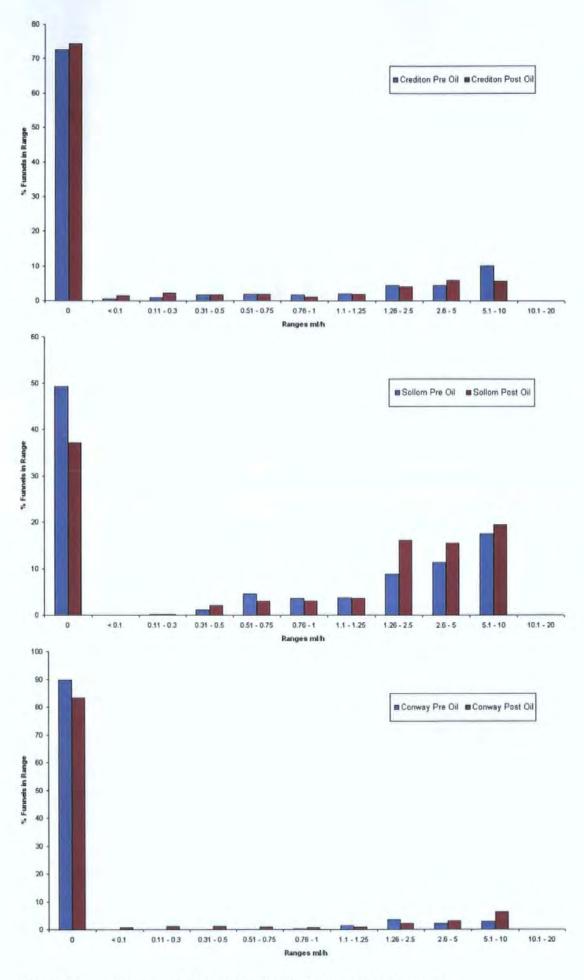
Figure 5.8   Percentage of funnels flowing during the entire experiment.
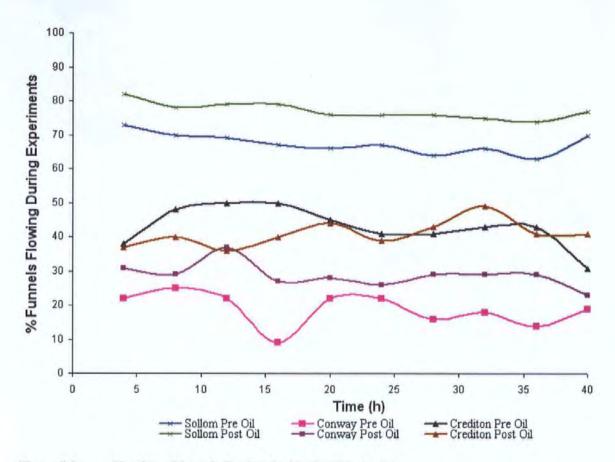
Figure 5.9   **Number of funnels flowing during the experiment**

The Conway soil displayed a very sparse quantity of funnels flowing with only 19% flowing pre oil and 29% flowing after oil injection.
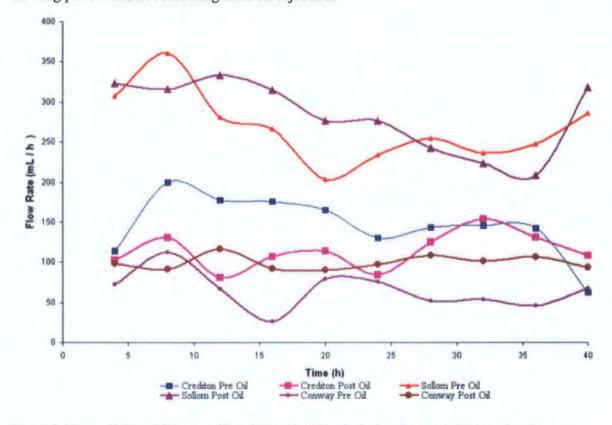
Figure 5.10   **Volume of eluate collected from the funnels during the lysimeter experiments.**

There was little visible ponding on the surface implying the water was being channelled through the soil body via a well established flow network.

Figure 5.11 to Figure 5.16 are contour maps of the volumetric flow rates of the samples collected at the lysimeter plate as described in Chapter 4. Blue represents no-flow zones. Red indicates the zones of highest flow.
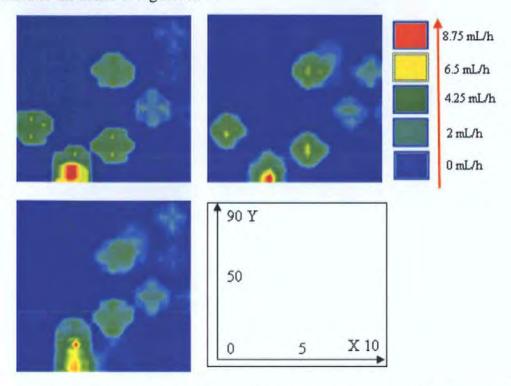
Figure 5.11 Eluate from the base of Conway block before oil injection. Top left 4 hours elapsed, top right 20 hours & bottom left 40 hours. All following diagrams use the same key for the *XY* coordinates funnel numbers.

Figure 5.11 includes a grid system with which to specify locations and areas on the lysimeter plate. So for example funnel 23 would be identified by *X3–Y*20. An area can be specified i.e. 23, 24 & 25 by the coordinate *X*(3-5)-*Y*20. Other zones can be identified for example funnels 23, 24, 25, 33, 34 & 35 by the coordinates X(3-5)-Y(20-30).
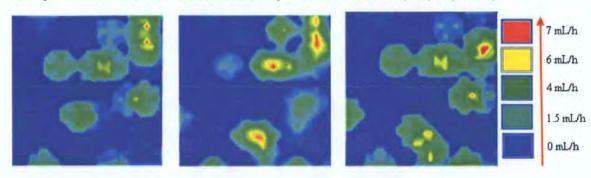
Figure 5.12 Eluate from the base of Conway block after oil injection. Left 4 hours elapsed, centre 20 hours & right 40 hours.

After oil injection into the Conway soil block, a distinct change in the preferential flow pattern is shown.
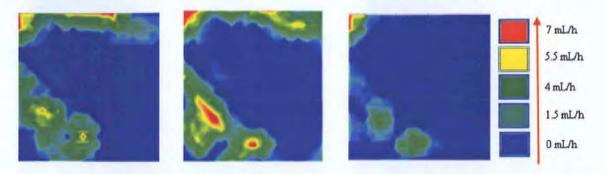
Figure 5.13 Eluate from the base of Crediton block before oil injection. Left 4 hours elapsed, centre 20 hours & right 40 hours.
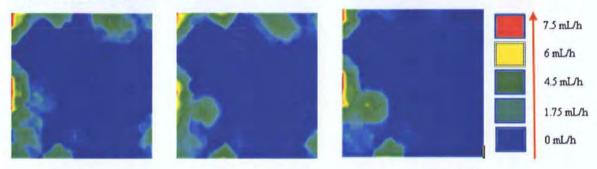
Figure 5.14 Eluate from the base of Crediton block after oil injection. Left 4 hours elapsed, centre 20 hours & right 40 hours.

The pre oil injection Crediton soil had a large flow zone through funnels $X1$-$Y(0$-$90)$ of the lysimeter collection plate. In the post oil injection sample funnels $X(2$-$4)$-$Y(20$-$30)$ had flows of between 4.5 and 6mL/h which where not shown previously in the pre oil sample.
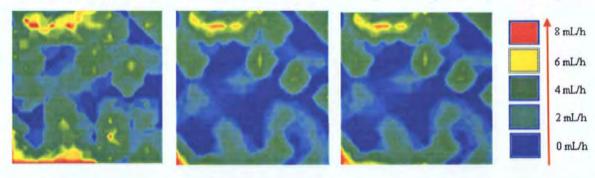
Figure 5.15 Eluate from the base of Sollom block before oil injection. Left 4 hours elapsed, centre 20 hours & right 40 hours.
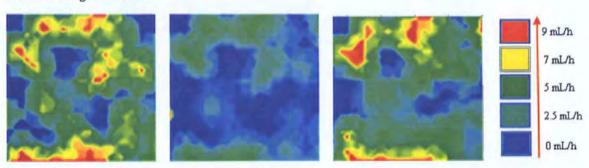
Figure 5.16 Eluate from the base of Sollom block after oil injection. Left 4 hours elapsed, centre 20 hours & right 40 hours.

The Sollom soil flow contours indicate a much more even distribution of flow from the soil block, with only 20–30% of funnels with no flow, during both experiments. Again the oil has very little effect on the flow zones in the soil.

Figure 5.17, Figure 5.18 and Figure 5.19 shows the distribution of funnel flow rates for the entire experimental period pre and post oil injection. The Crediton soil displayed very little difference in the flow patterns pre and post oil injection. A variation can be seen in the 7.5 mL/h region, but the other points differ very little.

The Sollom pre oil injection sample had a strong bi-modal distribution with 170 funnels flowing in the 1.25 mL/h and 150 funnels flowing in the 7.5 mL/h. The Sollom had 330 funnels flowing at 0 mL/h, with this figure reducing to 230 funnels after oil was introduced. Again the post oil sample was bi-modally distributed with 170 funnels flowing at 1.25 mL/h and 150 funnels flowing at the 7.75 mL/h.
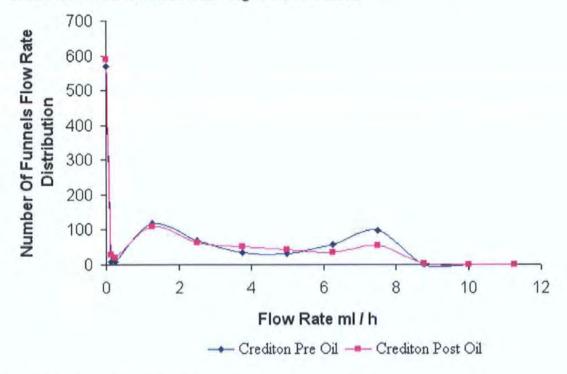
Figure 5.17 **Crediton funnel flow rates before and after oil injection.**
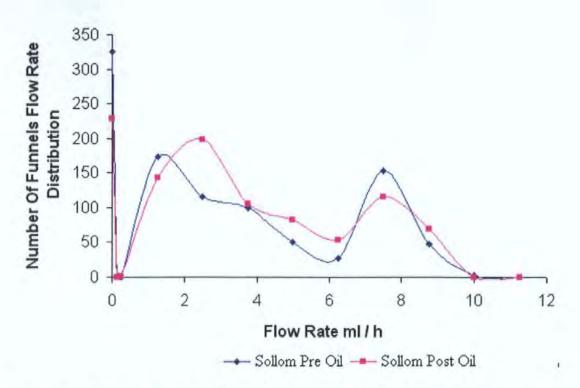
Figure 5.18   Sollom funnel flow rates before and after oil injection.

The Conway sample had by far the fewest number of samples collected 189 pre oil and 288 post oil injection. The flowing funnels were evenly distributed, with no major peaks in the distribution (excluding the funnels exhibiting no flow).
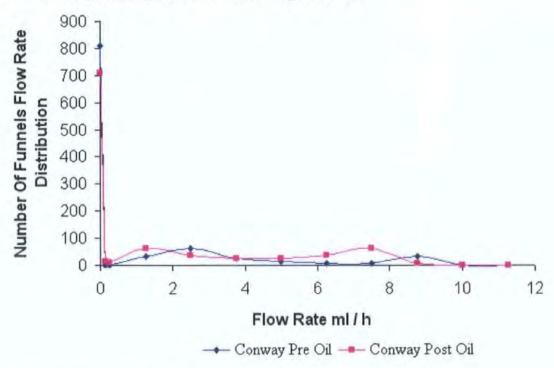
Figure 5.19   Conway funnel flow rates before and after oil injection.

5.4.1   Modified χ^2 analysis of flow rates.

We have seen that qualitative and semi-quantative trends can be deduced from the eluate flow rates. It is important to know whether the trends have any statistical significance. The great advantage of using a precision grid lysimeter is that a suitable statistical test can

be devised. The χ^2 statistic is usually employed to judge the significance of events, especially when those events relate to an expected Normal distribution. In this work we have modified the χ^2 test to study physical rather than Boolean data. The modified χ^2 statistic was calculated according to the relation:

$$\chi^2 = \sum \frac{(O_1 - O_2)^2}{E}$$

Equation 5.1

where O_1 and O_2 are the observed results and $E = \max(O_1, O_2)$. To normalise the data, the flow rates were expressed as a percentage of the total flow from the base of the block for each sample period. χ^2 was then calculated to test two features of the experiment:

- The consistency of the unperturbed flow rates
- The similarity or difference of the flow rates after introduction of oil

Normalised data for the modified χ^2 were derived from the data grids seen in Figure 5.11 to Figure 5.16.

Since the data was physical, albeit normalised, rather than Boolean, the usual probability calibration of the χ^2 statistic is invalid. Instead, the modified data set was skewed in several ways in order to understand how the χ^2 would alter with perturbations to the flow pattern. The modified χ^2 statistic was then calibrated against known statistical perturbation to the data. The procedure for perturbing the data was as follows:

i.   Typical data grids were selected.

ii.   The data was transposed along the diagonal values from top left to bottom right (green).

iii. A column of data was transferred in the X-direction (left to the right hand side) of the data grid, and the rest of the data transposed one column in the x-direction left, blue)

iv.   The data was also transposed in the Y-direction (yellow).

v.   The flow values from the original data set were put into entirely random positions (purple).

This produced banded distribution as shown on the chart in Figure 5.20 with the colours corresponding to the transformations described above. The horizontal axis represents each sample period comparison, so for x = 1, for example the comparison is made between samples collected at 4 hours to those made at 8 hours. The flow rates at the start of the experiment all take a few hours to settle, except for the Conway pre oil injection which shows unstable flow until the samples collected at hours 20 – 24 are compared when the flow drops down below the $\chi = 0.2$ value. The reason for this is unclear as the samples

114

were exposed to 48 hours of rainfall before commencing the experiments and as such should have been as stable as could reasonably be achieved. The Sollom pre oil sample also required 12 hours of further time before stability was achieved.

Figure 5.21, Figure 5.22 and Figure 5.23 illustrate the experimental consistencies and the differences between the samples after oil injection. The blue lines represent the flow patterns before oil is introduced into the soil block, the pink lines represent the flow comparison after oil is introduced into the soil block and the yellow line represents samples from the different experiment compared at the same time value. The χ^2 value can be seen to noticeably increase when attempting to compare sample grids from different experiments in the same time frame. This reflects a change in the way that the water is flowing through the soil.

Figure 5.21 shows that the flows within either the pre- and post- oil injection were stable ($\chi^2 \sim 0.1$ after initial equilibration). However, they are quite different between pre- and post-flow ($\chi^2 \sim 0.6$). So it can be seen that the addition of oil changed the flow channels, and set up a new stable system of flow, with approximately the same overall rate and distribution of funnels (Figure 5.8).

Figure 5.22 shows that the pre-oil-injected Sollom sample shows an erratic behaviour initially ($\chi^2 > 0.4$) but settles down after 8 hours to within the stabilised flow thresholds ($\chi^2 < 0.39$). The χ^2 for the pre- to post- oil comparison suggests that the oil has less of an effect on preferential flow than in the Crediton ($\chi^2 \sim 0.6$) or Conway samples ($\chi^2 \sim 1.2$) samples. The Sollom post oil experiment χ^2 falls always well within the stable flow zone.

In the Conway experiments, all the flows are less stable. The flows within the pre- and post-oil phases of the experiment have $\chi^2 \sim 0.2$ after initial equilibration and comparison of pre- and post-oil flows gives $\chi^2 \sim 1.2$, rising to a maximum of 1.6.
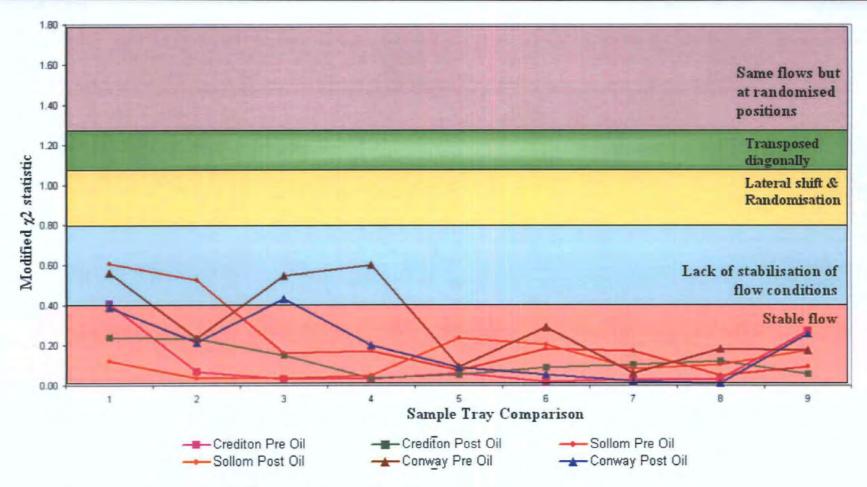
Figure 5.20 Calibrated banding assessing the χ^2 number and its associated flow properties.
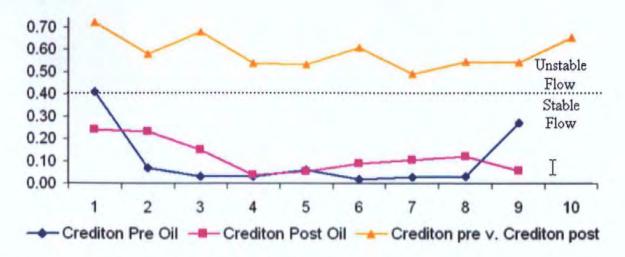
Figure 5.21   Crediton showing the relationships between sample trays during individual experiments and the sample trays Pre and Post Oil.
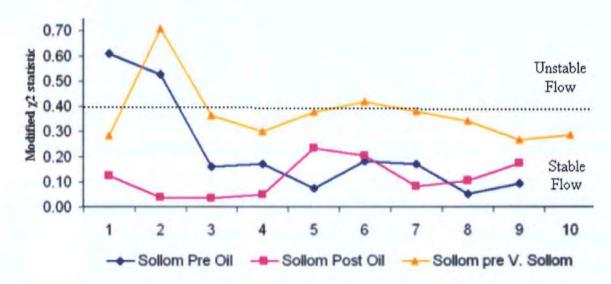
Figure 5.22   Sollom showing the relationships between sample trays during individual experiments and the sample trays Pre and Post Oil.
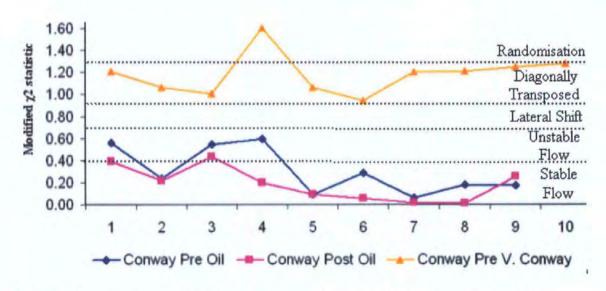
Figure 5.23   Conway showing the relationships between sample trays during individual experiments and the sample trays Pre and Post Oil.

5.5 Bromide Tracer Experiments

Bromide was used as a conservative tracer, i.e. a tracer that was not expected to interact with the soil matrix. Figure 5.24 is a plot of the bulk bromide breakthroughs for all experiments. The individual funnels behaviour for the experiments are shown in Appendix 1. The bulk breakthrough curves for Conway, Crediton and Sollom soils show quite different behaviours.

5.5.1 Bromide Distribution

The Crediton sample prior to oil injection has a double peak with an extended tail (i.e. one which decreases more slowly than predicted by a Convection-Dispersion equation). Such extended tails are encountered commonly, due to reservoir effects caused by the soil matrix. After oil injection there is a lag of approximately 4 hours from the V_{max} value between the two curves. A notable feature however is the fact that only 1500 mg L^{-1}/h at 20 hours was being eluted from the base of the soil block when compared to 3400 mg L^{-1}/h at 16 hours for the pre oil injected sample.
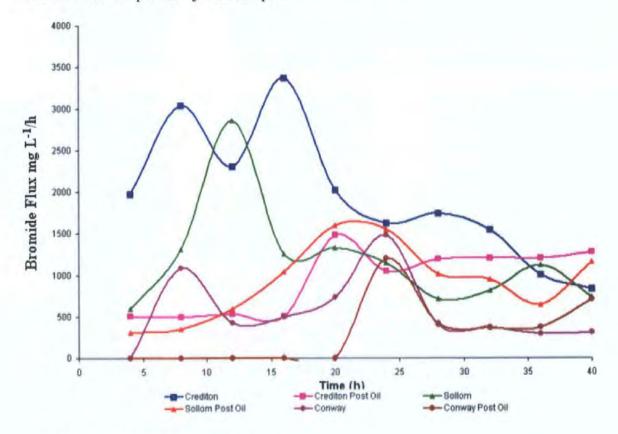
Figure 5.24   Bromide bulk breakthroughs.

The Sollom soil pre oil peaks at 12 hours with a flux of 2900 mg L^{-1}/h. Post oil injection the time taken to peak is 20 hours and at only 1600 mg L^{-1}/h. The Conway soil displayed an interesting pattern of behaviour. There was a rapid peak at 8 hours of around 1100 mg L^{-1}/h with a dip and then a gradual increase up to a maximum value of 1500 mg L^{-1}/h. The Conway soil after oil injection does not show the rapid initial peak but the breakthrough

period corresponds exactly with the 24 hour breakthrough shown in the pre oil sample. The flux of bromide is however slightly lower at 1150 mg L^{-1}/h. The tailing period is also unaffected by the oil and revealed an almost identical breakthrough tail with values matching at the 28, 32 and 36 hours.

We now look at the same results as three –dimensional distributions. Figure 5.25 represents a diagrammatic view of the soil block. Each of the arrows represents a line of sight (LOS), as if the viewer was looking at the soil block. This diagram is used to interpret the results as displayed in Figure 5.26 and Figure 5.42.
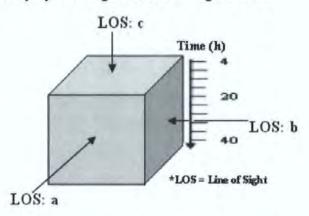
Figure 5.25   Diagrammatic representation of the soil block. Line of Sight represents the orientation of the viewer observing the soil block.

LOS: a would represent the viewer looking directly at the front of the lysimeter, LOS: b would be rotated 90^{0} to the right of the lysimeter and LOS: c would look vertically down, through the surface of the soil block. The time axis represents the results obtained from each sample tray. The higher up the diagram the earlier in the experiment the samples were produced, i.e. the topmost samples were analysed first. With LOS: c the time period disappears into the page, and so the diagram just shows the distribution across the X, Y grid. Isosurfaces plotted on Figure 5.26 show the zones of highest concentration for the bromide flux from the base of the soil block. LOS: a can be used as a 'rule of thumb' to visualize the lag time induced by the oil injection. LOS: c can be used to visualize the zones conducting the most bromide.

For the Conway soil it can be observed that the highest bromide concentrations were found within a few hours of commencing the experiment, as indicated by the red zone in the LOS: a. The oil injection has been seen to cause a severe lag in the time taken to breakthrough. It must also be noted that the bromide flux has been reduced by 75 % from a maximum of 600 mg L^{-1}/h to 150 mg L^{-1}/h.
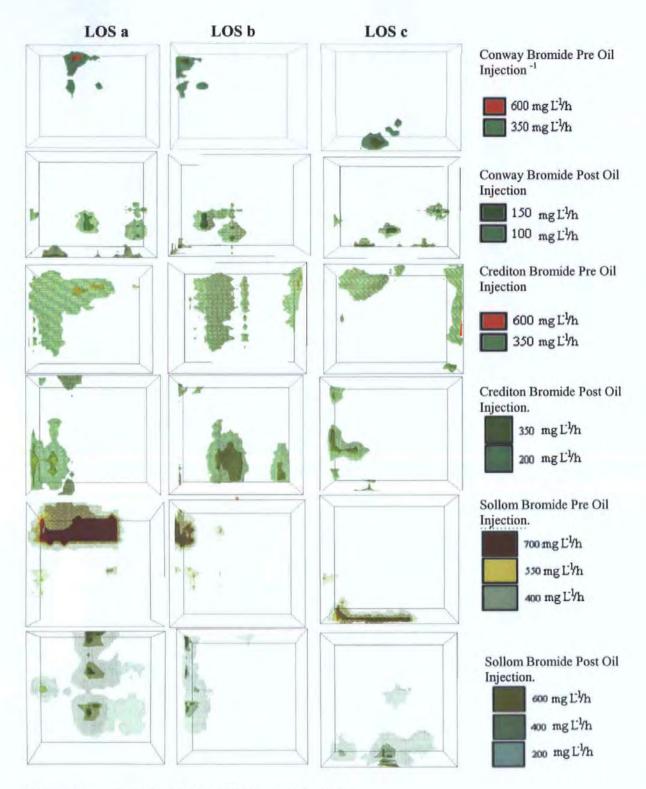
Figure 5.26   Bromide breakthrough for experiments.

For the Crediton soil it can be observed that pre-oil injection there is an almost immediate breakthrough. This takes place in the areas of funnels $(X(2-5)-Y(80-90))$. This zone of high concentration flow (350 mg L^{-1} / h) persists for around 30 hours giving a clear example of a preferential flow channel. Post-oil injection it can be observed that the breakthrough of bromide has slowed considerably. The main zone of preferential flow has shifted down to around the $Y(20-30)$ zone with even fewer channels conducting the higher concentrations of bromide.

The Sollom soil had a large zone of preferential flow in the $(X(1-6)-Y(0))$ zone. A large pulse of 700 mg L^{-1} / h passed through the sampling grid between 4-12 hours. This zone of preferential flow remains after oil injection, but the concentrations are again reduced. We can also observe an interesting pulsing feature as we move down a flow channel - every few hours a high concentration of bromide is eluted from the base of the soil block. This phenomenon can be observed in funnel $(X(5)-Y(0))$.

It is clear that for the Sollom soil, the oil again causes a lag effect in the bromide distribution. The flow channels have been changed ($\chi^2 \sim 0.4$, Figure 5.22), and the highest conducting channels are no longer able to conduct the eluate from the base of the soil block.

Figure 5.27, Figure 5.28 and Figure 5.29 are plots of funnels that when flowing also contained bromide in the leachate. There was more variation in the Crediton soil before oil injection than after oil injection. After oil injection 90% of funnels conducted bromide as compared to an 80% minimum pre oil injection. The oil injection appears to have caused bromide to be dispersed further and therefore leached from all flowing funnels.

For the Sollom soil 80% of the funnels were conducting bromide, slightly higher than the post oil Sollom that was just below 80%. There is no discernable effect that the oil injection affected the funnels that bromide was leached from, as there was variability in both data sets.
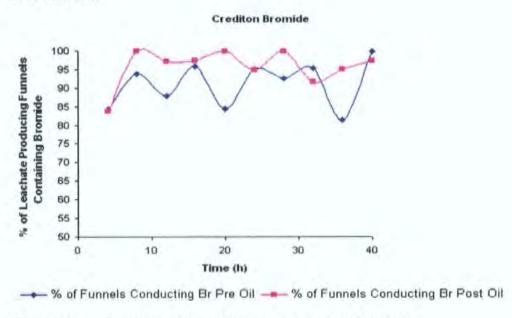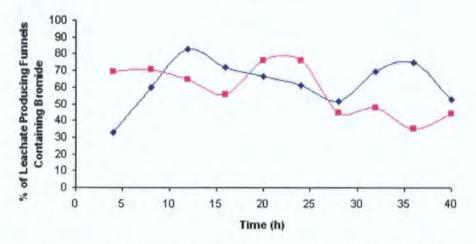
Figure 5.27   Percentage of funnels flowing that conducted Bromide.
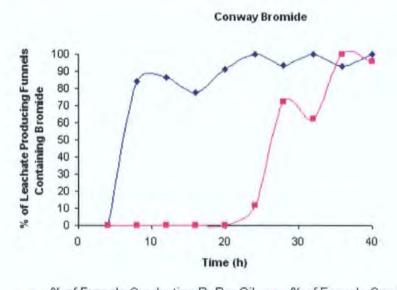
Sollom Bromide

— % of Funnels Conducting Br Pre Oil —■— % of Funnels Conducting Br Post Oil

Figure 5.28   **Percentage of funnels flowing that conducted Bromide.**

The Conway soil before oil injection had over 90% of funnels conducting bromide. After oil injection a lag period of 24 hours was noted before any bromide was conducted through these funnels. The oil has noticeably caused a severe lag in the amount of time taken for any bromide to be leached from the soil. 100% of funnels were conducting bromide at 36 hours.

Conway Bromide

— % of Funnels Conducting Br Pre Oil —■— % of Funnels Conducting Br Post Oil

Figure 5.29   **Percentage of funnels flowing that conducted Bromide.**

5.5.2 Statistical Analysis of Bromide Leachates

It was decided to analyse statistically the effect that the introduction of oil was having upon the flow of leachates through the soil block. In order to do this it was necessary to parameterise the breakthrough curves. However due to the high resolution of the experiments some of the breakthrough curves had a complex structure. However we believed it possible to overlook the small scale fluctuations and analyse the curves in such

a way that the general trends could be taken for each of the curves and parameterised. Three values were to be derived from each of the curves. The lag time, peak height and half width were calculated for each peak. These parameters could be used to then effectively describe each of the breakthrough curves.
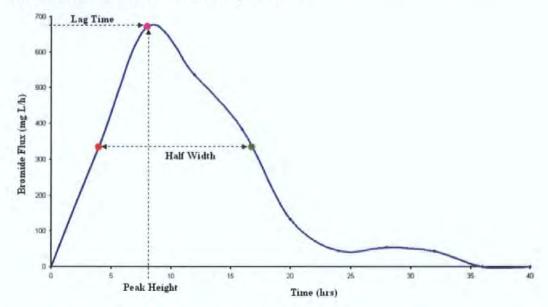
Figure 5.30   Parameterisation of a breakthrough curve.

As some breakthrough curves are complex (Figure 5.31), it was necessary to establish a cut-off point. The maximum breakthrough value was taken and then the first standard deviation from this value established a cut-off value of 19.154% on the complex curves. Peak areas above this value were then considered. To establish a half width of the peak the 50% cut-off point was utilised. This was taken for the first rise of the breakthrough curve which reached over 50% of the height of the maximum breakthrough. As the curve descended the last value that passed the 50% threshold was taken to be the terminating value for the half width.
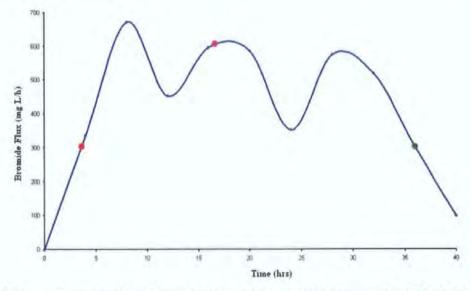
Figure 5.31   A complex breakthrough Curve, with corrected peak height and half width shown as dots.

Each of the parameters shown in table 5.2 would provide the following information:

1. Half Width – Breadth of the curves and persistence of the tracer in the water and also relating to the dispersal of the tracer
2. Peak Time – The speed at which the tracer reached the base of the soil block equivalent to the convection term in a convection dispersion eqation
3. Corrected Peak Height – the concentration of tracer eluted from the base of the soil block corrected for flow rates.

Bromide	Standard Deviation			Mean		
	Half Width	Peak Time	Mean Peak Height	Half Width	Peak Time	Mean Peak Height
Crediton Pre Oil	10.88	7.21	221.22	7.83	6.60	159.08
Crediton Post Oil	8.59	15.36	119.42	6.20	14.27	59.56
Sollom Pre Oil	9.91	10.47	238.92	8.71	13.16	158.70
Sollom Post Oil	7.71	13.72	151.34	7.79	18.35	102.86
Conway Pre Oil	6.52	9.22	197.79	3.27	5.17	70.81
Conway Post Oil	2.57	16.73	77.98	1.40	10.82	30.20

Table 5.2   Bromide statistical analysis summary

Figure 5.32 – Figure 5.34 are illustrations of the half widths of the peaks, or the time that the particular zone of the lysimeter was collecting bromide tracer. The x-axis and y-axis relate directly to the lysimeter grid, with the x1-y1 coordinate being the bottom left most funnel. The plots created by this method provide a very clear indication of the effect of the oil injection.
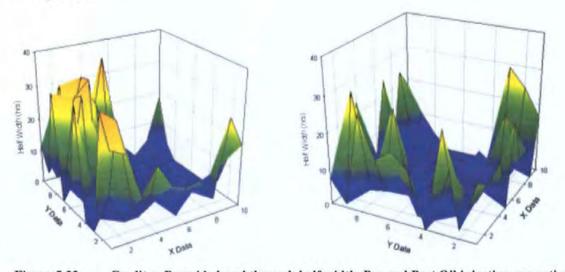
Figure 5.32   Crediton Bromide breakthrough half width. Pre and Post Oil injection respectively.

It can be seen from Figure 5.32 that there was a decrease in the amount of breakthrough curves expressing a half width of 30 hours. The region of occurrence of the breakthrough curves remained unaltered i.e. around the first row of the y-axis and along the first column of the x-axis. In all of the following figures the left hand plot is pre oil injection with the right hand plot being post oil injection.
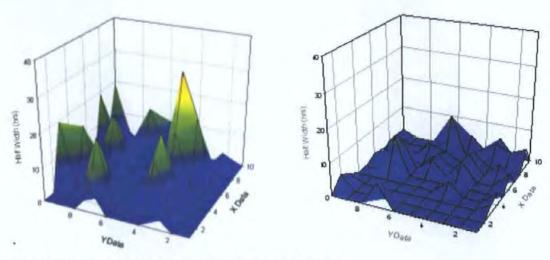
Figure 5.33   Conway bromide breakthrough half width.

The Conway soil displays a greater retardation in the peak times. The half widths can be seen to be greatest (above 15 hours) in several regions in the pre oil injection samples. Again similar zones are displaying the greatest half widths but the life span of these breakthroughs is on average around 5 hours, with two peaks reaching the 10 hour boundary.
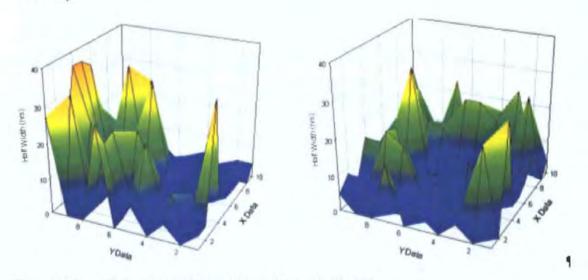
Figure 5.34   Sollom bromide breakthrough curve half width

The Sollom sample half widths were typically the longest reaching approximately 36 hours. Figure 5.34 it can be seen from the pre oil injection plot that very few of the funnels were not conducting bromide. The longest period of bromide leaching was found in the y>8 axis area. The typical value for data in this area is well over 20 hours. The post oil injection Sollom sample shows the greatest shift in the zone of the soil block that is leaching bromide. The x>8 values have now become the area of longest bromide breakthrough with breakthrough curves of up to 15 hours having been recorded.

After examining the half width of the curves, the peak time or time taken for the maximum volume of flow to occur were plotted. Figure 5.35 – Figure 5.38 show at which point in

time each funnel achieved its maximal flow value. It can be seen from these plots the progression of the bromide tracer through the soil block.
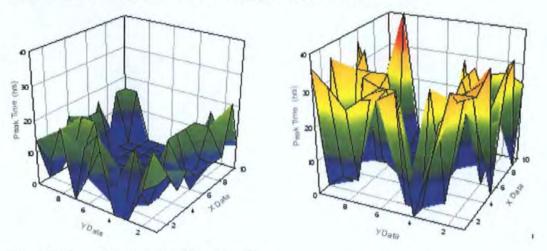
Figure 5.35   Crediton bromide peak time.

The oil has visibly increased the time taken for the bromide tracer to reach the base of the soil block. Pre oil injection it can be seen that the bromide tracer reached the edge of the soil block and passed through completely in <16 hours. However in the post oil injection sample it can be seen that the breakthrough time is typically extended to >25 hours.
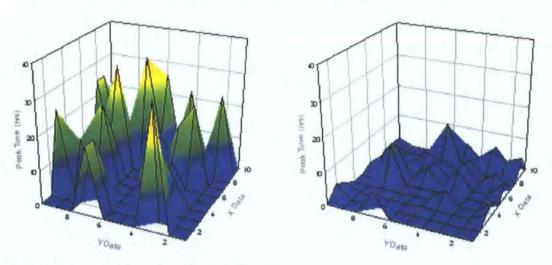
Figure 5.36   Conway bromide peak time.

In the Conway soil the breakthrough of the bromide has been altered in a unexpected manner. Previously the breakthrough time for the Conway soil was around 20 hours as is shown in the time that the peak in figure 5.24 reaches its maximum value of approx. 1200 mg L^{-1}/h. However oil injection reduces the time taken for the bromide to maximise its peak output. Reasons for this are discussed in the summary and further in Chapter 7.
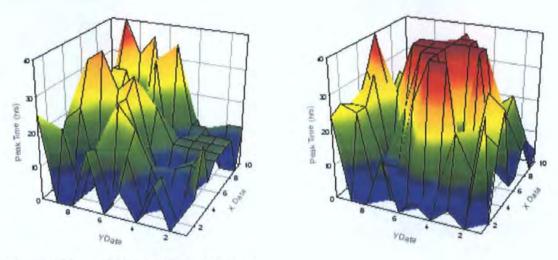
Figure 5.37   Sollom bromide peak time

The Sollom soil however shows behaviour in line with the Crediton soil. Peak time in the off centre y-axis 8 value is the longest suggesting that the bromide has migrated towards the edge of the soil block faster than through the centre of the soil block. Typically it was taking on average 13 hours (Table 5.1). This average increases up to 18 hours after oil injection. However it can be seen from Figure 5.37 that the centre funnels were not conducting bromide until late in the experiment. Figure 5.24 shows that although the total bromide breakthrough had peaked the breakthrough curve was still increasing as the experimental sampling was terminated.
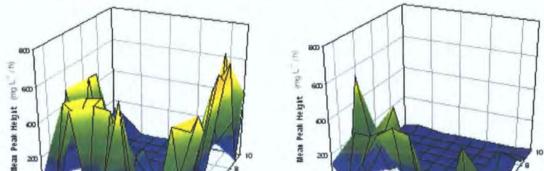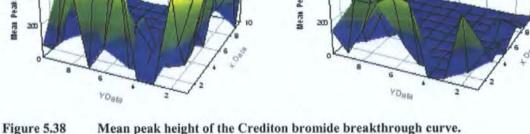
Figure 5.38 to 5.40 show the maximal peak value at breakthrough for each funnel.

Figure 5.38   Mean peak height of the Crediton bromide breakthrough curve.

From Figure 5.38 it can be seen that the maximal bromide peaks have reduced from >400 mg L^{-1}/h to (with one exception) to less then < 400 mg L^{-1}/h. There is also an almost a complete removal of the peaks in the y-axis 1 values.
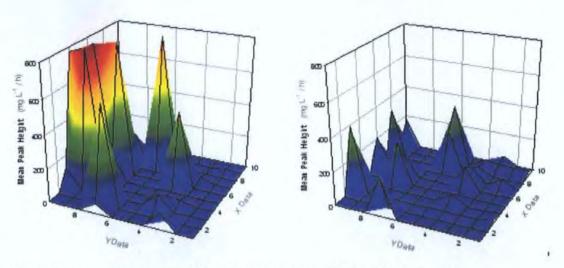
Figure 5.39   Mean peak height of the Conway bromide breakthrough curve.

The Conway peaks pre oil injection reach a maximum value of around 800 mg L^{-1}/h on the y-axis 10 values. Elsewhere there are several peaks clearly in view were the bromide has preferentially leached from certain areas from the base of the Conway soil. The oil injection has not altered the areas in the Conway soil from which the largest bromide peaks are to be observed but has however greatly reduced the amount of bromide that is leaching from the base of the soil block. In the pre injection samples the bromide curves were typically >= 400 mg L-1/h whereas all of the bromide peaks in the post oil sample can be seen to average around 200 mg L^{-1}/h.
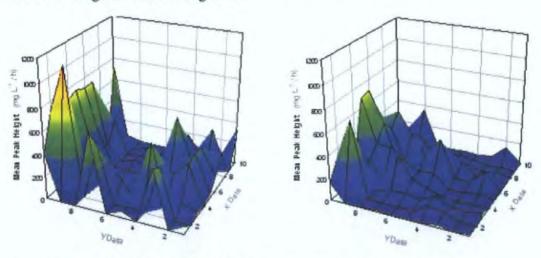
Figure 5.40   Mean peak height of the Sollom bromide breakthrough curve.

The Sollom soil peak values reduced in general, but the y-axis 10 area remained relatively unchanged. A major feature eliminated with the oil injection was the peak at x-axis 2 and y-axis 9, which reduced from 1100 mg L^{-1}/h to 600 mg L^{-1}/h.

5.6   Phosphate

The phosphate tracer behaved much more unpredictably than the bromide tracer.

5.6.1 Analysis of Phosphate Leachates

Figure 5.41 shows the bulk flux rate of the phosphate from the base of the soil block. Phosphate breakthrough for Sollom soil first starts after approximately 8 hours (200 mg L^{-1} / h), the Sollom soil, also shows a second major peak at 36 hours. The Sollom soil has a dual breakthrough. There is a smaller peak at 8 hours of 200 mg L^{-1}/h with a larger peak at 36 hours for 300 mg L^{-1}/h. The sample after oil injection does not demonstrate the sporadic nature of the pre-oil sample. The peak was found at 12 hours at a concentration of 100 mg L^{-1}.

The sandier Crediton series soil (200 mg L^{-1}/ h). The Crediton series soil then peaks at 20 hours when compared to 36 hours for the Sollom soil. The Crediton sample has a clear peak at 20 hours of 330 mg L^{-1}/h. The phosphate flux drops dramatically after 36 hours to 15 mg L^{-1}/h. After oil injection the breakthrough for the phosphate fluctuates at around 25 mg L^{-1}/h. There is no visible peaking in this sample, meaning the oil has slowed the phosphate distribution from the tracer injection site.

The Conway pre-oil injection samples were lost due to an instrumentation error. The post oil injection sample peaks at 36 hours at a concentration of 175 mg L^{-1}.
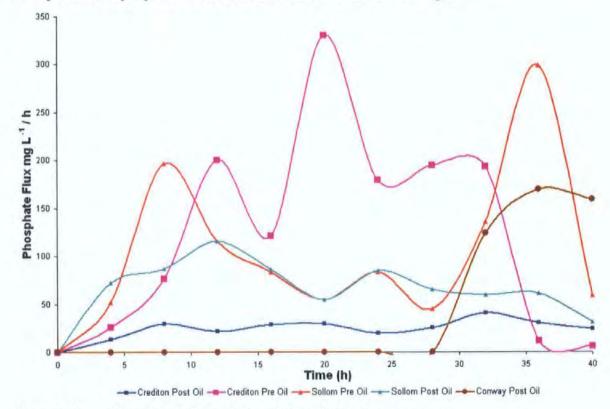
Figure 5.41   **Phosphate Bulk breakthrough For all lysimeter experiments.**

An alternative illustration of the breakthrough is shown in Figure 5.42, which is a 3-D plot of the flow through of phosphate from the lysimeter collection plate with lines of sight as

defined in Figure 5.25. Each layer represents a time period, in depth, with time increasing with depth (a and b) and with the top down view (c) time moves into the page.

In the Sollom sample, the initial speed of the first output could be due to mobile dissolved phosphate reaching a preferential flow zone quickly. The Crediton sample behaviour may be explained by the sandier soil having less interaction with the phosphate and therefore the phosphate passes through the body of the soil quickly, whilst being retained in the siltier Sollom soil matrix.

It can be observed from Figure 5.42 the Conway soil sample post oil injection, that the phosphate flow channels are distributed in discrete zones around the soil block. The Crediton and Sollom soil samples again reflect the behaviour that was observed in the bromide analysis, i.e. the reduction in Phosphate leaching from the sample accompanied by the alteration in preferential flow paths.
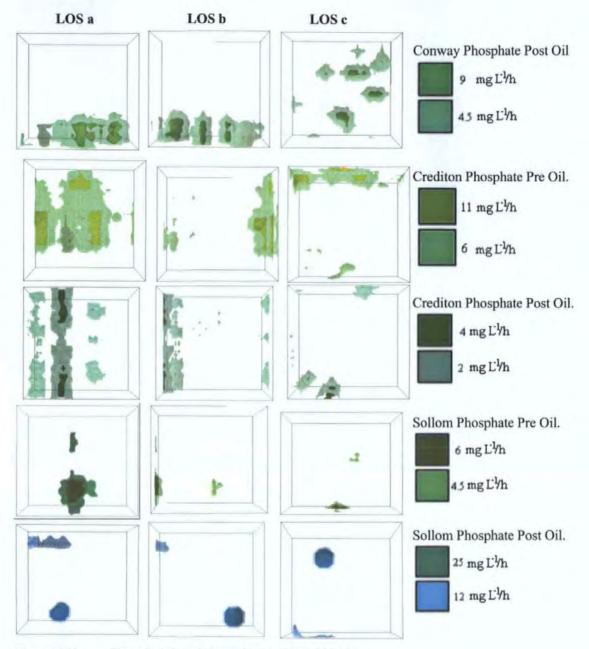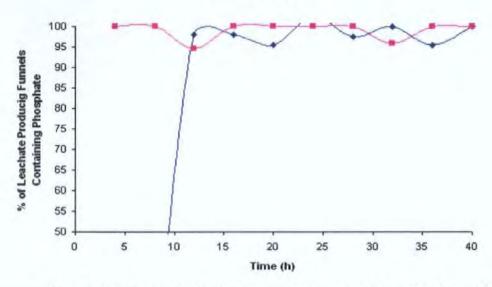
Figure 5.42   Phosphate breakthroughs for the soil blocks.

Figure 5.43, Figure 5.44 and Figure 5.45 show the percentage of funnels that were flowing and also containing phosphate. The phosphate was distributed throughout most of the funnels that were flowing. For each of the samples the distribution was usually above 95% except for the Sollom pre oil at 8 to 12 hours in which only 30% of the funnels conducted phosphate.

Crediton Phosphate

Figure 5.43   Percentage of funnels flowing that conducted Phosphate.

Sollom Phosphate
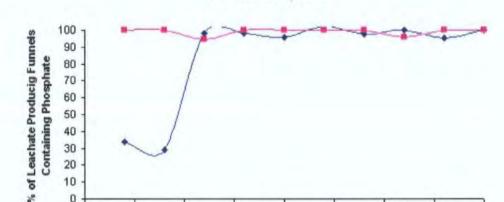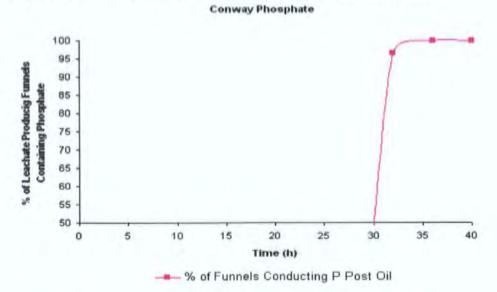
→ % of Funnels Conducting P Pre Oil —■— % of Funnels Conducting P Post Oil

Figure 5.44   Percentage of funnels flowing that conducted Phosphate.

Conway Phosphate

—■— % of Funnels Conducting P Post Oil

Figure 5.45   Percentage of funnels flowing that conducted Phosphate.

5.6.2 Statistical Analysis of Phosphate Leachates

Using the methods outlined in Section 5.5.2 the phosphate breakthrough curves were analysed. Table 5.3 is a summary of the statistical analysis. Due to the failure in the analysis of the Conway pre oil injection phosphate analysis no comparison can be made between the pre and post oil injection samples.

Phosphate	Standard Deviation			Mean		
	Half Width	Peak Time	Mean Peak Height	Half Width	Peak Time	Mean Peak Height
Crediton Pre Oil	11.46	10.65	3.89	9.91	9.75	2.56
Crediton Post Oil	9.11	13.59	1.28	6.19	12.37	0.65
Sollom Pre Oil	10.83	13.72	4.30	11.22	18.75	4.00
Sollom Post Oil	13.14	10.40	2.03	16.59	15.24	1.78
Conway After Oil	3.39	17.16	4.30	1.99	10.89	1.99

Table 5.3   Phosphate Statistical analysis Summary

Figure 5.46 – Figure 5.49 show the half widths for the phosphate curves leached from the base of the Crediton and Sollom soil blocks.
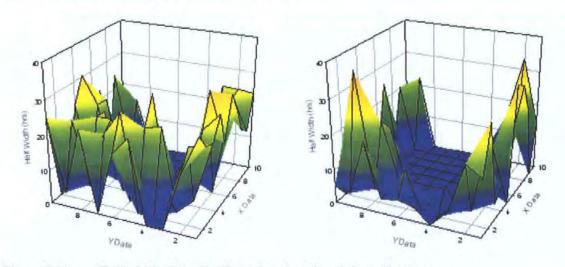
Figure 5.46   Half width of the Crediton phosphate breakthrough curves.

It can be seen from Figure 5.46 that the time period for the phosphate breakthrough after oil injection has reduced the amount of funnels conducting phosphate for any length of time. However the funnels that do conduct phosphate do so for longer >20 hours. There is a noticeable absence of any breakthrough curves in the centre of the Crediton soil block after oil injection. Pre oil injection there were more funnels conducting phosphate for around the 20 hour mark. The oil injection appears to have restricted the migration of the phosphate through the Crediton soil series.
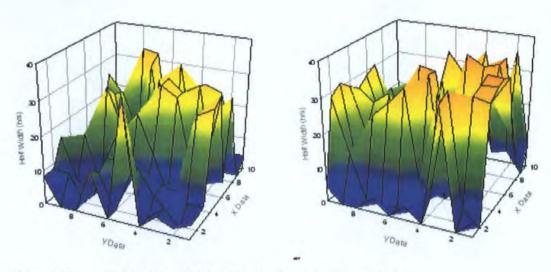
Figure 5.47   Half width of the Sollom phosphate breakthrough curves.

The Sollom half widths increase in length after oil injection rising from around 20 hours on average to over the 30 hour mark.

The peak times for the speed of the phosphate dispersal to the base of the soil block are shown in Figures 5.48 & 5.49. Again the left hand chart is previous to oil injection and the right hand column is post oil injection.
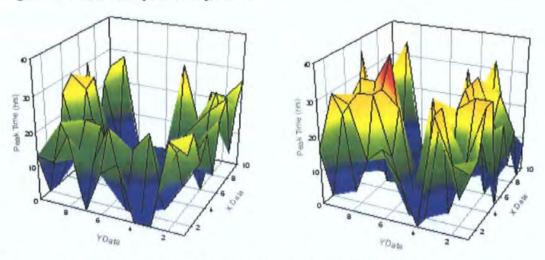
Figure 5.48   Peak time of the Crediton phosphate breakthrough curves.

The Crediton soil phosphate breakthrough curve was also delayed by the injection of oil. The breakthrough can be seen to be delayed by an increase of over 5 hours, and most of the peaks arrive at around 30 hours. This indicates an homogenisation of the distribution of phosphate through the soil block. It must still be noted that the peak time is only the arrival of the maximal point of the peak. The peak size is not indicated here.
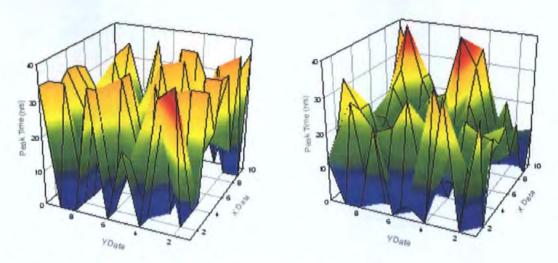
Figure 5.49   Peak time of the Sollom phosphate breakthrough curves.

The phosphate curve peak time has in fact decreased with the addition of oil. This may be an indication of the arrival of small amounts of phosphate at the base of the soil block. This will give the overall impression of a reduction in phosphate conducting channels, but this is in fact just a indication that very little phosphate may be penetrating the block.

Figure 5.50 & Figure 5.51 are the Mean Peak Heights for the phosphate breakthrough.
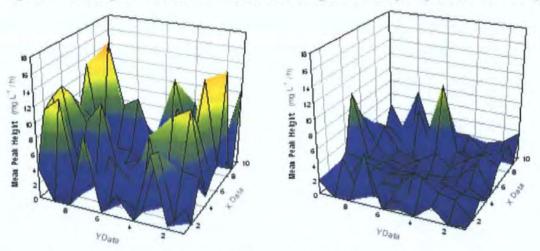
Figure 5.50   Mean Peak Height of the Crediton phosphate breakthrough curves.

Figure 5.50 it can be clearly seen that the phosphate has been reduced from an average of over 10 mg L^{-1}/h to an average of 4 mg L^{-1}/h, a clear indicator of the retarding effect the oil had upon the injection site.
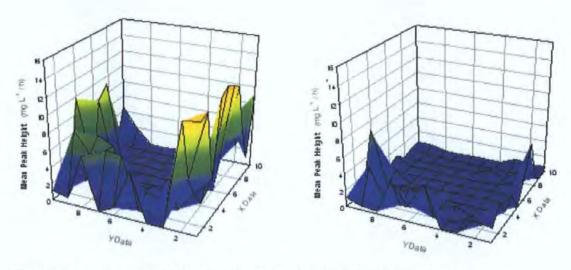
Figure 5.51   Mean Peak Height of the Sollom phosphate breakthrough curves.

The Sollom soil displayed a large decrease in the amount of phosphate eluting from the funnels.   The zones of breakthrough remained mostly unchanged.   However, the peaks reduced from well over 6 mg L^{-1}/h to a maximum value after oil injection of just over 6 mg L^{-1}/h in funnels 94 and 6.

5.7   Oil Distributions

5.7.1   Analysis of soil core samples

To determine the final location of oil in each soil block, each block was cored at the end of its experiments using a 2cm internal diameter steel gouge auger (Van Walt Limited, Haslemere, Surrey, U.K).   The oil migration study shows little relationship between the preferential flow pathways and the location of the oil.   Figure 5.52, 5.53 and 5.54 are 3-D distributions of the oil in soil as determined by the Scintillation counter described in section 3.2.2.   Larger diagrams are available in Appendix II.

The oil in the Conway soil has a pronounced difference in behaviour to that in the Crediton.   The 100 DPM oil plume migrates vertically for approximately 15cm before a pronounced lateral shift in the preferential flow path.   The oil migrated laterally for 15 cm before descending for another 5 cm.   Beneath the initial vertical plume of migration, a large lens of 85 DPM was observed at a depth of 30- 40 cm.

Profile View   Plan View
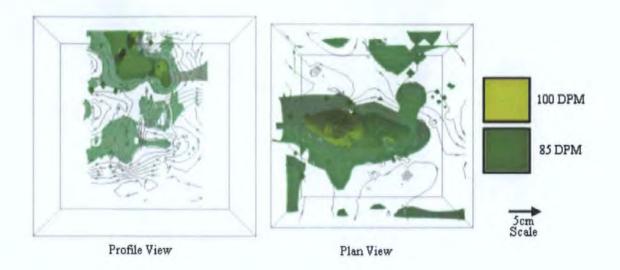
Figure 5.52   Conway oil Distribution

The oil formation in the Crediton soil measuring 100 DPM (disintegrations per minute) can be seen to have penetrated to a depth of approximately 20-25cm, with lobes of approximately 5 cm extending from the main lobe of the oil formation. Soil samples measuring 85 DPM can be seen to have penetrated throughout the soil structure. A large lobe of oil of 100 DPM has dispersed 20cm laterally from the oil application point. This may have migrated further, but the sampling regime did not allow for analysis of this section of the soil block. The 85 DPM areas can be seen to follow the distribution of the main formation, while more extensively penetrating throughout the structure. A definite area of preferential flow can be seen directly below the oil introduction point. Smaller isolated areas of 85 DPM oil where observed nearer the base of the soil block.

Profile View   Plan View
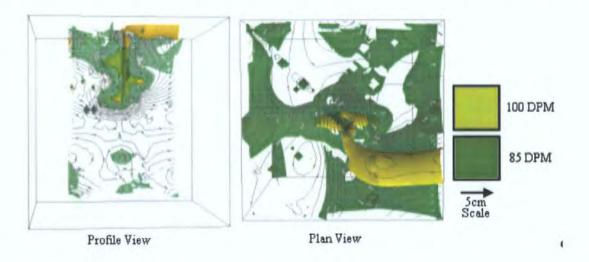
Figure 5.53   Crediton oil dispersal.

Profile View   Plan View

Figure 5.54   Sollom oil distribution.

Figure 5.55 illustrates the orientation of transects used to map the oil distribution in the subsequent figures. Figure 5.56, Figure 5.57 and Figure 5.58 show cross sections through horizontal vertical and planes of the highest concentration areas of oil distribution. As shown the highest penetration of oil can be seen in the Crediton series soil. There appears to be very little movement in the Sollom soil with a large lens appearing at the top surface of the block. The Conway soil allows a limited amount of penetration into the soil body, leaving a trace near the surface.
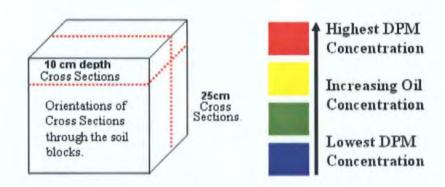
Figure 5.55   Cross sections from which figures Figure 5.56, Figure 5.57 and Figure 5.58 are composed. The scale on the right indicates the relative concentrations of oil in the soil block.
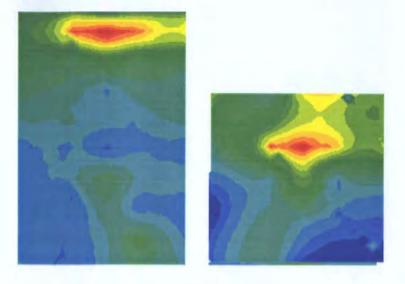
Figure 5.56 Sollom Oil Distribution. Highest Concentration 129 DPM. Left Vertical Section, Right horizontal section.
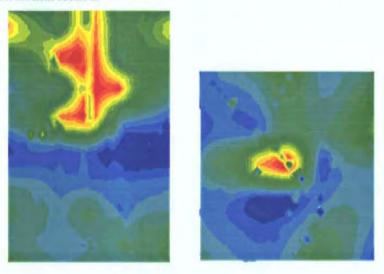
Figure 5.57 Crediton Soil oil distribution. Highest Concentration 110 DPM. Sections as above.
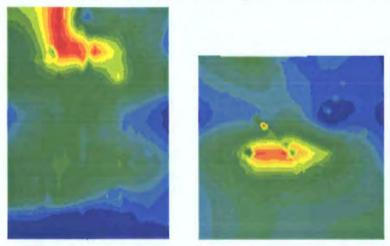
Figure 5.58 Conway Oil Distribution. Highest Concentration 135 DPM. Sections as above.

5.7.2 Statistical comparison of oil distributions

In order to compare the soil samples in a systematic fashion it was necessary to devise a method of establishing the dispersal of the oil through the soil blocks. Establishing a

statistic to compare the samples dispersal value would provide a good rule of thumb for evaluating the relative behaviour of the oil in the soil.

The method chosen for the assessment of dispersal was developed in order to compare adjacent nodes (points on the sampling grid). Each node was compared to its neighbour and if the DPM count was sufficient to trigger a binary return value then this value was added to the value of the counting node. First, all cells in the block were put on a binary scale, as giving either above or below a threshold, set as the geometric mean of the concentrations. Then each cell was compared to its neighbours, where neighbours were defined as shown in Figure 5.59. Then the number of similarities and differences counted up and then normalised across the entire soil block.

Figure 5.59 illustrates the method of assessing the adjacent cells. The central node assess the adjacent cells for their oil content in DPM. IF the oil content is above the chosen threshold then it assigns am increment to the central node.
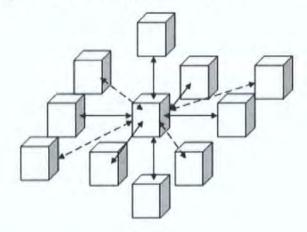
Figure 5.59   Nodes used in the calculation of oil distribution

Figure 5.60 shows the value of a cell which has no differences between itself and adjacent cells. This will return a zero difference value as the oil is equally dispersed throughout the area being measured. The diagonally adjacent nodes have been removed from this diagram for illustration purposes.
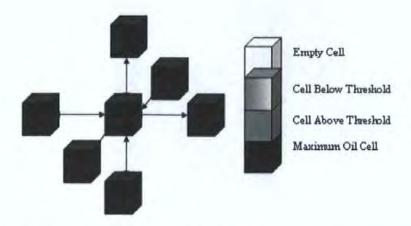
Figure 5.60   Nodes which will return a positive result in the oil distribution.

Figure 5.61 will return an absolute value of four as there are four cells adjacent to it, indicating a localised globule of oil.
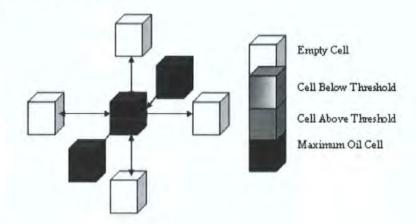
Figure 5.61   An example of a result returned for localised oil distributions

Table 5.4 shows the variance found in the soil samples using the above node analysis method.

	Variance Total
Conway	0.41
Crediton	0.40
Sollom	0.14

Table 5.4   Total variance established using the new method of node analysis

As shown in the Figure 5.57 -Figure 5.58 it can be seen that the lobate nature of the Crediton and Conway oil distribution has produced a higher figure than the Sollom oil. Figure 5.56 confirms that in the Sollom soil, the oil penetrated little into the soil surface and formed a lens near the surface.

5.8   Summary

We wished to investigate the effects of

1. Soil Texture

141

a. Its effects on the migration of LNAPL through soil structures

b. The effect of soil texture on aqueous species migration through the soil

2. The effect of oil injection on the transport of aqueous species through a soil.

These objectives were achieved with the successful analysis of the samples using the automated lysimeter (Chapter 4) and the automated analytical techniques studied in Chapter 3. This provided a large body of data which could be analysed in a stand alone method and also statistically analysed. In order to perform the statistical analyses of the flow rates, tracers and oil migration it was necessary to develop three new methods of analysis. This was due to the large and complex nature of the data generated during the studies for example each aqueous sample provided three data points flow rate, bromide and phosphate concentrations. This provided over 3000 data points for each experiments. The statistical methods developed where

1. a modified χ^2 analysis for flow rate comparison (Section 5.5.2)

2. A new method of breakthrough curve parameterisation (Section 5.6.2)

3. A new method for relationship analysis of oil distributions (Section 5.7.2)

Using these methods it was possible to summarise the findings as shown below.

5.8.1 Oil Migration

- Visual analysis of the Crediton and Conway soils reveals a lobate migration pattern whereas the Sollom soil forms a lens.

- Statistical analysis of these samples using the new method confirms this pattern assigning a variance of 0.40 to the Conway soil, 0.41 to the Crediton soil and the Sollom soil has a variance of 0.14, indicating the least dispersed oil.

5.8.2 Flow Rates

- The Sollom soil consistently provided the lowest percentage of non flowing funnels followed by Crediton and Conway respectively.

- The high clay and silt content of the Conway soil may have caused the observed alterations in the flow pattern of the Conway soil, as can be seen in Figure 5.11 and Figure 5.12. Most soils swell and shrink, and the shrinkage curve is one of their physical characteristics. A number of researchers have observed complex changes of pore space in shrink –swell soils with water content variation e.g., (Talsma,1985), (Assouline, Tavares, and Tessier, 1997), (Cousin, Levitz, and Bruand 1996).

- The oil alters the water content of a soil, and that if the soil structure is sensitive to water content, as in shrink swell soils, the addition of oil will cause significant

differences to the soils pore-heave hydrological characteristics, even though the saturation stays constant throughout the experiment.

- The χ^2 analysis revealed that within the unperturbed experiments there was generally stable flow. The Conway Pre oil injection was unstable for the first 20 hours but stabilised after this. All the flows fell well under the generated calibration grids for randomised flows which demonstrated that there was consistency within them.

5.8.3 Bromide Breakthrough

- Figure 5.24 shows the maximum bulk bromide breakthrough occurred for each of the samples with Sollom 2500 mg L^{-1}/h at12 hours, Crediton 3500 mg L^{-1}/h at 12 hours and Conway 1500 mg L^{-1}/h at 24 hours.

- The bromide migration was clearly impaired by the addition of oil to the injection site. The Conway soil reached its maximum breakthrough at 16 hours again with a breakthrough flux of 1300 mg L^{-1}/h, whilst the Sollom and Crediton fluxes were greatly reduced with breakthroughs at 20 hours and 1550 mg L^{-1}/h and 1450 L^{-1}/h respectively.

- The statistical analysis as shown in Figures 5.32 to 5.40 reveal several important factors. The Crediton and Sollom soil samples peak times (i.e. the time taken for bromide to reach its maximum breakthrough value) are greatly increased by the addition of oil. The Conway sample peak time is greatly reduced by the addition of oil, which may be due to lower concentrations of bromide reaching the base of the soil block and causing the breakthrough curve to peak quickly but with much less bromide content.

- The breakthrough curve concentrations were reduced by oil for all the soils.

5.8.4 Phosphate Breakthrough

- From Figure 5.41 shows the maximum bulk phosphate breakthrough occurred for each of the samples with Sollom 290 mg L^{-1}/h at 36 hours, Crediton 320 mg L^{-1}/h at 20 hours and Conway (post oil only) 165 mg L^{-1}/h at 24 hours.

- Oil addition impairs the phosphate progress also with Solloms breakthrough 110 mg L^{-1}/h at 12 hours and Crediton's 40 mg L^{-1}/h at 32 hours.

- The ratio of funnels flowing to those conducting phosphate is high in all experiments and not perceptibly affected by the oil injection. This may be an artefact of the limits of detection of the analytical method that can detect the phosphate at the μg L^{-1} as opposed to the mg L^{-1}. However the presence of the

phosphate indicates a migration from the point source, as there was no detectable phosphate prior to the experiment.

- The statistical analysis for phosphate (Figure 5.46 - Figure 5.51) reveals similar trends to those seen in the bromide analysis. The peak heights are reduced in both experiments with the most dramatic decrease in the phosphate retarding being found in the Crediton post oil sample which only has 2 peaks over 6 mg L^{-1}/h whereas over 90% of the peaks in the pre oil sample were above this range.

Appendix I contains the high resolution plots of all the data collected during the analysis of the soil blocks. Appendix II contains full page figures of Figures 5.52 – 5.54. Further discussions on the causes of oil as a migration inhibitor are explored in more detail in Chapter 7.

6 Modelling of soil data (Johnson, Roy, *et al.*, 2003)

6.1 Objectives

The use of a pore-scale model can be used to obtain more information from soil water retention curves than is currently obtained. Our first objective was to use our own pore scale, Pore-Cor, to simulate water retention curves generated by a pedo transfer function. This lead onto the second objective which was to interpret the results and to reveal the additional information obtainable from soil water retention curves. The third objective was to attempt to extend the model and apply it to real soil samples. The soil water retention curve (SWRC) would then be used to assess the models performance on real samples.

In order to meet the above requirements it was necessary to extend the capabilities of the Pore-Cor network model. Described in this Chapter is the development of an annealed simplex method for the analysis of soil water retention curves. The new method was subjected to a sensitivity analysis. To demonstrate its application, an environmental impact assessment carried out by Bodurtha (Bodurtha *et al.*, 2003) is also briefly described.

The improved algorithm allowed the modelling of:

- Hydraulic Conductivity (K)
- Transmissivity to pollutants
- Structure variation with texture

6.2 Data Sets

6.2.1 National Soils Resources Institute Pedo-Transfer Function

This study used a pedo-transfer function (PTF) as discussed in Chapter 1 (Equation 1.27 & Equation 1.28) developed at the National Soils Resources Institute (NSRI), UK (Mayr and Jarvis 1999). The PTF is based on a least squares regression analysis of a very large data set of English and Welsh soils. In principle the PTF spans soil water contents at an infinite range of pressures. However it is impossible to simulate a void network which covers an infinite range of void sizes, and hence predicts an infinite range of water tension pressures. The lower end of the size range was therefore truncated at a diameter equal to the wilting point diameter for plants of 0.2 μm. Voids smaller than this were assumed non-conducting, an approximation that introduced small inaccuracies (Bryant, 1993). Also imposed was an upper limit of 2500 μm, which is around 5 times larger than the typical air-entry diameter for gravity drainage.

Since we model the void network only over the range 0.2 to 2500 μm, the modelled porosity must include only those voids within this size range. Due to the shielding or shadowing of the large voids within the matrix, this adjustment cannot be made exactly.

Lacking any other information, an assumption was made that the correlation between pore and neighbouring throat sizes was like that in sandstone, i.e. each pore was the same size as the diameter of the largest throat entering it (Matthews, 1993). In other models the size correlation between throats emanating from the same site has been found to be important (Rajaram, 1997).

6.3 Soil Modelling under Pore-Cor

In the previous work, fitting was done by a 'grid' method – i.e. two parameters were chosen by the user by trial and error, and then a grid of combinations of two other parameters was tested, and the best combination found. Figure 6.1 illustrates an obvious problem with the grid method, which is that its precision is limited by the spacing of the grid.
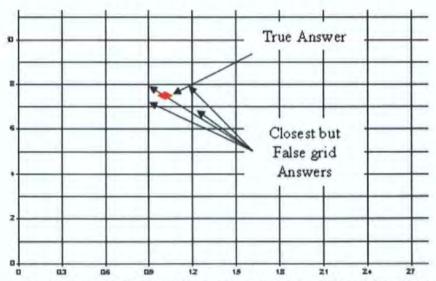
Figure 6.1   The grid method of parameter space exploration. The red diamond indicating the correct answer, which is unobtainable by the use of the grid method.

Here, we describe the use of an annealed simplex for the fitting. The far greater speed and effectiveness of the new procedure allowed us to perform a more robust sensitivity analysis and to model a wide range of soils across the whole soil texture diagram.

6.3.1 The Simplex Method

Finding the best-fit values of four geometric modelling parameters is analogous to finding the global minima of a four–dimensional surface. Each simulated curve can be thought of as being a function of four variables say, s, u, v, w, and the 'distance' between simulated and experimental curves as $f(s, u, v, w)$ for some function f. Suppose also that there exists a

global minimum value of the function, δ. We wish to find the quadruple ($s=s_p$, $u=u_p$, $v=v_p$, $w=w_p$) such that $f(s_p, u_p, v_p, w_p) = δ$. In the case where the function f is not differentiable we need some other way of finding the minimum point. The simplex method (Nelder and Mead, 1965) provides a suitably robust method for doing this.

To find the minimum δ, the simplex can undergo four different transformations, Figure 6.2, namely reflections, extensions, contractions and shrinks. Within the Pore-Cor model, the simplex works in four parametric dimensions, namely throat skew, pore skew, and connectivity as described above, and correlation as described below. The simplex is also constrained by an additional three Boolean dimensions defined by the criteria that

(i) the structure must be adjustable to the exact experimental porosity, without overlapping adjacent pores,

(ii) the structure must be such that at infinite applied pressure on the fluid, all voids would be percolated – i.e. there is no unconnected region of the void network, and

(iii) the structure must be geometrically realisable, a criterion that is not met when, for example, the correlation required cannot be achieved for a structure of the required porosity.
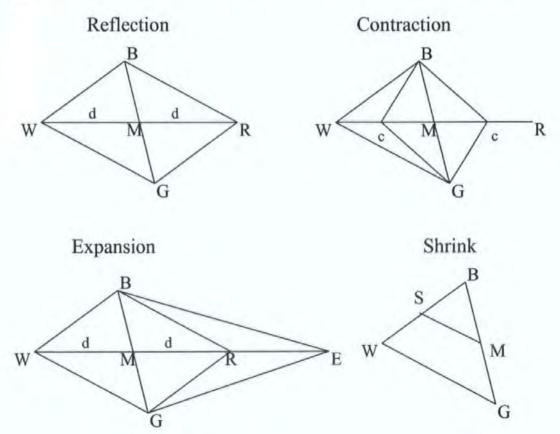
Figure 6.2 The Available Simplex Manoeuvres. Where B, G and W are the starting points. M is the Median, R is the point of Reflection, E point of Expansion and S is the point of shrinkage. d and c represent distance and contraction points.

Depending on where the simplex starts, it runs the risk of converging to a non-global minimum of the distance function $f(s_p, u_p, v_p, w_p)$. The existence of non-global minima is particularly likely when experimental water retentions curves are used, because these contain experimental scatter and because of 'granulation' of the Pore-Cor parameter space, as explained below.

In an effort to circumvent this problem, (Press and Teukolsky, 1991) describe how the simplex method can be combined with a so-called annealing schedule. They explain how conventional minimization algorithms are analogous to rapid cooling; they go downhill as far as they can go and this leads to a local, but not necessarily global minimum. Therefore the simplex is given an energy determined by a Boltzmann probability distribution,

$$\text{Prob}(E) = \exp\left(-\frac{E}{kT} \right)$$

where k is the Boltzmann constant. It reflects the fact that a system in thermal equilibrium at temperature T has its energy probabilistically distributed among all different energy states E. Even at low temperatures, there exists the possibility, albeit very small, of the system's being in a high energy state. As a result, there is a corresponding chance for the system to escape out of a local energy minimum in favour of finding a better (lower) minimum. Thus the system sometimes goes uphill (in terms of energy) as well as downhill, but, crucially, the lower the temperature, the less likely is any major uphill movement.

For the simplex to move around the parameter space effectively, parameters must be defined such that measurements or trials would have an approximately equal distribution throughout the total range of the parameter. This is a necessary operation in chemometrics as well, and in that field is known as 'variance stabilization'. We therefore have to transform two of the variables into what we refer to as 'stabilized' variables. Additionally, the parameter space must not be granular – i.e. quantized in one or more of its dimensions. The stabilized throat-skew is defined according to the following formula, where q = throat-skew:

$$\text{Stabilized throat-skew} = \begin{cases} \dfrac{q}{1-q} : q < 0 \\[2ex] q \ : 0 \leq q \leq 2 \\[2ex] \dfrac{3q-4}{q-1} : q > 2 \ . \end{cases}$$

<div align="right">**Equation 6.2**</div>

The stabilized pore skew is simply $\log_{10} \sigma$, reflecting the fact that void sizes within soils tend to be logarithmically distributed. Table 6.1 shows examples of these stabilized variables. Another geometric parameter is 'correlation level', C, which is a measure of the degree of structure of the soil – it is related to a size auto-correlation function, in this case over distances of tenths of a millimetre. It is normalized so that zero corresponds to a completely random soil, and 1 to a fully structured soil, for example one comprising vertical bands or laminae. The previous definition of this parameter (Matthews *et al.*, 1995a), led to quantization in five steps, $(0, 0.2 , 0.4, \dots,1)$, with intermediate values of C undefined. For correct operation of the simplex, the laminae are no longer completely flat, but are slightly curled on spherical loci.

Connectivity	Throat skew	Stabilized throat skew	Pore skew	Stabilized pore skew	Correlation	Distance
5.500	-2.000	-0.667	1500	3.176	0.200	14.867
3.800	0.573	0.573	12000	4.079	0.404	10.643
4.480	1.437	1.437	8075	3.907	0.614	5.117
5.000	2.000	2.000	5000	3.699	0.400	3.625
4.620	2.009	2.009	5180	3.714	0.748	1.354
4.350	0.884	0.884	7107	3.852	0.447	10.479
4.343	2.076	2.076	9372	3.972	0.431	2.098
4.489	2.094	2.086	8750	3.942	0.679	1.610
4.814	2.033	2.032	5924	3.773	0.768	1.427
4.620	2.009	2.009	5180	3.714	0.748	1.354
4.376	1.970	1.970	9569	3.981	0.799	1.201
4.390	1.902	1.902	8979	3.953	0.794	1.136
3.290	1.702	1.702	8979	3.953	0.794	1.038
3.310	1.652	1.652	8979	3.953	0.794	0.912
3.257	1.670	1.670	9284	3.968	0.788	0.900

Table 6.1 Some of the many hundreds of the movements of the simplex from its starting points shown in the top five rows of the table, and combinations of parameters which give ever better fits. The optimum fitting combination is displayed in the final line of the table. This fit is of the invented 2-D surface Figure 6.3. All parameters are dimensionless.

The effect of this is that the structures corresponding to the previously quantized values of C listed above are the same, but that intermediate values of C (such as 0.29) are now also defined. Thus there is no longer any quantization of this parameter that would confuse the

movement of the simplex. Figure 6.3 is a side representation of the parameter space. A simple 2-D simplex path is shown in Figure 6.4. The simplex can be seen to converge upon the lowest point in the parameter surface. The simplex movements are represented by the red line which clearly shows rapid convergence onto the true minimum.
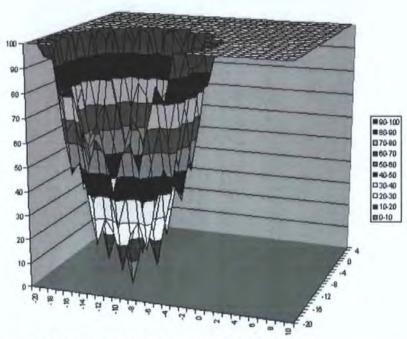
Figure 6.3   The 2-D test parameter space explored by the simplex.
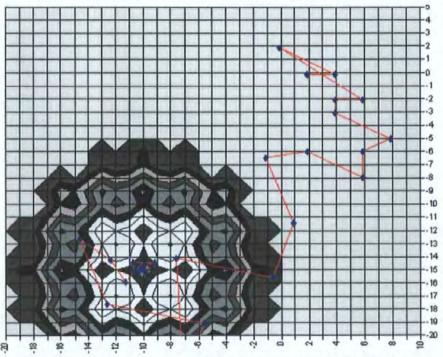
Figure 6.4   Convergence of a 2-D simplex upon a minimum point in parameter space.

The distance function f can best be understood by reference to Figure 6.5, which shows a typical fit of a simulated to an experimental water retention curve, in this case for a soil comprising 34% sand, 33% silt and 33% clay. Suppose that the vertical axis is normalized to cover a range 0 to 100% of total water content, i.e. so that the total modelled porosity of 19.3% becomes 100%. The horizontal axis is normalized by taking the logarithm to base

10 of the tension (or of the equivalent throat diameter calculated from the Laplace equation). Then if the experimental and simulated curves are plotted on such a graph, the distance f is the average distance between each experimental point and the nearest simulated point. Figure 6.5 shows the fit achieved using the Simplex method.
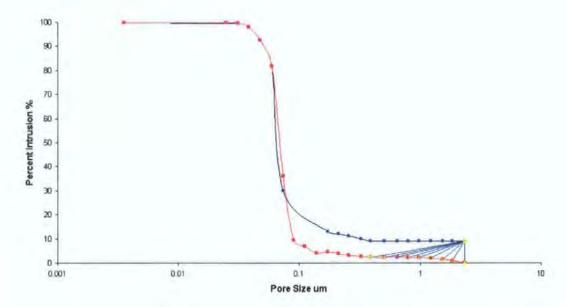
Figure 6.5 The fitting method developed to assess the quality of the fitted simplex algorithm results. Simulated data (red) Experimental data (blue). The distance used is the shortest, in this case the vertical distance between the points marked in yellow.

As the distance is normalised and dimensionless, it can be compared from sample to sample. Subjectively we class $f = 1$ as a good fit, and so $f = 0.900$ is a very good fit. Table 6.1 lists some of the many hundreds of the movements of the simplex, as it moves from its starting points, shown in the top five rows of the table, to combinations of parameters which give ever better fits, as measured by the distance f. As the simplex moves, the distance reduces ultimately to the value of 0.900 shown in the bottom row of Table 6.1. The control panel for the simplex is shown in Figure 6.6.
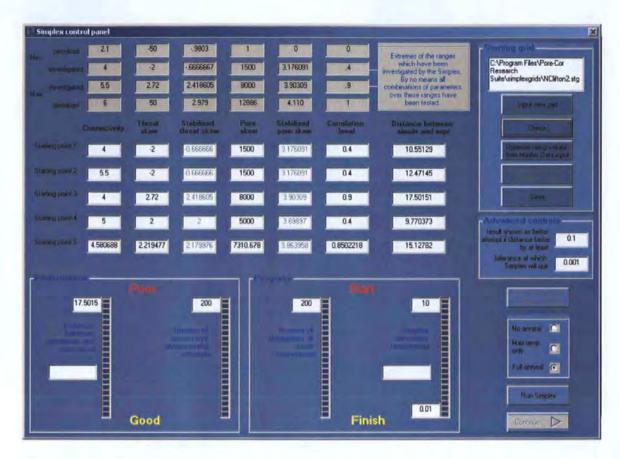
Figure 6.6   The simplex parameter control screen

6.3.1.1 Effectiveness of the Simplex method

Experimental water retention curves typically comprise only four or five experimental points. It is therefore not surprising that smoothing equations, such as those of van Genucthen, Kosugi, and Brooks and Corey, which typically contain four fitting parameters, often seem to fit the experimental points perfectly, since the number of statistical degrees of freedom is typically one or zero. Often, as in this work, individual water retention curves of a wide range of soils are not available individually, and so there is a fit of a water retention smoothing equation to a pedo-transfer function, which is itself based on a smoothing equation. Again, unsurprisingly, the fit seems remarkably good. So in the current work, the use of the simplex method has not improved on the closeness of fit of the traditional approaches. It has merely succeeded in bringing the quality of fit from one which was significantly worse than the traditional approach (as shown in Figure 6 of (Peat *et al.*, 2000) to a fit that is equally good. The improvement therefore lies not in the quality of fit, but in the speed of fitting, which allows more simulations and therefore allows a sensitivity analysis to be carried out (a feature often lacking from traditional approaches).

6.4 Results and Discussion

There are an infinite number of void structures that generate the same water retention curve. Arbitrarily constraining the geometry of the void structures reduces the number of

those that have the correct properties. If the geometry is constrained to an extreme degree with the straight capillaric approximation then only one structure results. This structure can be readily calculated from the first derivative of the water retention curve. The simplicity of this calculation makes the approximation dangerously popular, and it is also implicit in the widely accepted equations for calculating hydraulic conductivity from water retention (Mualem, 1976). The Pore-Cor void structure is itself highly constrained, but much less so than the straight capillaric model. So a range of possible structures emerge, and their validity, within their own approximation framework, must be tested by sensitivity analysis.

However, two problems prevent the use of a standard sensitivity analysis, in which the worsening of the fit is examined with respect to the change of every parameter in turn away from its optimum value. The first is that the modelling uses iterative and stochastic methods rather than more standard mathematical equations. The second is that the simplex is working simultaneously in seven dimensions, and the isolated testing of one of them gives little insight into the overall fitting procedure.

The two problems are circumvented in different ways. To cope with the iterative and stochastic nature of the modelling procedure, we use 'stochastic generations'. The Pore-Cor unit cells are generated with a pseudo-random number generator, such that the same structure is always generated from the same parameters, and that slight changes in geometric parameters give structures which are almost identical. For example, if the connectivity was changed from 3.5 to 3.6, and the first structure had a group of large pores near the top of the unit cell, then that same group of large pores would probably be observable in the same place in the structure with connectivity 3.6. The two structures are said to belong to the same 'stochastic generation'. However, there is also the facility to change the seed of the random number generator, producing a different stochastic generation or family of structures. The modelling results described below result from between four and ten different stochastic generations for each water retention curve, and the standard deviations represents the spread of the results between different stochastic generations.

To cope with the multi-dimensional nature of the working of the simplex, two approaches are taken. The first is that we track the movement of the simplex on to its best answer by logging the changes of the four primary fitting parameters close to their optimum values, as shown in Table 6.21. The second method is to scan away from the optimum result with

153

a grid of varying values for two of the four primary parameters. This still represents only a slice through the multidimensional parameter space, and only the centre point has been optimized in all the dimensions. Nevertheless, it gives an insight into the sensitivity of the result with respect to a pair of parameters.

6.4.1 Sensitivity Analysis

To test the modelling method, we chose a set of soils with equal percentages of silt and clay, Figure 6.7(◆). Another set (■) had equal quantities of sand and silt, and varying quantities of clay. All had a density of 1.5 g cm^{-3} and no organic carbon content. In subsequent figures, the samples are referred to only by their percentage of sand.
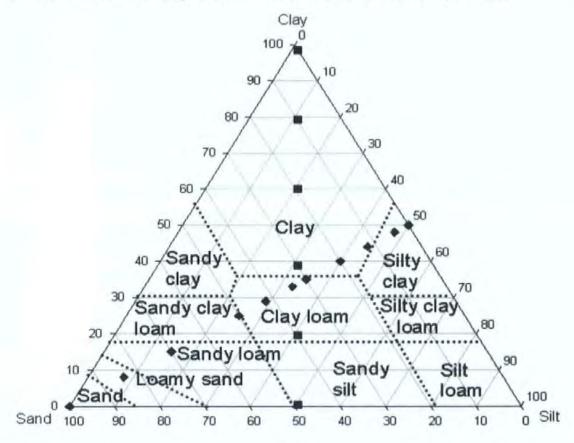
Figure 6.7   Transects of the soil diagram. ◆ refers to samples with equal silt and clay, and ■ to samples with equal sand and silt.

The water retention curves were generated from the NSRI pedo-transfer function, and fitted by the simplex. The extremes of the second set (■) at or near 0% and 100% clay are not typical of English or Welsh soils. They are therefore outside the range of the PTF, and provide less reliable data than the other points. Because the density was fixed, the total porosities of the chosen soils were all similar, in the range 40 - 45%, (except tending towards 100% silt, which is outside the range of soils in the PTF and which we have not studied here). However, much of this water is locked into the soil matrix, and is therefore not extracted by suction. The water retention curves therefore cover a much smaller range

of porosity, and consequently much less porosity is in the modelled range of 0.2 μm to 2500 μm. The extreme example is 100% clay (shown as 0 % sand) where only 2.6% of the total porosity is modelled at this sample density. The pedo-transfer function suggests that even increasing the suction by two orders of magnitude would increase the extracted water to only 7.6%, although this figure is an extrapolation outside the experimental range and should be treated with caution.

Series name	Sand / %	Silt / %	Clay / %	Bulk density /g cm^{-3}	Organic Carbon /%	SLHC[1] /cm day^{-1}	SSVHC[2] /cm day^{-1}
Bardsley	6	46	48	1.43	0.4	0.4	0.7
Claverley	47	28	25	1.75	0.1	8.2	16.1
Clifton	36	32	32	1.64	0.2	4.5	10.8
Conway	22	50	28	1.33	1	30.2	46.4
Gore	25	48	27	1.35	0.7	26.5	41.4
Hamble	9	71	20	1.42	0.2	7.7	15.5
Sollom	98	1	1	1.47	0.1	666	616.5
Waterstock	51	34	15	1.47	0.1	64.3	92.2
Wickham	1	58	41	1.51	0.2	0	0.1

Table 6.2   **The selection of soils from the NSRI database.**

[1]Saturated Lateral Hydraulic Conductivity   [2]Saturated Sub-Vertical Hydraulic Conductivity

Note: data to be used only under licence from National Soil Resource Institute, Cranfield University

Figure 6.8 shows a sensitivity analysis for 34% sand, 33% silt and 33% clay, i.e. for a soil at the centre of Figure 6.7. For graphic purposes, combinations of parameters leading to networks that are invalidated by any of the three secondary dimensions have been allocated a value of 6.6. The optimum values are at the centre of the surface. It can be seen that the fitting is sensitive to throat skew, i.e. the sizes of the voids, but not very sensitive to the connectivity of the network. However, networks with small connectivities fragment, and are therefore invalid.

Figure 6.8 Sensitivity analysis of point 34-33-33, centre of soil texture diagram.

Figure 6.9 shows the variation of connectivity with % sand. In this and subsequent diagrams, ♦ refers to samples with equal silt and clay, and ■ to samples with equal sand and silt, as in Figure 6.7.
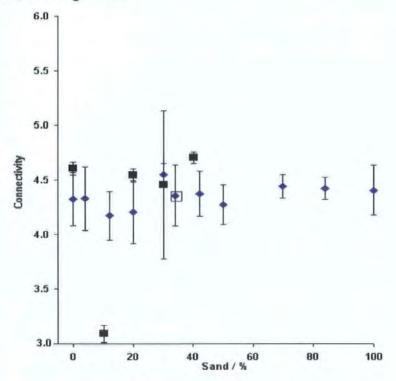
Figure 6.9 Variation in Connectivity with Sand Content

The point at 34% sand, 33% silt and 33% clay is so near equal for all three constituents that it refers to both transects, as indicated. The error bars in these and other graphs refer to simulations with different stochastic generations. The centre point is the mean, and the

156

error limits are + and - one standard deviation. The graph shows that except for one outlier at 10% sand, 10% silt and 80% clay, connectivity changes little. The outlier is one of the unreliable water retention curves, for the two reasons previously explained – i.e. it is outside the range of English and Welsh soils, and a very small percentage of the total void space is being modelled. So although a sensitivity analysis shows that the connectivity is definitely less than for the other samples, not much importance can be given to the result.

On the vertical transect Figure 6.10 (■), the samples with large clay contents become increasingly difficult to model, and that with no sand or silt (100% clay) has huge error bars.
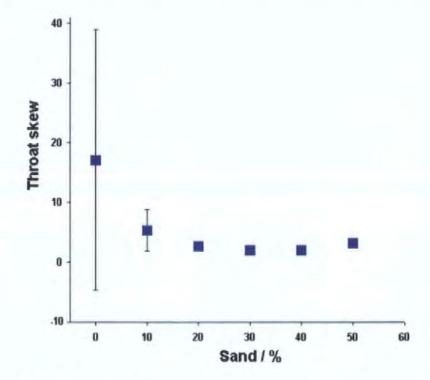
Figure 6.10   Effect of sand on modelled sensitivity.

Figure 6.11 shows that throat skew decreases with increasing % sand for the equal silt and clay samples (♦). This is as expected – the void sizes increase with increasing % sand.
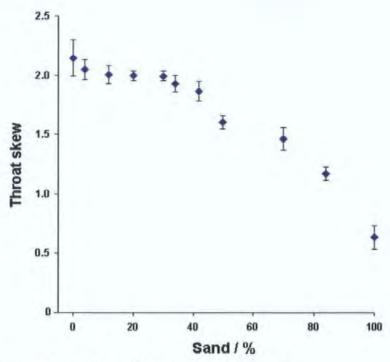
Figure 6.11   Decreasing throat skew with increasing sand content.

Figure 6.12 shows that correlation tends to decrease with increasing % sand, i.e. as expected; the void structure becomes less correlated spatially.
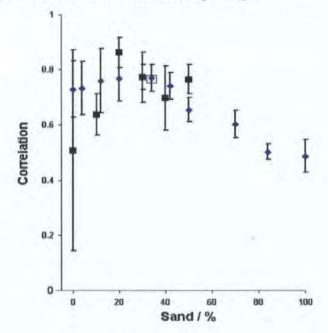
Figure 6.12   Decreasing correlation with increasing sand /%.

Figure 6.13 shows that the saturated hydraulic conductivity increases with increasing % sand along the diagonal transect (♦), as expected. Interestingly, the hydraulic conductivity goes through a maximum at 34% sand in the vertical transect (■) before decreasing by six orders of magnitude as the texture changes to 100% clay.
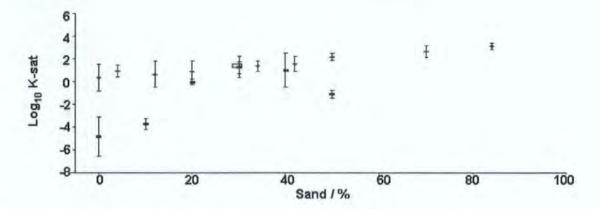
Figure 6.13   K increasing with increasing /% Sand

All the simulations so far have been for soils without any organic carbon, so it is of interest to study the effect of change in this characteristic. Figure 6.14 shows that saturated hydraulic conductivity changes little. The compilers of soil PTFs have found that the addition of organic carbon as a parameter does not produce closer fits to data – i.e. its effects are unsystematic. Hence this may be reflected within the NSRI pedo-transfer function, with the result that no obvious trend re-emerges when the data are modelled.
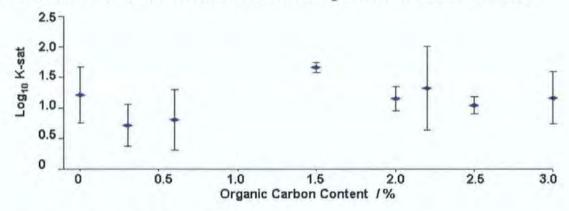
Figure 6.14   The effect of Organic Carbon on K.

Figure 6.15 shows that, as expected, the saturated hydraulic conductivity decreases with increasing bulk density, by some two orders of magnitude on increasing the density from 0.9 to 2.3 g cm^{-3}.
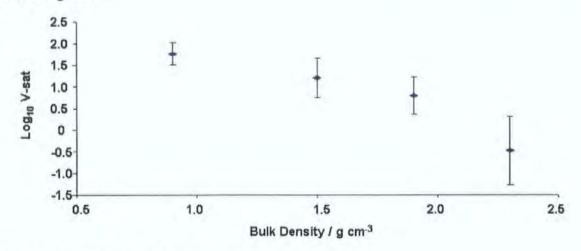
Figure 6.15   K decreasing with increasing bulk density

6.4.2 Trends in behaviour of the simulated structures

So far we have stayed within the realms of simulation, partly because there are no suitable experimental measurements across the whole range of soils with which to compare the simulated results. However, remaining within the realms of simulation leads to a rather sterile academic exercise. One stage back to reality is to examine the differences in structure and property across the range of soils studied. This is facilitated by viewing in a virtual environment within which the user can explore the soil structure and find out where the fluids have gone. Figure 6.16 illustrates a structure drawn using the PTF processed by the Pore-Cor modelling engine. Most of the detail of throats is invisibly small in the diagrams. To emphasize the differences between the structures, therefore, we have applied a tension of 10.0 kPa.
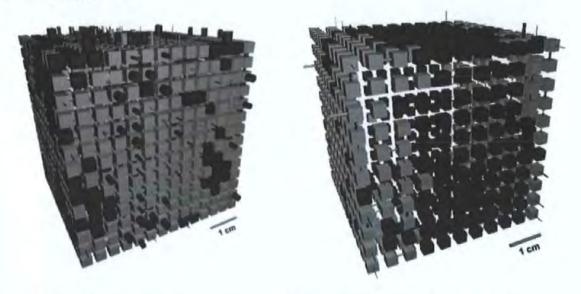
Figure 6.16   Simulated void structures of sand (left), and 50% sand 50% silt right. Structures show distribution of air (grey) displacing water (black), after application of 10.0 kPa.

Air, shown pale grey, has displaced water, shown dark grey. It can be seen that the behaviour of the fluids is entirely different. In the sand, little water is left, and it occurs in pockets randomly distributed throughout the structure. In the 50% silt, 50% clay sample, however, the water resides in a spatially correlated zone of small throats, and much more of it is retained. These characteristics have emerged spontaneously from the model, and closely reflect those found experimentally. Many more simulations are possible – for example with regard to the effect of colloids and non aqueous phase liquids (NAPL) within these structures.

6.4.3 Modelling of Soil Void Structure Using NSRI Experimental Data

6.4.3.1   NSRI Data.

The water retention data derived from the NSRI was the best available at the time of this study. The lost mass of the water at a given pressure head was used to calculate the

corresponding volume of water lost. Table 6.3 shows the bulk density and porosity for each of the samples analysed at the NSRI laboratories. There is only one representative sample of the Conway series due to sample failure in the NSRI laboratory.

	Bulk density (g/cm³)	porosity (/%)	%water volume relative to total volume in this 100g / g vs pressure in kPa					
			1	5	10	40	200	1500
Conway	1.42	46.4	43.8	41.5	40.7	40.4	39.7	39.4
Sollom	1.57	40.6	38.5	36.1	34.9	34.5	33.4	33.1
Sollom	1.25	52.8	31.8	30.0	28.6	26.8	24.8	21.7
Sollom	1.59	39.9	38.7	35.6	34.3	33.5	33.0	32.4
Clifton	1.59	40.0	36.8	35.3	34.5	33.9	32.3	31.8
Clifton	1.33	49.9	36.2	34.6	33.4	31.8	28.2	26.1
Clifton	1.16	56.4	30.9	29.6	27.2	26.9	26.6	26.5
Crediton	1.41	46.8	63.6	42.2	38.0	35.0	33.2	27.4
Crediton	1.25	53.0	56.8	36.5	32.3	31.3	30.9	30.6
Crediton	1.26	52.3	68	38	36	34	28	22

Table 6.3   Water Retention data for the experimental soil samples.

The NSRI measurements were converted to water retention by volume relative to the total void space in each sample, Figure 6.17. It can be noted that the extraction of volumetric water is a time consuming and difficult procedure. The curves produced do however follow an identifiable trend for each soil type and thus have credibility.
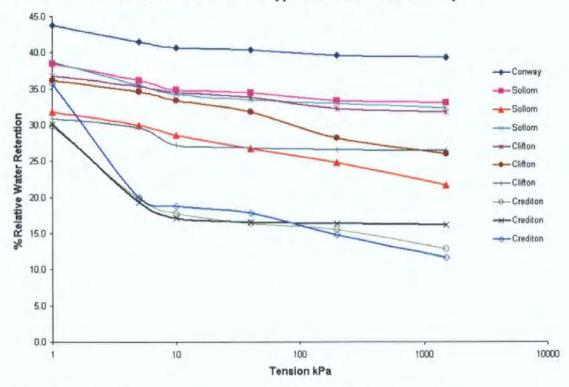
Figure 6.17   Water retention curves as analysed in the NSRI laboratories.

6.4.3.2   Oil Injection Simulations Using the NSRI data set

Using real soil data, the simplex method was able to develop simulated structures. Using the simplex method fits for the soil samples are reported in Table 6.4 and the subsequent

unit cells generated from three curves are shown in Figure 6.18, Figure 6.19 and Figure 6.20. Oil injection into the unit cell was simulated up to a pore size of 300μm.
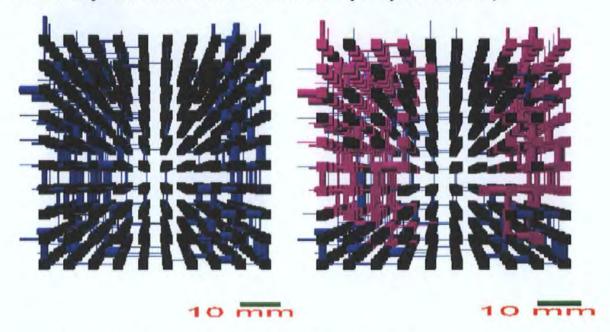
Figure 6.18   Conway (pores grey) & intruded Oil (shown pink); scale 10mm as indicated by the green bar.
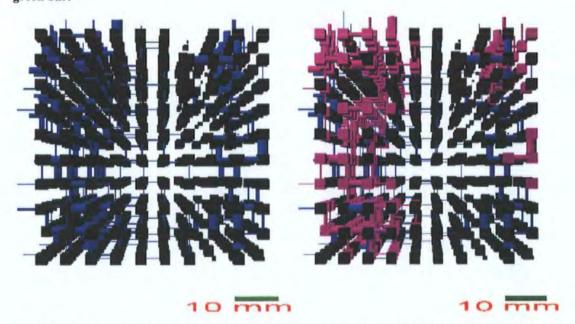
Figure 6.19   Sollom (pores shown grey) & intruded Oil (shown pink)); scale 10mm as indicated by the green bar.
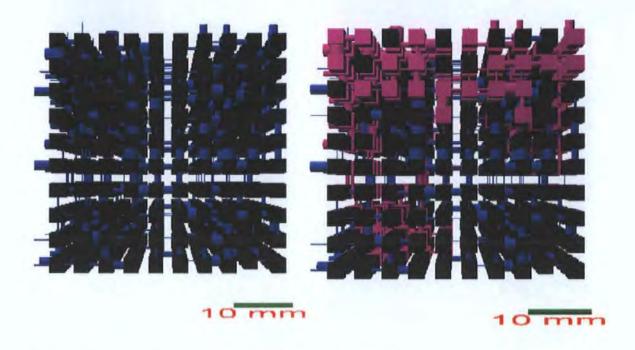
Figure 6.20 Crediton (pores shown grey) & intruded Oil (shown pink); scale 10mm as indicated by the green bar.

Table 6.4 lists some of the parameters used to model the data points and display the structures displayed above. The low experimental porosity for the Sollom and Conway soils relate to the inability of the experimental method to obtain water retention data at these lower pore sizes i.e. for the silt to clay ranges.

Sample Name	Experimental Porosity / %	Simulated Porosity / %	Connectivity	Liquid Permeability / milliDarcies	Throat Skew	Pore Skew	Correlation level	Distance
Conway	7.4	7.393041	4.5363	243.0586	0.93178	4135.4	0.37935	1.766367
Crediton	22.4	22.38386	3.5729	533.9935	0.3071	4052.5	0.14235	1.3478
Sollom	7.5	7.493547	3.1001	318.2957	0.71839	88.761	0.42181	1.146141

Table 6.4 Parameters established for each of the soil types.

It can be seen that the oil distributions agree with the partial fingering flow predicted by the Lenormand approach discussed in section 1.10. Relatively, Sollom (Figure 6.19) contains a much greater dispersion of oil than Conway or Crediton, which agrees with experimental, Table 5.4.

6.5   Pore-Cor oil injection simulations and Hazard Assessment Tool

Using a hazard assessment protocol (or hazard assessment level H.A.L.) developed at the University of Plymouth for NGT, the soils modelled could be classified as to their vulnerability to the transmission of NAPL in the soil. Below a case study of three soil types is described.

Three soils have been selected to illustrate the classification system with which values derived will be integrated into the NGT's own hazard prediction system. The soils were selected for their predicted hazard level i.e. one each from most hazardous, least hazardous

and intermediate value, in relation to there soil texture. It is expected that the sandiest soil would be the most susceptible to intrusion by the oil. The soil textures for the soils selected are shown in Table 6.5.

Soil Type	Sand /%	Silt /%	Clay /%	Porosity /%	Hazard Assessment Level
Wickham	0	56	44	16.48	1
Malling	27	18	55	11.65	3
Fyfield	84	5	11	35.43	5

Table 6.5   Textures for the test case soils and their Hazard Assessment Level (H.A.L.).

A question that should be asked is *"Why model, when the porosity is already known?"*. Figure 6.21 illustrates that it does not follow that the porosity of a particular soil sample will yield a linear relationship with the sample's permeability, i.e. an increasingly large porosity will yield an increasingly large permeability. This is disregarding important principles in porous media such as tortuosity, connectivity and void space distribution. It was therefore important to develop sound models to interpret and convert the 2-D water retention curves into 3-D structures from which salient properties of the material can be devised. Parameters for the stochastic generations yielded by the Pore-Cor model can be seen in Table 6.6.

Pore Size µm	Wickham	Fyfield	Malling
2500	0	0	0
1500	5.46E-03	3.164566	2.92E-02
750	3.09E-02	16.61658	0.164694
250	0.30397	40.43844	1.616058
30	17.55077	70.66477	29.69034
6	47.42839	84.56516	54.20827
3	59.24014	88.93884	64.17825
1.20	73.95446	93.59468	76.84165
0.75	81.12354	95.56989	83.11717
0.37	91.25222	98.08122	92.10928
0.272	95.73472	99.09705	96.13741
0.20	100	100	100

Table 6.6   Air intrusion data for the test cases.

Examining Figure 6.21 it can be seen that a soil (Cuckney) with a permeability higher than that of others is not as permeable as some soils with a lower porosity. The structure once generated can then be modified by using various processes such as oil injection, colloid injection and anisotropic mechanisms. This process has allowed the comparison of the behaviour of structures from data derived via the NSRI pedo transfer function.
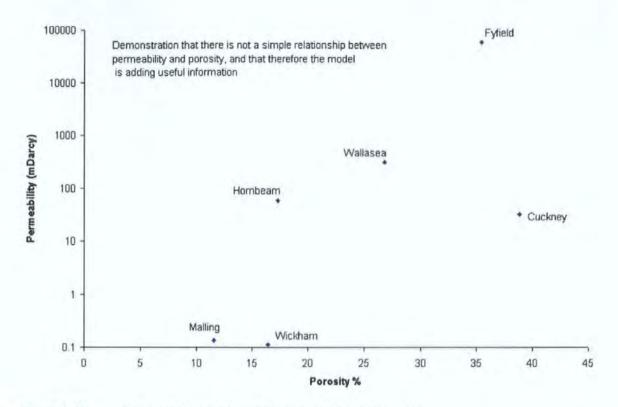
Figure 6.21   Relationships between soils permeability and porosity.

Table 6.6 and Figure 6.22 are the air intrusion curves to be modelled by Pore-Cor. Ten stochastic generations were produced for each of the structures.
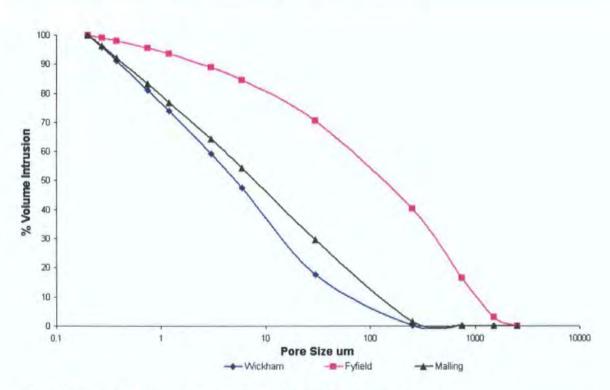
Figure 6.22   The Water Retention Curves in a Usable Pore-Cor format.

It was assumed that the hazard level of each soil type could be judged by a combination of hydraulic conductivity (high liquid permeability = high risk) and air pressure at breakthrough (high pressure required for a non-wetting fluid to break though from one side of the sample to the other = low risk). It was arbitrarily assumed that an increase of 2

orders of magnitude of liquid permeability increases the risk of NAPL migration by the same amount as a decrease of one order of magnitude of break-through pressure, the latter being a much more sensitive parameter. The results were then plotted on graphs of the type shown in Figure 6.23. The total range of results was then split into five equal zones corresponding to five hazard levels, from 1 (low risk) to 5 (high risk) as shown. The clusters represent different stochastic generations of the same experimental data, rather than variations in experimental data. The results are summarised in Table 6.7.
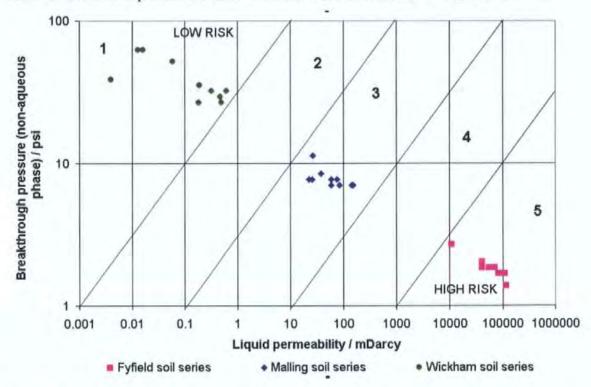
Figure 6.23   The hazard assessment level risk estimation chart.

Sample Name	Stochastic Generation Number	Experimental Porosity	Connectivity	PermLiq (mDarcy)	Throat Skew	Pore Skew	Correlation Level	Standard Deviation	Breakthrough % Volume	Breakthrough Pore Diamater
Fyfield	1	35.439	3.5916	69315.24	0.8954	643.18	0.74009	1.41	15.2972	796.8289
Fyfield	2	35.439	4.3126	54908.97	0.9295	11247	0.6236	1.57	20.4452	796.8289
Fyfield	3	35.439	5.2132	40455.01	1.134	7746.9	0.5448	1.61	16.8727	724.4061
Fyfield	4	35.439	3.1638	10961.11	0.47379	2189.7	0.64872	1.22	28.5589	544.2939
Fyfield	5	35.439	3.488	96864.36	0.621	10919	0.7117	1.25	12.1949	876.4921
Fyfield	6	35.439	3.5823	115575.8	0.74628	1954.9	0.62085	1.32	8.88036	1060.508
Fyfield	7	35.439	3.2832	978250.7	0.45825	12209	0.92899	1.42	10.3048	1707.767
Fyfield	8	35.439	3.3341	83417.59	0.40963	8493.9	0.66538	1.23	18.3821	876.4921
Fyfield	9	35.439	3.488	40438.55	0.721	1374.7	0.7516	1.44	16.6033	796.8289
Fyfield	10	35.439	4.1287	107978.7	0.9128	1730.6	0.7516	1.59	18.5618	876.4921
Malling	1	11.658	4.1368	84.87392	1.9782	12277	0.91129	0.97	12.4237	209.8959
Malling	2	11.658	3.4762	59.05554	1.9434	8771.1	0.9079	1.04	10.5796	209.8959
Malling	3	11.658	5.4866	153.0975	2.0618	5784.8	0.86056	1.23	12.7818	209.8959
Malling	4	11.658	5.5186	22.60684	2.1437	6995.4	0.84563	1.15	9.73963	190.8188
Malling	5	11.658	4.2596	59.75401	2.023	9422.1	0.91242	0.93	14.5099	190.8188
Malling	6	11.658	3.4669	25.52837	1.9607	6632.1	0.81733	0.90	12.827	190.8188
Malling	7	11.658	4.7771	26.10807	2.0645	10295	0.8147	1.03	16.1385	130.3435
Malling	8	11.658	5.5208	75.46628	2.0791	5364.7	0.89736	1.25	14.5194	190.8188
Malling	9	11.658	5.6066	37.42212	2.1549	8880.9	0.83351	1.23	13.2086	173.4756
Malling	10	11.658	5.6456	143.3971	2.067	8385.3	0.86982	1.22	14.8752	209.8959
Wickham	1	16.481	3.3524	1.28E-02	2.0206	9042.9	0.58518	0.78	27.0288	23.4529
Wickham	2	16.481	3.1956	5.89E-02	2.2525	4919.5	0.88963	0.91	25.4759	28.37674
Wickham	3	16.481	4.7079	0.189909	2.8903	12176	0.88903	1.05	15.3132	41.54265
Wickham	4	16.481	4.707	0.3230458	2.89	12176	0.889	1.22	13.1259	45.69589
Wickham	5	16.481	4.8949	0.5024673	2.8285	12113	0.90161	1.09	11.7131	55.28955
Wickham	6	16.481	5.3001	0.6318302	2.8909	10068	0.81588	1.11	13.6169	45.69589
Wickham	7	16.481	3.7001	0.0158926	2.372	6352.3	0.7658	1.08	24.0687	23.4529
Wickham	8	16.481	5.473	0.4774887	3.0253	12483	0.83836	1.15	12.0106	50.26435
Wickham	9	16.481	4.018	0.1857131	2.4817	11086	0.7656	1.10	10.8535	55.28955
Wickham	10	16.481	4.6807	4.04E-03	2.8141	12204	0.86074	1.07	16.2163	37.76691

Table 6.7   Pore-Cor Parameters for the test samples

Figure 6.24 shows three of the simulated structures after oil injection at the same pressure. These structures clearly show an increase in the permeation of NAPL displacing air from within the unit cell. The hazard assessment level for each structure also clearly predicts that this will be the case.

Wickham	Malling	Fyfield
H.A.L. 1	3	5

*Hazard Assessment Level
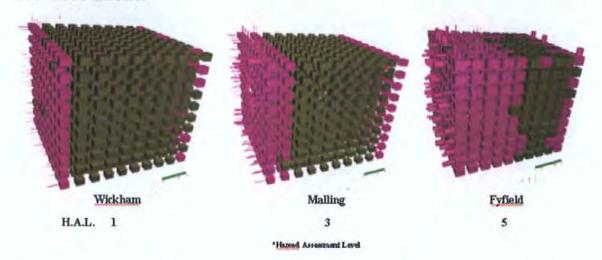
Figure 6.24 **Hazard assessment level (H.A.L) modelling of oil injection into simulated Pore-Cor structures. Oil (shown Pink), displacing air in the soil voids (shown grey).**

6.6   Summary

A network model capable of predicting experimental properties of porous media has been described. Through experimental observation and model development this study aimed to enhance understanding of porous materials by improvement of the network model and by its appropriate application to situations that might benefit from this. The three objectives outlined at the start of this chapter (Section 6.1) were all achieved to a satisfactory level. In summary, in this chapter it has been shown that:

- A simplex 'brain' has been added to the Pore-Cor network model allowing it to explore parameter space and hence a wider range of water retention curves. The model also gained the capability to successfully model sparse data sets such as those produced by water retention experiments. The fitting parameters could be explicitly related to the void structure of the experimental samples. They are therefore an advance on the more traditional fitting curves such as the van Genuchten equation.

Objective 1   To use the Pore-Scale model (Pore-Cor) with water retention curves generated by a pedo transfer function and to assess the usefulness of the model.

- Objective 1 was achieved. It was shown that the model produces sensitive trends across English & Welsh soils as represented by simulated PTF's, and error bars should the range of results produced by different stochastic realisations. Any results used outside of the PTF's domain (in this case English and Welsh soils) should be treated with caution.

Objective 2   To interpret the results to reveal the additional information obtainable.

- From the modelled parameters it was possible to construct 3d structures giving a simplified representation of the soil structure. Using these structures it was possible to simulate processes such as oil intrusion, which agreed with the experimental results of Chapter 5.

Objective 3   To attempt to extend the model and apply it to real soil samples.

- We found that we could successfully model soil water retention curves derived from real soil samples and produce structures and parameters in accordance with those expected from the experimental data.

- Using experimentally derived soil water retention data from the NSRI, three soils were analysed. The results of the analysis were used in the development of a system that can be used to assign a ranking to each soil which could be subsequently integrated into a pre-existing hazard assessment framework.

7 Summary, Discussion and Future Work

Soil is arguably one of the most complicated of all media to study. The work in this thesis has covered an unusually wide range, from field work through laboratory work to intensive computer programming and modelling. So an ambitious span of work has been carried out on a very complicated media type. In this overview, we attempt to pull together the many strands of the work to assess the overall conclusions, and the extent to which this doctorate project has furthered the progress of soil research.

7.1 Hypotheses

The question that this project proposed (Section 1.3) "Can pore scale modelling of soil be validated against experiments at core and 0.5m scale, and used to produce results of national importance?". We believe that on the basis of this study the answer to both parts of this question is "Yes".

For the modelling work we had to:

i. Introduce a Boltzmann-annealed simplex 'brain' to the Pore-Cor model.

ii. Design and implement a database to handle the large volume of parameters and iterations necessary for use of the model.

To gather the necessary high-resolution data we had to:

i. Develop, construct and operate a new automated lysimeter (Johnson *et al.*, 2003).

ii. Develop experimental protocols that would gain the maximum benefit from the automated functionality of the Skalar auto-analyser and the Beckman Scintillation counter.

The theoretical and experimental advances allowed us to discover entirely new results.

With respect to the modelling we found that

i. The Pore-Cor model produces sensible trends across the whole of the English and Welsh soils, when based on NSRI pedo-transfer function (Johnson *et al.* 2003).

ii. The model predicts the correct partial fingering flow of NAPL through these soils.

With respect to the experimental results, we found that:

i. The addition of cable oil does not significantly alter the water flow patterns.

ii. The bromide breakthrough curve peaks are suppressed by oil.

iii. The phosphate breakthroughs are much more random than bromide, and are also suppressed.

Having summarised the achievements of the project, we will now discuss the conclusions, and consider a more explicit approach to upscaling which could be used in future work.

7.2 Experimental Methods

The initial experimentation comprised trials on the Crediton soil core and 0.5m soil block which established a usable protocol for the analysis of the other soil samples. The analytical techniques, although not new in themselves, had to be developed and tested for analysis time, reagent consumption and equipment maintenance. The protocol and maintenance regime established for the Skalar SFA enabled efficient analysis of large numbers of samples produced during the 0.5 m core experiments.

The main experimental advance was to carry out high-resolution measurements on soil blocks, which at 0.5 m are large enough to be representative, but just small enough for experimental parameters such as rainfall to be controlled. To avoid the need to extract and mount 0.5 m cores, which weigh around half a tonne, repacking of soil samples was attempted. However, it has been shown in this work (Figure 4.11) that repacking severely alters the flow characteristics of the soil sample. So a protocol was developed and carried out to mount intact 0.5 m blocks of soil in the precision lysimeter.

7.3 Experimental Results

Table 7.1 is a summary of the experimental results produced by analysis of the soil blocks using the automated lysimeter. The experimental analysis of the soil blocks was necessary to analyse the validity of the predictions of the Pore-Cor computer model. To try and draw the strands of the project together we must attempt to understand the experimental results.

The experimental results clearly show the suppression of bromide and phosphate tracers by introduction of oil into the tracer injection site. This caused a lag in the breakthrough curves observed at the base of the soil block (Figure 5.24 & Figure 5.41). From the 3-D plots (Figure 5.26 & Figure 5.42) it could be seen that the previous high flow capacity channels were disrupted by the oil flow, although the actual elution rates of the funnels remained unaffected (Figure 5.8). This suggests that the oil was preventing the tracer dispersing to its previously preferred route through the sample block. This therefore leaves us with two postulates:

i. If the oil is suppressing the expected pulse, then this pulse must interact with the oil as a buffer. However, the reservoir characteristics of the oil are clearly not the same as those for e.g. soil with phosphate – the shape of the breakthrough curves come out flat rather than peak with a long tail expected by high reservoir capacity.

171

ii. So another postulate is that the oil is restricting the number of channels through which the bromide or phosphate is flowing, and that these are acting as constant-flux type of transport of the dissolved species.

If we take into account the flow sequences shown in Figure 1.19 we may propose a method of oil migration which precludes bromide from the flow paths in the soil matrix. If we consider Figure 1.19 a and b we would hypothesise that the oil would migrate through the soil body in this fashion.

We can conclude from analysis of the 3-D plots and statistical analysis of the tracers (Section 5.5.2) that visible trends are revealed relating to the retardation of tracer migration by the oil in the soil. Figure 7.1 is a schematic representation of the different processes which we believe occurred after oil injection into the soil block, ands the retarding mechanisms involved in delaying the tracers. The blue arrows indicate the preferential path taken by water passing through the soil. Figure 7.1 a, shows a flow channel and a single pore as indicated exposed to the channel. As water migrates past the opening to this channel the water from the pore will be drawn through. This drawdown effect is a common hydro-geological phenomenon around oil wells and bore holes. Following from this the small scale draw down effects in a capillary tube (analogous to our preferential flow path) can be assumed. As shown in Figure 7.1 b, bromide was introduced into the soil sample and if trapped in such a pore as Figure 7.1 b, then the Br will be allowed to migrate from the pore body and be drawn into the preferential flow path and eluted from the base of the soil block rapidly. Evidence for this can be seen in Chapter 5; Figures 5.38-5.40 show that in the pre oil injection samples, the bromide is found in discrete locations.

After oil injection the soil peak heights are greatly reduced, and the mechanism for this can be explained in figure 7.1 C. As the NAPL was injected it then migrated through the soil body (Figures 5.24-5.26). The experiments conducted during this study allowed 8 hours between oil injection and secondary tracer injection so any bromide trying to access the preferential pores containing NAPL would find there progress inhibited. As NAPL passed through the soil body dispersing it would leave a residual trace of oil. This effect has been observed by workers such as Dullen, 1992 where oil blobs can be trapped in water wet oil reservoir. These oil blobs if trapped at key areas would inhibit the transport of bromide pores and prevent the elution of bromide from the base of the soil block. Mercer and Cohen, (1990) also noted the residual NAPL becoming trapped in the soil body by gravity migration of the NAPL. After Figure 7.1 d we would revert to a situation as shown in figure 1.17 b, a modified version of which is repeated, for convenience, in Figure 7.2   Zones of fluid

flow and relation to found oil distributions2, with films of oil around the soil particles and with bromide flow becoming less inhibited as the NAPL plume becomes more dispersed in the soil matrix.
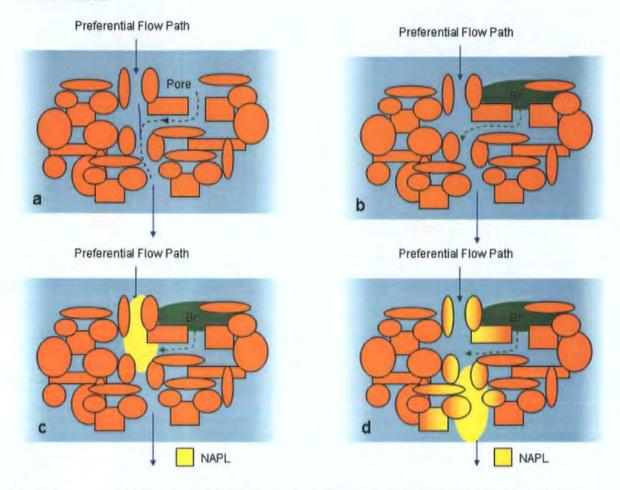
Figure 7.1   Diagrammatic Representation of oil retardation mechanism of the bromide tracer.

Referring to Figure 7.2 it can be summarized that the oil injection initially behaved as in Figure 1.19 a, with the oil forming an exclusion zone and 2 phase flow occurring. As the oil becomes more dispersed we can compare the flow mechanism to that as seen in Figure 1.19 b. Finally we may express oil flow as seen in Figure 1.19 d as there is a small amount of oil flowing in a large excess of water. Figure 7.2 illustrates the changing zones in these flow regimes.

Relating the distributions as described by Dullen to the actual distributions we can see localized concentrations of oil. However the majority of the oil formed a fingering pattern through the soil body in the Crediton and Conway samples. In contrast the Sollom sample formed a lens. This may be due to two factors: either an impenetrable layer in the soil (Thompson *et al*, 1992) or the soil water table (Figure 5.5) was over 40% volumetric water content at this depth and may have prevented the LNAPL from migrating any further into the soil body as reported by (Butts & Jensen 1996).
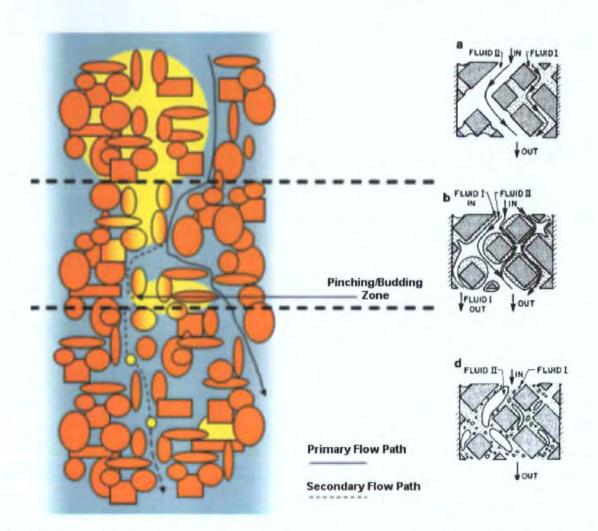
Figure 7.2　　Zones of fluid flow and relation to found oil distributions. Figure 1.19 reproduced on the right.

Property Soil Series	Texture	χ^2 Analysis of Flow Rates	Overall K @ 6.4 mL / h	Graphical Analysis of Preferential flow	Bromide Analysis Pre Oil Top	Phosphate Analysis - Pre Oil Top	Oil Permeation
					Post oil bottom	Post Oil Bottom	
Crediton	Sandy Loam	Flow rates in both experiments internally consistent. Oil addition alters the flow patterns increasing χ^2 when comparing experiments. The modified χ^2 when comparing the pre- and post- oil experiments indicates a different flow pattern was formed, from the base of the soil block was .	2nd most hydraulic conductive.	Preferential flow occurred towards the edge of the collection plate with 59% pre oil – 57% post oil.	The Crediton soil produced the quickest breakthrough curve 3500 mg L^{-1} / h @ 16 hours	330 mg L^{-1} / h @ 20 hours	The Crediton soil sample was the most permeable with a lobe extending 25cm into the soil block. With lobes branching from the main intrusion site for approximately 5cm laterally.
					The oil caused the retardation of the bromide and increased the length of the time taken for the breakthrough to 1500 mg L^{-1} / h @ 20 hours	40 mg L^{-1} / h @ 32 hours	

Sollom	Clay Loam	An initial period of instability in the pre oil sample existed for 8 hours, but stabilised afterwards. The χ^2 value when comparing the 2 samples indicated a change in flow patterns analogous to unstable flow conditions.	1st and most permeable through the soil body	81% pre – 71% post oil, of the collection plate had water passing through it.	The Sollom soil sample was the 2nd curve 2900 mg L^{-1} / h @ 12 hours	300 mg L^{-1} / h @ 36 hours	The Sollom soil was the least permeable to the oil with a lense forming at approximately 10 cm depth.
					1500 mg L^{-1} / h @ 20 hours	120 mg L^{-1} / h @ 12 hours	
Conway	Silty Clay	The Conway pre oil injected sample initially was unstable for 12 hours, but settled afterwards. Comparing the two samples pre- and post-oil the highest χ^2 value was found.	3rd and least hydraulic conductivity of water through the soil body	31% pre oil – 21% post oil of the funnels were utilised to collect water from this sample.	The Conway sample was the slowest 1500 mg L^{-1} / h @ 24 hours	$\times$	The Conway soil formed a single lobe penetrating vertically for 15 cm before moving laterally 5-10cm and then a further migration of 5 cm vertically.

Table 7.1   Summary of the results of the experiments conducted on the Soil blocks.

7.4 Modelling Methodology & Application

The results in Chapter 6 suggest that the new method of characterizing the void structures of soils seems potentially very powerful. The simulated structures show the expected behaviour of real samples, and for example reveal that void sizes do change across the soil texture diagram, but connectivities vary little. This can be used to predict the transmissivity of soils to different contaminants.

7.4.1 Software Advancements

Prior to the installation of the Boltzmann-annealed simplex 'brain', the use of Pore-Cor to model the void structure of soil was an extremely laborious and time consuming process. The incorporation of the simplex required very great effort, but has now allowed the time-efficent production of very large number of stochastic realizations of structures, and consequently a robust sensitivity anlysis (Figure 6.8). It is now therefore possible to predict the relative hydraulic conductivity and other useful pore level properties of a soil. The simulations can be derived either from an experimental water retention curve, or from a pedo-transfer function, or indeed from the UNSODA database of US soils which were not investigated in this work. The model is therefore highly versatile in its use of data. The parameters derived from the model are stored in a sophisticated database developed within this project (Section 2.2.1). This database allows simple retrieval of complex data sets for later review. This increases the usability of the software by also allowing separate archives of modelled datasets, for sensitivity analysis and review.

7.4.2 Upscaling Discussion

In this work, we have compared the results of a pore-scale model with 0.5m scale lysimeter tests. We have therefore implicitly upscaled the pore-scale for comparison purposes. In reference to the question of upscaling our model results to core samples, it must be noted that the field of upscaling is constantly studied and revaluated in the fields of catchment and porous media studies. Here we have attempted to quantify the results of the 'real' soil blocks analysed in the laboratory using the new method developed to statistically analyse the oil distributions (Section 5.7.2). The method developed could be modified to analyse the microscale Pore-Cor model. However this is way beyond the scope of the current studies and will be appearing in a publication following this thesis. We therefore discuss the upscalability of our results and distribution comparisons within the context of current scientific thought and understanding.

The soil structures shown in Figure 7.3 reflect the fingering flow of the oil as shown in the experimental results, Table 5.4 (p141). The distribution of oil at the 0.5m scale was analysed by a simple auto-correlation method (Section 5.7.2). The same method could be applied to the Pore-Cor model, and will be the subject of future work. Figure 7.3 is a comparison of each of the Pore-Cor structures to each of the real life samples. The oil penetration as shown in Figure 7.3 was greatest in the Crediton sample, which is reflected in the model's representation. It can be observed that the model behaves as expected with the Crediton soil having the greatest penetrated pore volume. The Conway sample reflects the experimental results with both sides of the unit cell becoming filled with oil, whereas only the left hand side of the Sollom soil showing any oil migration.

Crediton	Sollom	Conway

| 0.41 | 0.14 | 0.40 |
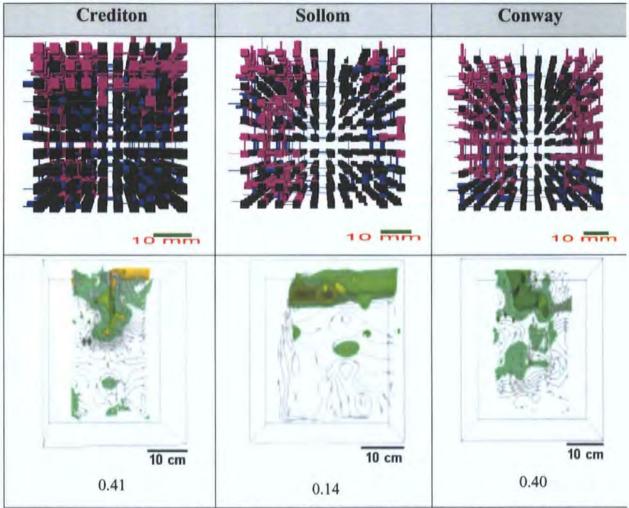
Figure 7.3 Pore-Cor model and experimental results comparison. Figure at the base of row 2 is the numerical similarity of the oil distributions as calculated by the variance method Section 5.7.3.

The major challenge is to produce models with predictive power concerning fast transport of pollutants through macropores, preferential flow due to the spatial variability of hydraulic properties or the instability of wetting fronts which results in fingering flow. The requirement for models to predict the pollution of groundwater by agrichemicals, the construction of waste disposal sites or the remediation of contaminated soils is still a highly desired tool. Given a specific soil, conditions and a specific tracer, what will be the

distribution of the tracers under these conditions? The primary consideration in the upscaling of a porous medium is the homogeneity of the soil, Nielsen et al (1973).

Vogel & Roth (2003) describe a system known as "The Scaleway" which is based on explicit consideration of spatial structure. The model proposed by Vogel is a contrasting theory to other models which rely on perturbation theories based on macroscopic homogeneity and the existence of a finite correlation length with the ability to predict flow at a specific site at a specific scale. The scaleway can be demonstrated most effectively using discrete hierarchical units for which the structural units can be clearly distinguished. The process is based on the fact that microscopic details average out at the macroscopic scale and hence, only the macroscopic structure is relevant. Vogel states that this method will apply to linear diffusion (Hammel & Roth, 1998), but it may not be true for others. A process this rule may not hold for is the displacement of water in a soil structure with air. Here structural features at the microscopic scale may control the macroscopic behaviour.

Figure 7.4 an arbitrary scale is chosen which is to be described by the material properties. At a particular scale a particular structure, where the different structural units are labelled by a certain texture. The structure is directly observable by appropriate instruments irrespective of the scale of observation. It is further assumed that detected structural units are associated with specific material properties that govern flow and transport. Consequently the textures of the different structural units are associated with a set of material properties. A simple relationship of this type would be the soil water characteristic and the hydraulic conductivity function. The appropriate process model, would comprise Stokes equations at the pore-scale, or the Richards' equation at the continuum scale. Then, the effective properties at a given observation scale can be calculated. These effective properties may represent the material properties of a structural unit at the next larger scale. Vogel also reports not only the effective production of parameters at the scale of observation but at the next larger scale. Additionally the complete phenomenology without invoking effective processes is available at the scale of observation provided the underlying process model is correct. The predictive effective behaviour can therefore be predicted due to the continuous structure of the relevant material properties being available.

large scale

small scale
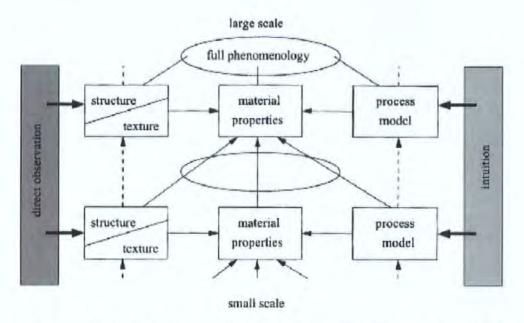
Figure 7.4 The Scaleway Vogel & Roth (2003). At each scale we observe structural units distinguished by their texture which is associated with a set of material properties. The structure of material properties together with an appropriate process model are necessary but sufficient ingredients to calculate the full phenomenology at the next larger scale and effective material properties at this larger scale.

Entry to the scaleway demands some knowledge of the structure. However techniques that reveal structure, such as mercury porosimmetry, do not reveal the underlying process model for a property such as hydraulic conductivity. It is therefore necessary to measure the structure of a property that is correlated with the variables of interest and use such proxy variables to distinguish between different structural units. Fundamentally, observation of the structure must be conducted whenever possible; however if this is not possible then the smaller more convoluted structure, material properties and process model must be calculated. The process models as descried by Vogel and Roth are *ad hoc* formulations based on experiences and intuition.

Vogel & Roth's method is not restricted by the type of forms or structure, be they uniform, irregular, fractal or regular. The price for this is the inability to predict anything beyond the scale of observation. Natural forms are inherently multi scale but Vogel does not consider this a limitation. For example in a soil the separation of the soil material into structural units of dense aggregates in a loose matrix is not obvious. The hierarchy may therefore be considered continuous. As there is no clear lower limit for the size of aggregates and therefore which aggregates comprise dense structural units and which aggregates are small enough to be part of the loose matrix. This is not a severe problem when associated with the process of solute transport as they are dissipative processes. So the breakthrough curves of

solute pulses are mainly affected by coarse structural elements while the tiny details are smeared out.

Described in Vogel & Roth's paper is a method of application of the model to a Br⁻ tracer. Figure 7.5 is a plot of the models predictions against plotted data points. The method illustrates a satisfactory prediction especially when compared to the mobile –immobile model (van Genuchtchen and Wierenga, 1976). The latter is a description of the experimental data found, not a prediction. This limitation is similar to the van Genuchten water retention curves as described in section 6.1.
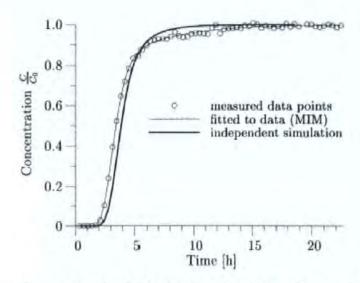
Figure 7.5   The Scaleway Vogel & Roth (2003). Breakthrough curve of a conservative tracer.

This method could feasibly be modified in prediction of the oil intrusion into the different soil texture/structure relationships. Figure 7.6 is a modification of Figure 7.1 revealing important parameters which may be considered when upscaling for a prediction of our oil distribution model. The oil retention model should rely more on the structure measurements of the soil rather than the hydraulic conductivity as this motion may be more susceptible to structural perturbation than just the hydraulic capabilitites.
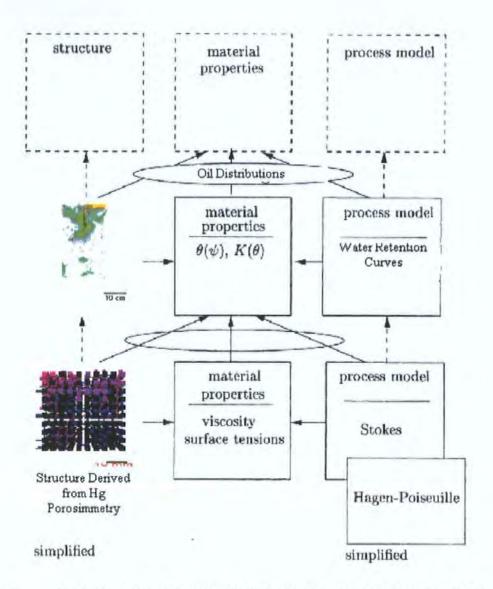
Figure 7.6 The Scaleway Vogel & Roth (2003). Modified protocol for derivation of oil distributions in other soil types with increasing scale.

A proposed method using the Scaleway would be to analyse the microstructure of the soil using Hg porosimmetry and model the curve (analogous to air intrusion data) using the Pore-Cor software. The microscale predictions could then be combined with the larger scale water retention details at the tens of cm scale. This in turn could then be upscaled to the 1m scale. Obviously the coarsening of the findings will greatly effect the accuracy of the prediction as we move up the scale, making more assumptions and rounding errors. To solve this problem even for these two scales numerically is far beyond the scope of this work. However we have identified a suitable framework that can be modified for the analysis and prediction of oil transport properties moving through the scales desired.

7.4.3 Current Capabilities

However in our current work we have identified a framework for numerically quantifying the distributions (variance) of oil in a real space sample. In Table 5.4 (p141) the fingering flow of the Conway and Crediton soil was successfully identified by the calculation of

variance in the oil distribution, with the more lens like Sollom distribution giving a much lower variance. Direct comparison with the Pore-Cor pore scale model is not yet feasible. However the Scaleway framework identifies a good possible system of upscaling the pore level data to a larger cm scale. The major limitation of the Pore-Cor model remains the inflexibility of its pore structure, trapped in a Cartesian grid. However although the model is a still simplistic geometrically, it represents a major improvement on the traditional capillary bundle model. Based on only a water retention curve, it can re-create the partial fingering behaviour of NAPL in soil on a scale of centimetres.

7.5 Future Work

Improvements in the experimental apparatus could be made by the introduction of real time data logging and analysis of leachates, leading to removal of sample storage issues completely. Simple flow injection analysers could be attached to the apparatus to automatically analyse leachates for tracers. Other factors such as sample saturation, pH and temperature and waste channel flow rates could all be automatically logged. This would create a closed system in which all inputs and outputs could be analysed and accounted for.

The integration of additional pedo-transfer functions for different countries would extend the use of the software, which is currently restricted to English and Welsh soils and the American UNSODA dataset. A major issue highlighted by this project is the lack of water retention data of good quality. Such data form the foundation of pedo-transfer functions, which need to be reliable. Water retention measurements should also be usable as raw data. At present, many data points are widely scattered, and do not agree with the known porosity of the soil. So the modelling of pedo-transfer data, and especially of raw data, is severely hampered.

Meanwhile advances have already been made in the model. (Bodurtha *et al., 2001*) have studied anisotropic structures, and Laudone *et al.* are working on the "skeletal elements" (representative particles) between the pores. These could also be used in conjunction with the upscaling method discussed in Section 7.4.2.

The model is also finding use for a wide range of materials, including catalyst substrates, sandstone oil-reservoir sandstone, paper coatings and sintered castings. These new applications are benefiting from the incorporation of the simplex, developed in this project because of the demands of modelling soil.

I. Appendix 1

Figure I.1, Figure I.2, Figure I.3, Figure I.4, Figure I.5 & Figure I.6 are the flow from each of the funnels during all of the experiments for all of the experimental soil samples analysed pre and post oil injection.

Figure I.7, Figure I.8, Figure I.9 and Figure I.12 are high-resolution plots of bromide breakthroughs from each separate funnel flux over all experiments. The best examples of standard bromide behaviour can be seen in Crediton funnels 1-10 and Sollom 1-20. They are characterised by a typical conservative tracer curve, with a high peak followed by a diminishing tail. It is observable from the Conway soils that very few funnels conducted bromide suggesting a very high preferential flow network. This when compared to Sollom & Crediton that has greater quantities of funnels conducting the bromide.

Figure I.13, Figure I.14, Figure I.15, Figure I.16 and Figure I.17 is a high-resolution plot of each of the funnels phosphate flux throughout the experiment. The high-resolution analysis allows individual sections of the lysimeter grid to be analysed for behaviour. The overall phosphate patterns are quite erratic, unlike the bromide that provided a smoother more predictable curve.

The Conway had very few funnels conducting phosphate, until the 36th hour. This is a uniform distribution throughout all funnels. A good illustration of the retardation of the phosphate is shown in the Crediton series. A marked number of funnels have reduced there conduction of phosphate. The Sollom soil appears to be least affected by the injection of the oil.
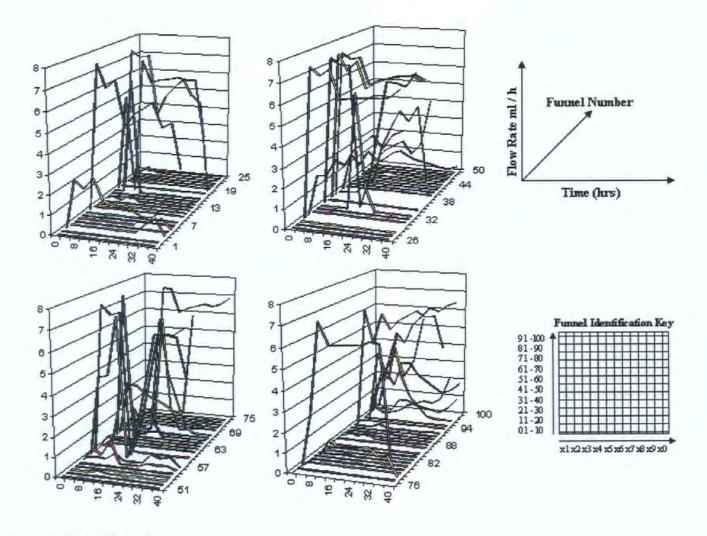
Figure I.1   Conway flow rates after oil injection.
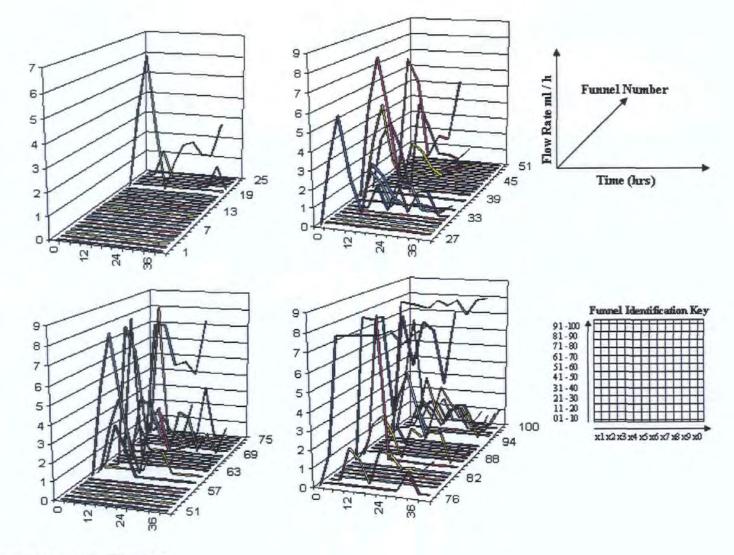
Figure I.2   Conway flow rates pre oil injection.
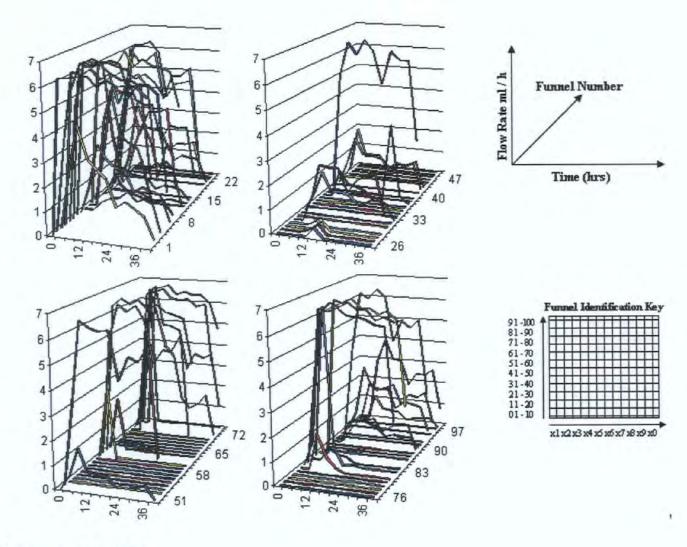
Figure I.3   Crediton flow rates pre oil injection.
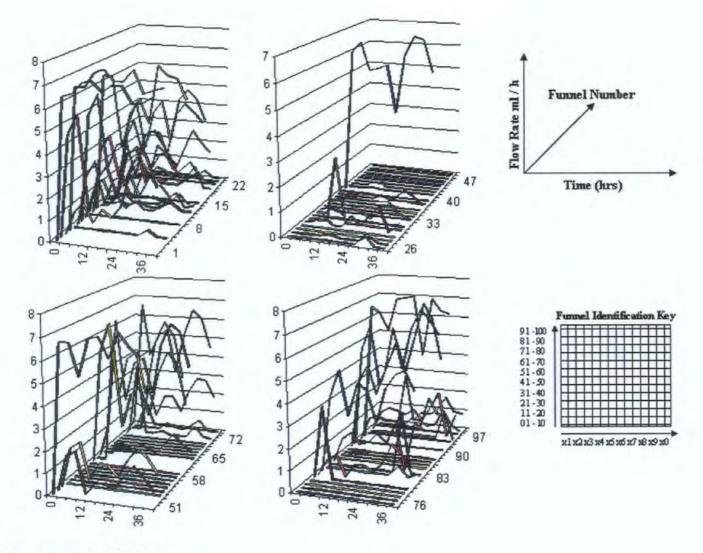
Figure I.4   **Crediton flow rates after oil injection.**

188
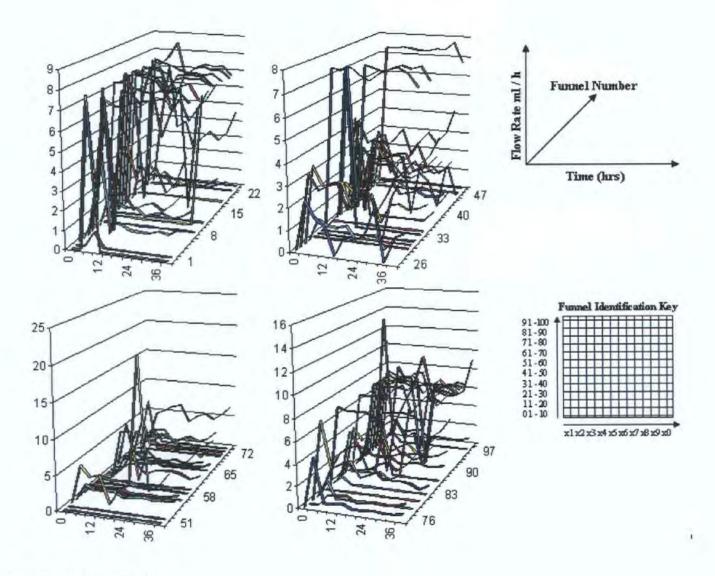
Figure I.5　　Sollom flow rates pre oil injection.

189
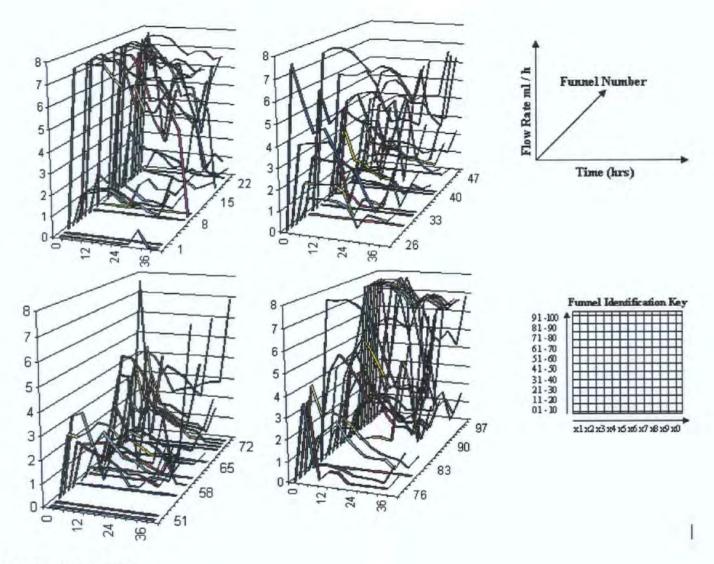
Figure I.6   Sollom flow rates after oil injection.
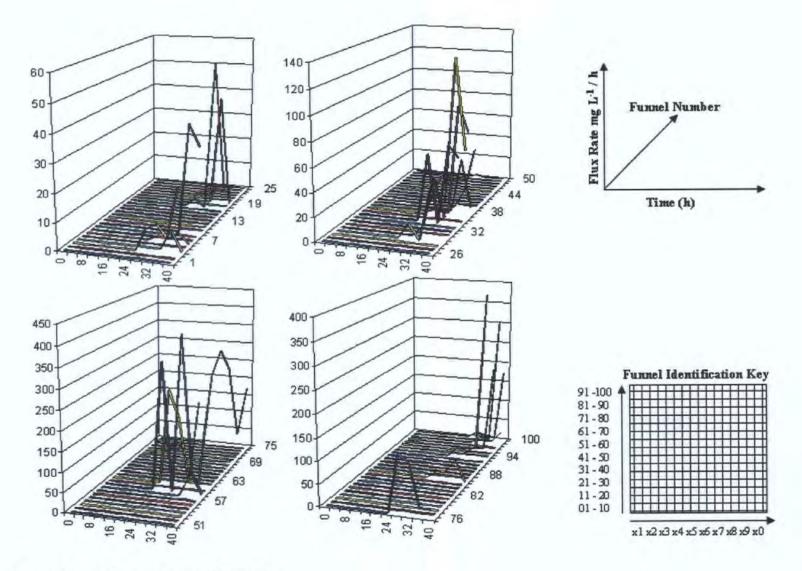
Figure I.7   Conway Bromide flux rates after oil injection
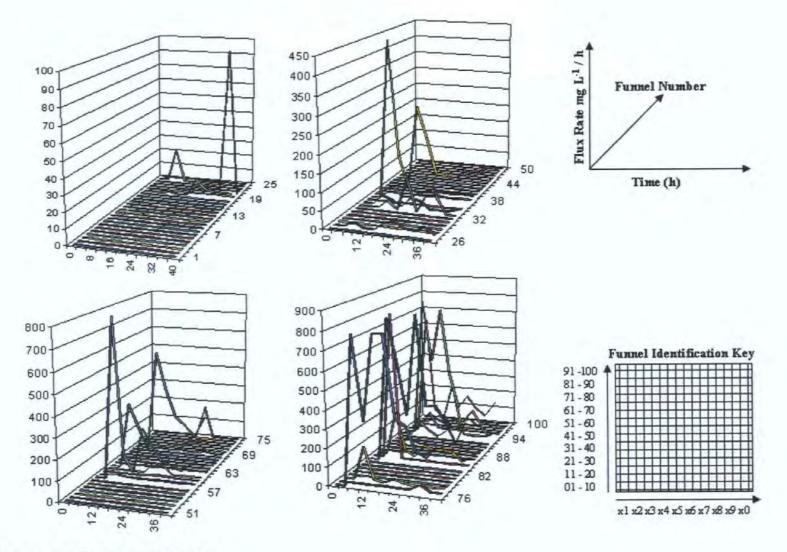
Figure I.8   Conway Bromide before Oil injection
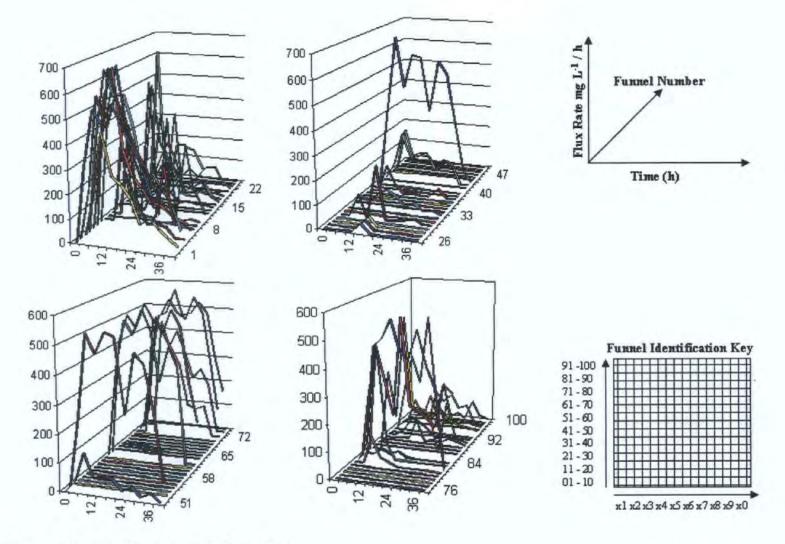
Figure I.9   Crediton Bromide distribution before oil injection
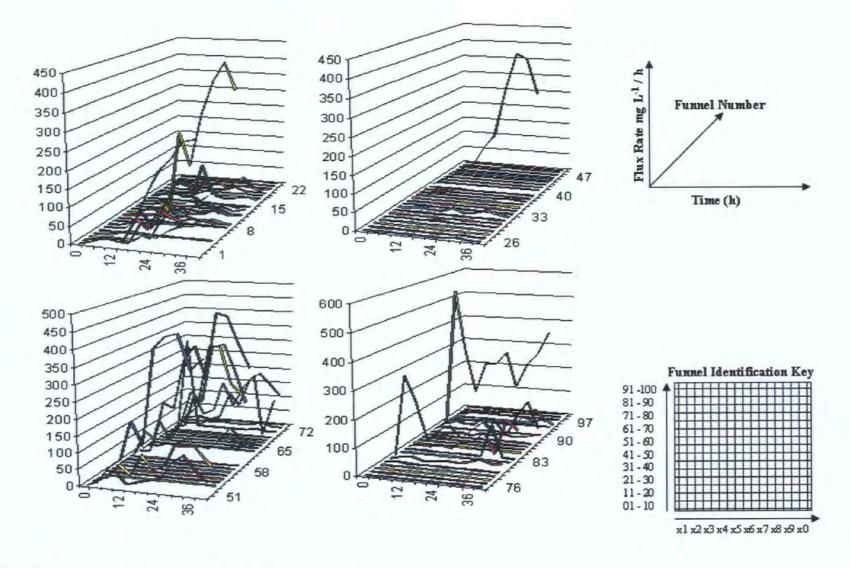
Figure I.10 Crediton Bromide breakthrough after oil Injection
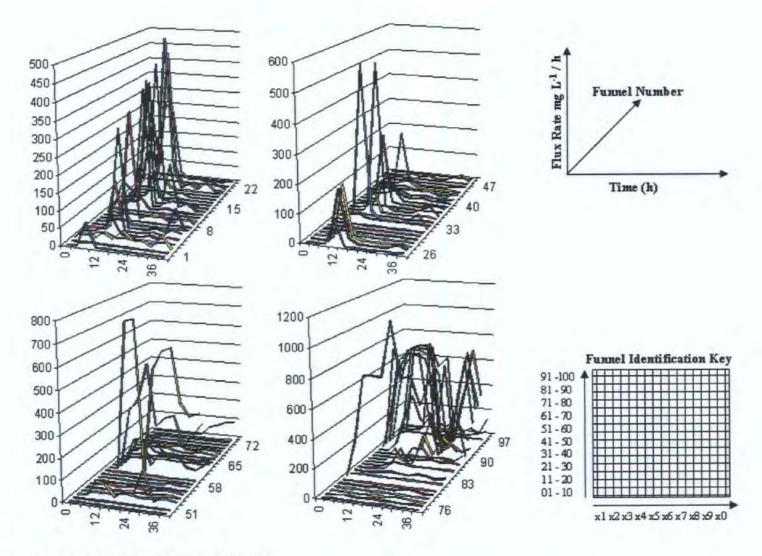
Figure I.11   Sollom bromide breakthrough before oil injection
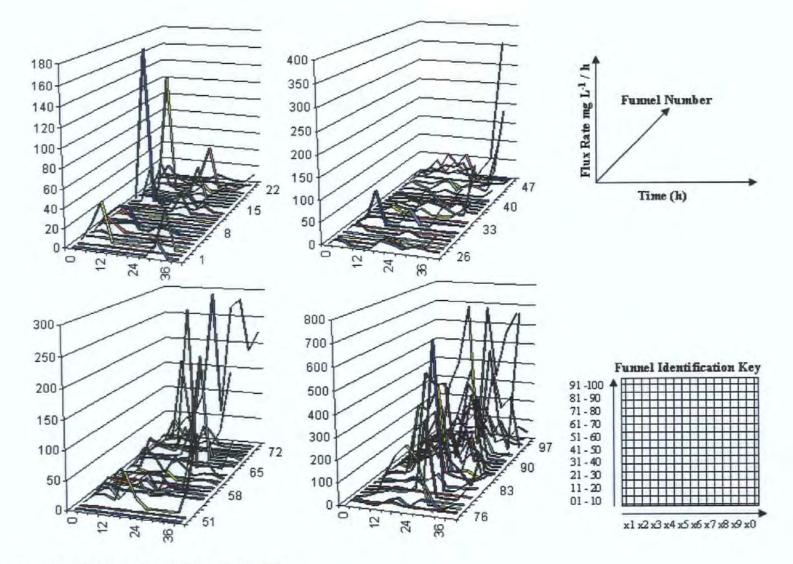
Figure I.12   Sollom bromide breakthrough after oil injection.
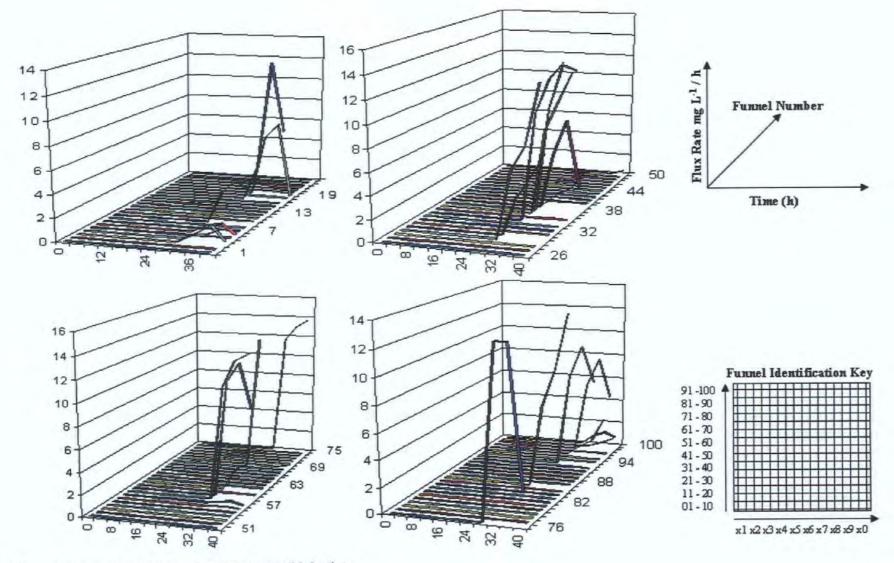
Figure I.13   Conway phosphate breakthrough post oil injection.
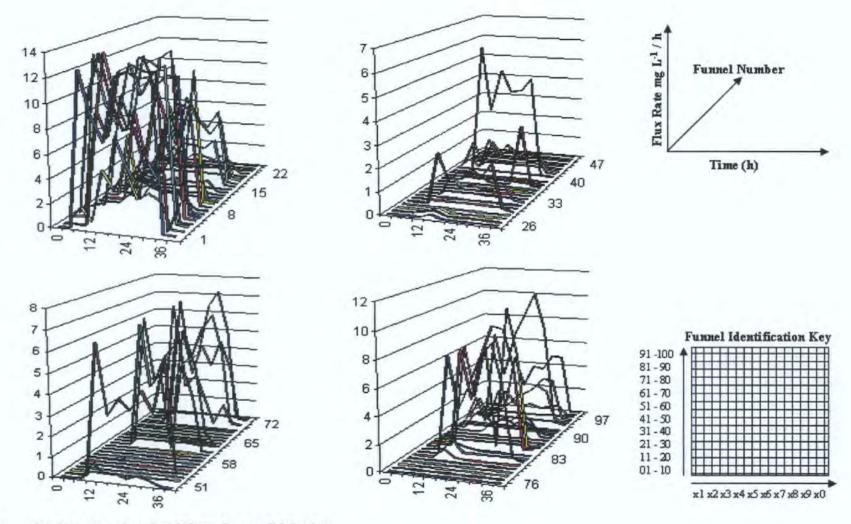
Figure I.14   Crediton phosphate breakthroughs pre oil injection.
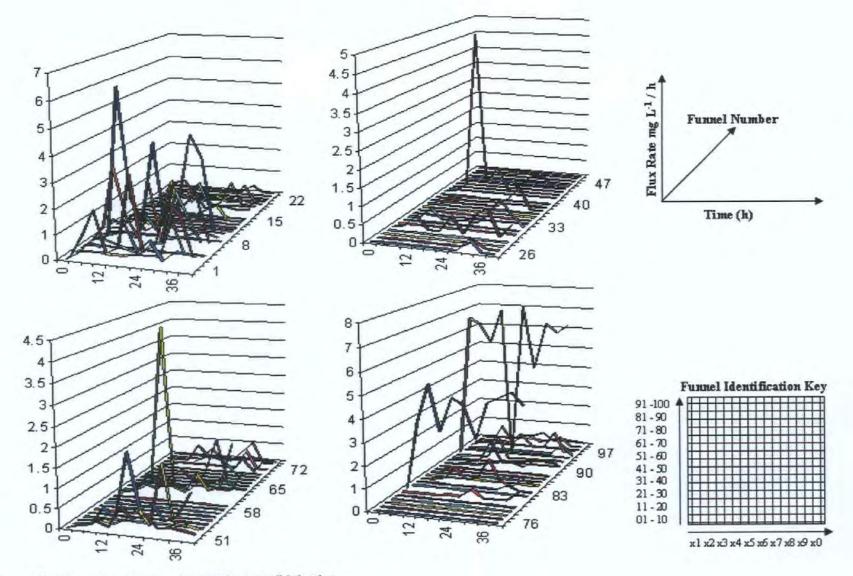
Figure I.15   Crediton phosphate breakthroughs post oil injection.
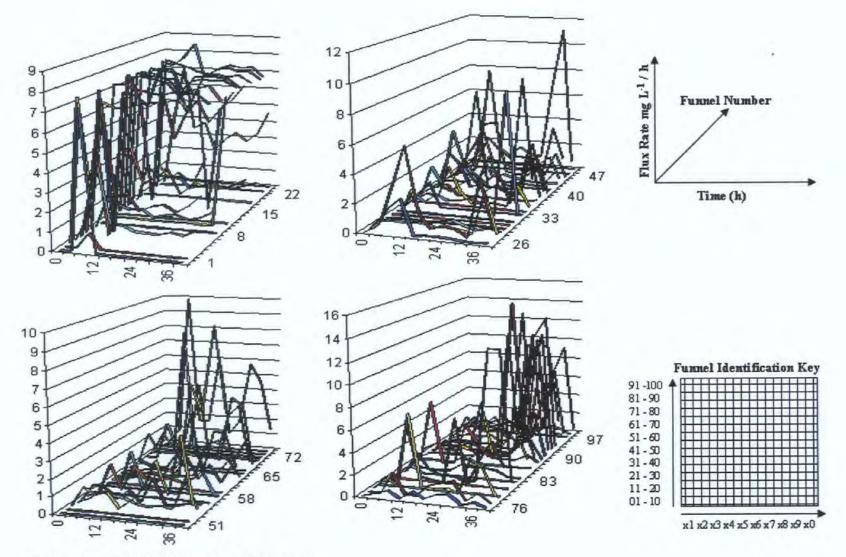
Figure I.16 Sollom phosphate breakthrough pre oil injection.
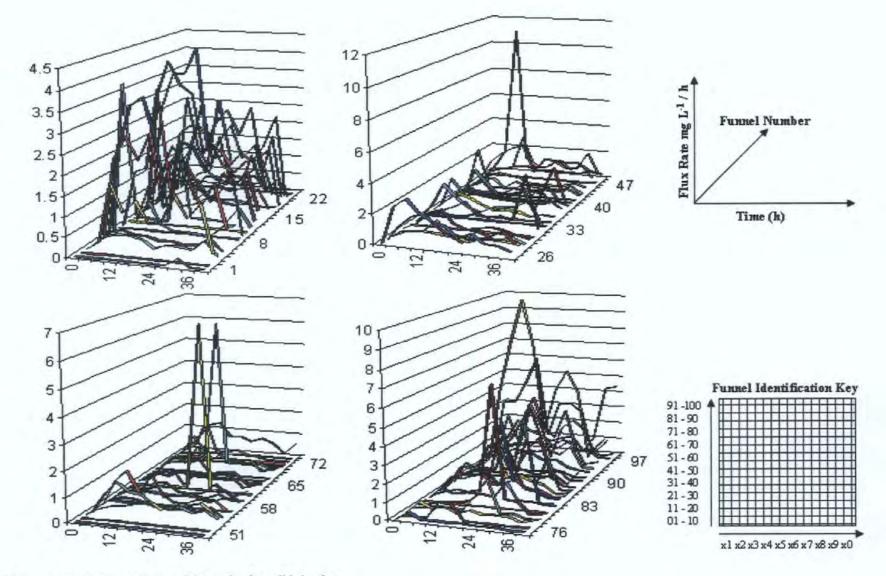
Figure I.17   Sollom phosphate breakthrough after oil injection

II. Appendix 2

Plotted on the following pages are the oil distributions described in Section 5.7, as plotted using the Visual Groundwater modelling package. The pictures are here enlarged to allow the reading of the contour values. The key as shown in Figure II.1 applies to all oil distribution diagrams, i.e. the value shown is either 85 or 100 DPM (disintegrations per minute).

100 DPM

85 DPM

Figure II.1   Key to oil Distributions DPM (Disintegrations Per Minute)

Figure II.2   Conway Oil Distribution Profile View.
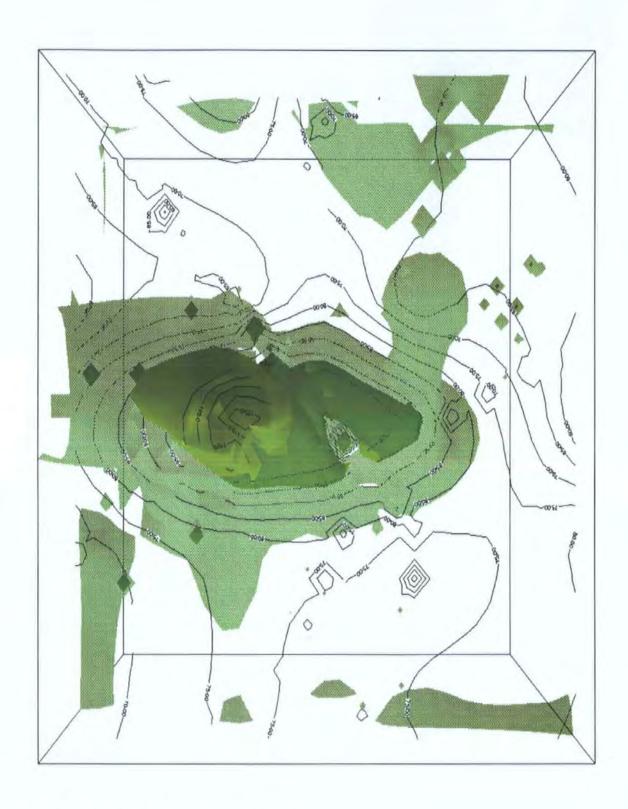
Figure II.3   Conway Oil Distribution Plan View.
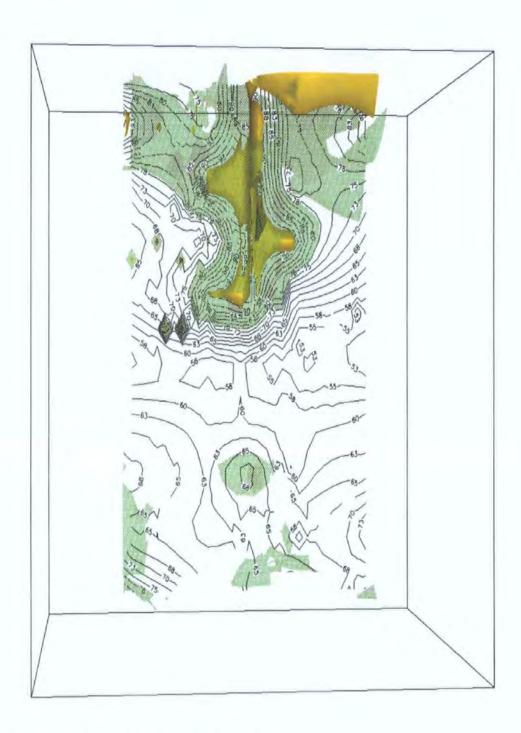
Figure II.4   **Crediton Oil Distribution Profile View.**
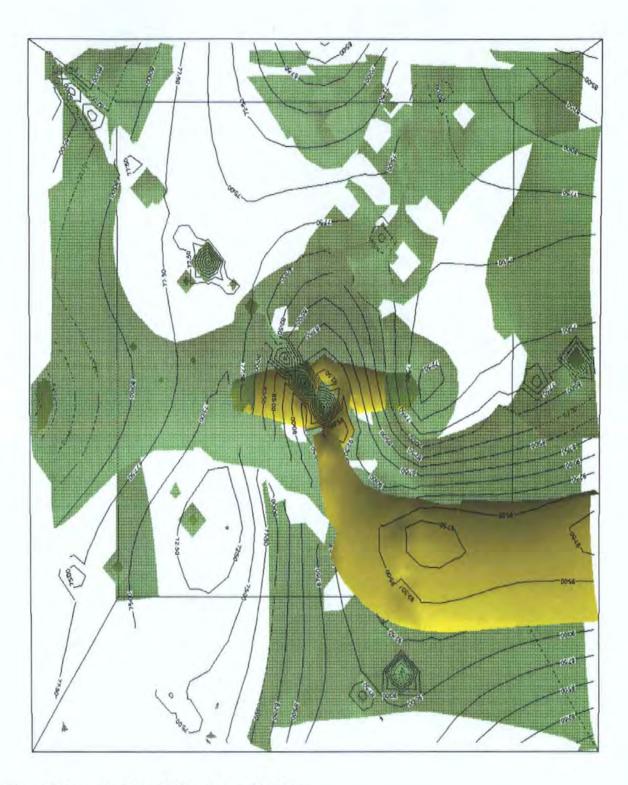
Figure II.5   **Crediton Oil Distribution Plan View.**

Figure II.6   Sollom Oil Distribution Profile View.
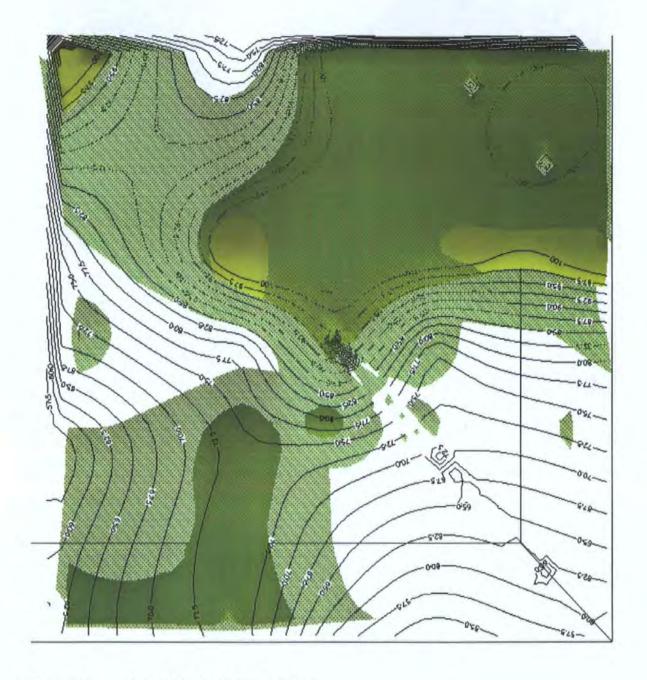
Figure II.7   Sollom Oil Distribution Plan View.

Reference List

Liquid flow in packed columns 3. Wall flows. Transactions of Institution of Chemical Engineers 46 (1968): 86-94.

Adler, P. M. and H. Brenner. "Transport processes in spatially periodic capillary networks .1. Geometrical description and linear flow hydrodynamics." Physicochemical Hydrodynamics 5 (1984): 245-68.

Ahmed,S.N.; Baldwin,R.; Derbyshire,F.; McEnaney,B.; Stencel,J. "Catalytic reduction of nitric-oxide over activated carbons." Fuel 72 (1993): 287-92.

Ahuja, R. K. , Kodialam, M., Mishra, A. K., and Orlin, J. B. "Computational investigations of maximum flow algorithms." European Journal Of Operational Research 97 (1997): 509-42.

American Public Health Association. Standard Methods for the Examination of Water and Wastewater. 14 ed. 1975.

Andreini, M. S. and T. S. Steenhuis. "Preferential paths of flow under conventional and conservation tillage." Geoderma 46 (1990): 85-102.

Armstrong, D.E., "Analytical Chemistry of Phosphorus Compounds.", Halmann, M. (Ed.) Wiley - Interscience, NY. (1972): 744.

Assouline, S., J. Tavares, and D. Tessier. "Effect of compaction on soil physical and hydraulic properties: experimental results and modeling." Soil Science Society Of America Journal 61 (1997): 390-98.

Baker, R. S. and D. Hillel. "Laboratory tests of fingering during infiltration into layered soils." Soil Science Society Of America Journal 54 (1990): 20-30.

Baskaran,S.; Bolan,N.S.; Rahman,A.; Tillman,R.W.; Macgregor,A.N. "Effect of drying of soils on the adsorption and leaching of phosphate and 2,4-dichlorophenoxyacetic acid." Australian Journal Of Soil Research 32 (1994): 491-502.

Batjes NH "Development of a world data set of soil water retention properties using pedotransfer rules", GEODERMA 71 (1-2): 31-52 MAY (1996)

Bernadiner, M. G. "A capillary microstructure of the wetting front." <u>Transport in Porous Media</u> 30 (1998): 251-65.

Beven, K and P Germann. "Macropores and water flow in soil." <u>Water Resources Research</u> 18.5 (1982): 1311-25.

Bewersdorff,A; Muller,G.; Oertel,H.; Sahm,P.R.; Sell,P-J.; Siekmann,J. "Zeitschrift fur flugwissenschaften und weltraumforschung." <u>Zeitschrift fur Flugwissenschaften und Weltraumforschung</u> 7.1 (1983): 1-7.

Biggar, J. W. and D. R. Nielsen. "Spatial variability of the leaching characteristics of a field soil." <u>Water Resources Research</u> 12.1 (1976): 78-84.

Bird, N. R. A., F. Bartoli, and A. R. Dexter. "Water retention models for fractal soil structures." <u>European Journal of Soil Science</u> 47.1 (1996): 1-6.

Bird, N. R. A. and A. R. Dexter. "Simulation of soil water retention using random fractal networks." <u>European Journal of Soil Science</u> 48 (1997): 633-41.

Bird, N. R. A., E. Perrier, and M. Rieu. "The water retention curve for a model of soil structure with Pore and Solid Fractal distributions. " <u>European J.Soil.Sci</u> 55 (2000): 55-63.

Birks, J. B. "An Introduction to Liquid Scintillation Counting". Boch-Light Laboratories Limited, 1974.

Bodurtha,P. "A Proposed system for the prioritisation of soil types susceptible to oil penetration." 2003, National Grid Transco, Project Concluding Report.

Bodurtha,P.,Matthews,G.P., Kettle,J.P., Roy,I.M. "The Influence of Structural Anisotropy on Fluid Permeation in Porous Media." May 2001, San Diego, USA: Tappi, 2001.

Bowman,B.T.; Brunke,R.R.; Reynolds,W.D.; Wall,G.J. "Rainfall simulator grid lysimeter system for solute transport studies using large, intact soil blocks." <u>Journal Of Environmental Quality</u> 23 (1994): 815-22.

Broberg, O. and Persson, G., <u>Hydrobiologia</u>. 170, (1988) 61.

Bronswijk, J. J. B., W. Hamminga, and K. Oostindie. "Field-scale solute transport in a heavy clay soil." Water Resources Research 31 (1995): 517-26.

Brooks, R. H. and A. T. Corey. "Hydraulic Properties of Porous Media." Hydrological Paper 3. Colorado State University, Fort Collins: Civil Engineering Department, 1964. 1.

Bryant, S. L., Mellor, D. W., and Cade, C. A., "Physically Representative Network Models of Transport in Porous Media", AIChE Journal 39, (1993): 387-396

Burganos, V. N. and A. C. Payatakes. "Knudsen Diffusion in Random and Correlated Networks of Constricted Pores." Chemical Engineering Science 47.6 (1992): 1383-400.

Butcher, J. B. and T. D. Gauthier. "Estimation of residual dense napl mass by inverse modeling." Ground Water 32 (1994): 71-78.

Butters, G. L., W. A. Jury, and F. F. Ernst. "Field scale transport of bromide in an unsaturated soil 1.Experimental methodology and results." Water Resources Research 25.7 (1989): 1575-81.

Butts, M. B. and K. H. Jensen. "Effective parameters for multiphase flow in layered soil." Journal Of Hydrology 183 (1996): 101-116.

Cameron, D. R. and A. Klute. "Convective dispersive solute transport with a combined equilibrium and kinetic adsorption model." Water Resources Research 13 (1977): 183-88.

Cheston, A. "Bioremediation of Joint Bays." Diss. Institute of Bioscience and Technology, 1997.

Chevalier, L. R. and J. Peterson. "Literature review of 2D laboratory experiments in NAPL flow, transport and remediation." Journal of Soil Contamination 8.1 (1999): 149-67.

Chow, Ven Te and T. E. Harbaugh. "Raindrop production for laboratory watershed experiments." Journal of Geophysical Research 70.24 (1965): 6111-19.

Chu, S. T. "Capillary-tube infiltration-model with brooks-corey parameters." <u>Transactions of the American Society of Agricultural Engineering</u> 37 (1994): 1205-08.

Cousin, I., P. Levitz, and A. Bruand. "Three-dimensional analysis of a loamy-clay soil using pore and solid chord distributions." <u>European Journal of Soil Science</u> 47 (1996): 439-52.

Crawford, J. W., N. Matsui, and I. M. Young. "The relation between the moisture-release curve and the structure of soil." <u>European Journal of Soil Science</u> 46 (1995): 369-75.

Daian, J. F. and J. Saliba. "Détermination d'un réseau aleatoire de pores pour modéliser la sorption et la migration d'humidité dans un mortier de ciment." <u>International Journal of Heat and Mass Transfer</u> 34.8 (1991): 2081-96.

Davis, J. L. and A. P. Annan. "Electromagnetic detection of soil moisture: Progress report I." <u>Canadian Journal of Remote Sensing</u> 3 (1977): 76-86.

Davis, J. L. and W. J. Chudobiak. "*In-situ* meter for measuring relative permittivity of soils." <u>Geological Survey of Canada</u> 75-1 (1975): 75-79.

Dawe, R. A., M. R Wheat, and Binder M.S. "Experimental investigation of capillary pressure effects on immiscible displacements in lensed and layered porous media." <u>Transport in Porous Media</u> 7 (1992): 83-101.

Day,M.; Parker,I.B.; Bell,J.; Thomas,M.; Fletcher,R.; Duffie,J. "Modelling of Mercury Intrusion and Extrusion". 1993, Amsterdam: Elsevier Science B.V., 1994.

Dekker, L. W. and C. J. Ritsema. "How water moves in a water repellent sandy soil 1. Potential and actual water repellency." <u>Water Resources Research</u> 30.9 (1994): 2507-17.

Dexter, A. R. "Heterogeneity of unsaturated, gravitational flow of water through beds of large particles." <u>Water Resources Research</u> 29.6 (1995): 1859-62.

Dinic E.A., "Algorithm for Solution of a Problem of Maximum Flow in networks with power estimation.", <u>Soviet Mathematics Doklady</u> 11, (1970): 1277-1280.

Dullien, F. A. L. <u>Porous Media. Fluid Transport and Pore Structure.</u> 2 ed. Academic Press, 1992.

Dullien, F. A. L. "Capillary effects and multiphase flow in porous media." <u>Journal of Porous Media</u> 1.1 (1998): 1-29.

Fatt, I. "The Network Model of Porous Media I. Capillary Pressure Characteristics." <u>Petroleum Transactions, AIME</u> 207 (1956): 144-81.

Fatt, I. "The network model of porous media II. Dynamic properties of a single size tube network." <u>Petroleum Transactions AIME</u> 207 (1956): 160-63.

Faust, C. R. "Transport of immiscible fluids within and below the unsaturated zone :A numerical model." <u>Water Resources Research</u> 21.4 (1985): 587-96.

Faust, C. R., J. H. Guswa, and J. W. Mercer. "Simulation of three dimensional immiscible fluids within and below the unsaturated zone." <u>Water Resources Research</u> 25.12 (1989): 2449-64.

Flury,M.; Flühler,H.; Jury,W.A.; Leuenberger,J. "Susceptibility of soils to preferential flow of water: A field study." <u>Water Resources Research</u> 30.7 (1994): 1945-54.

Fu,M; Chen G.; Davies,D.K.; Sutton,S.J.; Patel,D. "Use of fluorometry in the determination of DDB contamination in soils from underground oil-filled power cable leaks." <u>not known</u> (2000).

Garboczi, E. J. "Mercury Porosimetry and Effective Networks for Permeability Calculations in Porous Materials." <u>Powder Technology</u> 67.2 (1991): 121-25.

Garcia J.L.L., de Castro M.D.L., "Rapid analytical method for the determination of pesticide residues in sunflower seeds based on focused microwave-assisted Soxhlet extraction prior to gas chromatography-tandem mass spectrometry", <u>Journal of Chromatography B</u>, 993 (1-2), (2003): 121-129

Gardner,C.M.K.; Bell,J.P.; Cooper,J.D.; Dean,T.J.; Hodnett,M.G. "Soil Water Content." Ed. C. E. Mullins and K. A. Smith. New York: Marcel Decker, 1991. 1-73.

Gardolinski PCFC, Hanrahan G, Achterberg EP, Gledhill M, Ta:in AD, House WA, Worsfold PJ, "Comparison of sample storage protocols for the determination of nutrients in natural waters" Water Research, 35 (15), (2001): 3670-3678

Ghodrati, M. and W. A. Jury. "A field study using dyes to characterize preferential flow of water." Soil Science Society Of America Journal 54 (1990): 1558-63.

Gledhill, W. E., V. W. Saeger, and M. L. Trehy. "An aquatic environmental safety assessment of linear alkyl benzene." Environmental Toxicology and Chemistry 10 (1991): 169-78.

Hammel, K. and Roth, K., "Approximation of Asymptotic Dispersivity of Conservative Solute in Unsaturated Heterogeneous media with Steady State Flow", Water Resources Research 34, (1998): 709-715.

Harwood, J.E. and Hattingh, W.H. "Environmental Phosphorus Handbook.", Griffith, E.J., Beeton, A., Spencer, J.M., and Mitchell, D.T. (Eds.) (1974): 289.

Haygarth & Walley 2000. Personal communication on "Current methods of sealing soil cores".

Hendrickx, J. M. H., L. W. Dekker, and O. H. Boersma. "Unstable wetting fronts in water repellent field soils." Journal Of Environmental Quality 22 (1993): 109-18.

Hilfer, R. "Macroscopic equations of motion for two-phase flow in porous media." Physical Review E 58 (1998): 2090-96.

Hodnett M.G., Dasilva L.P., Darocha H.R., et al. "Seasonal soil-water storage changes beneath central amazonian rain-forest and pasture", Journal of Hydrology 170 (1-4) (1995): 233-254 Aug

Holden, N. M., Dowd, J. F., Williams, A. G., and Scholefield, D., "Computer Control for Investigating Water and Chemical Transport in a Large Isolated Soil Block", Computers and Electronics in Agriculture 12, (1995): 225-236

Horvath, Y., "The use of TDR probes in soil", Personal Communication, (2000)

Host-Madsen, J. and K. Hogh Jensen. "Laboratory and numerical investigations of immiscible multiphase flow in soil." Journal Of Hydrology 135 (1992): 13-52.

Hunter & Goldspink 1956 – Unknown from a paper supplied courtesy of Skalar Analytical.

Illangasekare, T. H., E. J. Armbruster, and D. N. Yates. "Non-aqueous-phase fluids in heterogeneous aquifers-experimental study." <u>ASCE, Journal of Environmental Engineering Division</u> 121.8 (1995): 571-79.

Isensee A.R. and Sadeghi A.M., "Laboratory Apparatus for Studying Pesticide Leaching in Intact Soil Cores", <u>Chemosphere</u> 25(4), (1992): 581-590.

Jalbert M, Dane JH, Bahaminyakamwe L "Influence of porous medium and NAPL distribution heterogeneities on partitioning inter-well tracer tests: a laboratory investigation" <u>Journal of Hydrology</u> 272 (1-4): 79-94 MAR 10 2003

Johnson,A.; Matthews, T.; Matthews,G.P.; Worsfold,P.J.; Patel,D.; Andrew,K.N. "High-resolution laboratory lysimeter for automated sampling of tracers through a 0.5M soil block." <u>Journal of Automated Methods and Management in Chemistry</u> 25.2 (2003): 43-49.

Johnson A, Roy IM, Matthews GP, Patel,D "An improved simulation of void structure, water retention and hydraulic conductivity in soil with the Pore-Cor three-dimensional network" <u>European Journal of Soil Science</u> 54 (3) (2003): 477-489

Keuper, B. H., W. Abbott, and G. R. Farquhar. "Experimental observations of multiphase flow in heterogeneous porous media." <u>Journal of Contaminant Hydrology</u> 5 (1989): 83-95.

Kosugi, K. "Three-parameter lognormal distribution model for soil-water retention." <u>Water Resources Research</u> 30.4 (1994): 891-901.

Kung, K.-J. S. "Preferential flow in a sandy vadose zone; 1. Field observation." <u>Geoderma</u> 46 (1990a): 51-58.

Kung, K.-J. S. "Preferential flow in a sandy vadose zone: 2. Mechanism and implications." <u>Geoderma</u> 46 (1990b): 59-71.

Lark R.M., Webster R,"Changes in variance and correlation of soil properties with scale and location: analysis using an adapted maximal overlap discrete wavelet transform" <u>European Journal of Soil Science</u> 52 (4), (2001): 547-562.

Lark R.M., Webster R, "Analysis and elucidation of soil variation using wavelets", <u>European Journal of Soil Science</u> 50 (2), Jun (1999):185-206.

Lenormand, R., E. Touboul, and C. Zarcone. "Numerical models and experiments on immiscible displacements in porous media." Journal of Fluid Mechanics 189 (1988): 165-87.

Letniowski, F. W. "Numerical Methods for NAPL Groundwater Contamination in Three Dimensions." Diss. Master of Math. Thesis, University of Waterloo, Waterloo, Ont., 1989.

Leverett, M. C. "Capillary behaviour in porous solids." Transaction of the American Institute of Mining and Metallogy Engineering 142 (1941): 152-69.

Lewis T.E., Blasdell B, Blume L.J., "Collection of Intact Cores from a Rocky Desert and a Glacial Till Soil", Soil Science Society of America Journal, 54(3), (1990): 938-940.

Ma, S. X., G. Mason, and N. R. Morrow. "Effect of contact angle on drainage and imbibition in regular polygonal tubes." Colloids And Surfaces A-Physicochemical And Engineering Aspects 117 (1996): 273-91.

Maher W, Woo L, "Procedures for the storage and digestion of natural waters for the determination of filterable reactive phosphorus, total filterable phosphorus and total phosphorus", Analytica Chemica Acta, 375 (1-2), (1998): 5-47

Mathews, T. J. and G. P. Matthews. "Discriminatory water and tracer flow in homogeneous repacked sand." Water Resources Research (1999).

Matthews,G.P.; Moss,A.K.; Spearing,M.C.; Voland,F. "Network Calculation of Mercury Intrusion and Absolute Permeability in Sandstone and Other Porous Media." Powder Technology 76.1 (1993): 95-107.

Mayr, T and N. J. Jarvis. "Pedotransfer functions to estimate soil water retention parameters for a modified Brooks-Corey type model." Geoderma 91 (1999): 1-9.

Mercer, J. W. and R. M. Cohen. "A review of immiscible fluids in the subsurface: Properties, models, characterisation and remediation." Journal Of Contaminant Hydrology 6 (1990): 107-63.

Miyazaki, T. "Preferential Flow." New York: Marcel Dekker, 1993. 93-121.

Mualem, Y. "A new model for the predicting the hydraulic conductivity of unsaturated porous media." Water Resources Research 12.3 (1976): 513-22.

Murphy, J. and Riley, J. P. Analytica Chimica Acta. 27, (1962): 1.

Nelder, J. A. and R. Mead. "A simplex method for function optimisation." Computer Journal 7 (1965): 308-13.

Nemes A., Schaap M.G., Leij F.J., Wosten J.H.M., "Description of the unsaturated soil hydraulic database UNSODA version 2.0", Journal of Hydrology, 251 (3-4), (2001): 151-162

Nicholl,M.J.; Wheatcraft,S.W.; Tyler,S.W.; Berkowitz,B. "Is old faithful a strange attractor." Journal Of Geophysical Research-Solid Earth 99 (1994): 4495-503.

Nielsen, D.R. and Biggar, J.W., Erh, K.T., "Spatial Variability of Field-Measured Soil Water Properties", Hilgardia 42, (1973): 215-259.

Osborne, M. and J. Sykes. "Numerical Modelling of Immiscible Organic Transport at the Hyde Park Landfill." Water Resources Research 22.1 (1986): 25-33.

Pantazidou, M. and N. Sitar. "Emplacement of nonaqueous liquids in the vadose zone." Water Resources Research 29 (1993): 705-22.

Parker, J. C., Katyal, A. K., Kaluarachchi, J. J., Lenhard, R. J., Johnson, T. J., Jayaraman, K., Unlu, K., and Zhu, J. L. Modelling multiphase organic chemical transport in soils and groundwater. 1991. EPA/600/2-91/042.

Parker, J. C., R. J. Lenhard, and T. Kuppusamy. "A parametric model for constitutive properties governing multiphase flow in porous media." Water Resources Research 23.4 (1987): 618-24.

Peat,D.M.W.; Matthews,G.P.; Worsfold,P.J.; Jarvis,S.C. "Simulation of water retention and hydraulic conductivity in soil using a three-dimensional network." European Journal of Soil Science 51.1 (2000): 65-79.

Perrier, E., N. Bird, and M. Rieu. "Generalizing the fractal model of soil structure: the pore- solid fractal approach." Geoderma 88.3-4 (1999): 137-64.

Perrier E, Mullon C, Rieu M, et al. "Computer construction of fractal soil structures: Simulation of their hydraulic and shrinkage properties" WATER RESOUR RES 31 12: 2927-2943 DEC (1995).

Pinder, G. F. and Abriola, L. M., "On the Simulation of Non Aqueous Phase Organic Compounds", Water Resources Research, 22, (1986): 109-119

Porter, K. E. "Liquid flow in packed columns 1. The rivulet model." Transactions of Institution of Chemical Engineers 46 (1968): 69-73.

Porter, K. E., V. D. Barnet, and J. J. Templeman. "Liquid flow in packed columns 2. The spread of liquid over random packings." Transactions of Institution of Chemical Engineers 46 (1968): 74-85.

Poulsen, M. M. and B. H. Keuper. "A Field Experiment to Study the Behaviour of Tetrachloroethylene in Unsaturated Porous Media." Environmental Science and Technology 26.5 (1992): 889-95.

Press, W. H. and S. A. Teukolsky. "Simulated Annealing Optimization Over Continuous Spaces." Computers in Physics (1991): 426-29.

Raats, P. A. C. "Unstable wetting fronts in uniform and nonuniform soils." Soil Science Society Of America Journal 37 (1973): 681-85.

Rajaram, H., Ferrand, L. A., and Celia, M. A., "Prediction of Relative Permeabilities for Unconsolidated Soils Using Pore-Scale Network Models", Water Resources Research, 33, (1997): 43-52

Rappoldt, C. "The Application of Diffusion Models to an Aggregated Soil." Soil Science 150.3 (1990): 645-61.

Rawls, W. J., D. L. Brakensiek, and S. D. Logsdon. "Predicting saturated hydraulic conductivity utilizing fractal principles." Soil Science Society Of America Journal 57 (1993): 1193-97.

Rawls, W. J., D. L. Brakensiek, and K. E. Saxton. "Estimation of soil-water properties." Transactions Of The Asae 25 (1982): 1316.

Rege, S. D. and H. S. Fogler. "Network model for straining dominated particle entrapment in porous- media." Chemical Engineering Science 42 (1987): 1553-64.

Rieu, M., & Sposito G., "Fractal fragmentation, soil porosity, and soil water properties: I. Theorey; II. Applications.", <u>Soil Science Society of America Journal</u>, 55 (1991): 1231-1244.

Rimmer,A.; DiCarlo,D.A.; Steenhuis,T.S.; Bierck,B.; Durnford,D.; Parlange,J.Y. "Wetting and nonwetting fluid displacements in porous media." <u>Transport in Porous Media</u> 25 (1996): 205-15.

Romkens,M.J.M.; Glenn,L.F.; Nelson,D.W.; Roth,C.B. "A laboratory rainfall simulator for infiltration and soil detachment studies." <u>Soil Science Society of America Proceedings</u> 39 (1975): 158-60.

Roth,K.; Schulin,R.; Fluhler,H.; Attinger,W. "Calibrationof time domain reflectometry for water content measurement using a composite dielectric approach." <u>Water Resources Research</u> 26.10 (1990): 2267-73.

Rowland, S. J. "Chemical Characterisation of Cable Oil". 1996. University of Plymouth, PEP Research and Consultancy Limited.

Schafer, R. L. et al. "Future research needs in soil compaction." <u>Transactions Of The Asae</u> 35 (1992): 1761-70.

Scheidegger, A. E. <u>The Physics of Flow Through Porous Media</u>. Toronto: University of Toronto Press, 1974.

Schiegg, H. O. Laboratory setup and results of experiments on two dimensional multiphase flow in porous media. Mcbride, J. F. and Graham, D. N. DE-AC06-76RLO1830, 1-423. 1990. Washington, DC, US Department of Energy. 1990.

Schlicting, H. <u>Boundary Layer Theory</u>. New York: McGraw-Hill, 1979.

Schoelkopf,J.; Gane,P.A.C.; Ridgway,C.J.; Matthews,G.P. "Influence of Inertia on Liquid Absorption into Paper Coating Structures." <u>Nordic Pulp and Paper Research Journal</u> 15.5 (2001): 422-30.

Schroth, M., Istok, J. D., Ahearn, S. J., and Selker, J. S., "Geometry and Position of Light Nonaqueous-Phase Liquid Lenses in Water-Wetted Porous-Media", <u>Journal Of Contaminant Hydrology</u>, 19, (1995): 269-287

Schwille, f. "Petroleum Contamination of the Subsoil - A Hydological Problem, the Migration of Hydrocarbons in a Water Bearing Stratum." Ed. P. Hepple. New York: American Elsevier, 1967. 23-54.

Schwille, f. "Dense chlorinated solvents in porous and fractured media: model experiments." unknown (1988).

Selker, J. S., J. F. Duan, and J. Y. Parlange. "Green and Ampt infiltration into soils of variable pore size with depth." Water Resources Research 35.5 (1999): 1685-88.

Sharma, M. M. and Y. C. Yortsos. "A network model for deep bed filtration processes." Aiche Journal-American Institute Of Chemical Engineers 33 (1987): 1644-53.

Simmons, C. S., McBride, J. F., Cary, J. W., and Lenhard, R. J., "Organic Liquid Infiltration into Unsaturated Porous Media", Subsurface Contamination by Immiscible Fluids Balkema, Rotterdam, (1992) :213-219

Smith, K. A. and Mullins, C. E. Soil Analysis: Physical Methods. 45-55. 1991. New York, Marcel Dekker Inc.

Sorbie, K. S. and P. J. Clifford. "The inclusion of molecular-diffusion effects in the network modeling of hydrodynamic dispersion in porous-media." Chemical Engineering Science 46 (1991): 2525-42.

Spearing M, Matthews G.P., "Modeling Characteristic Properties of Sandstones", Transport in Porous Media, 6 (1991): 71-90.

Sukop M.C., Perfect E., Bird N.R.A., "Water retention of prefractal porous media generated with the homogeneous and heterogeneous algorithms", Water Resources Research 37 (10): 2631-2636 OCT (2001).

Swisher, R. D., E. F. Kaeble, and S. K. Liu. "Capillary gas chromatography of phenyl dodecane alkylation and isomeration mixtures." Journal of Organic Chemistry 26 (1961): 4066.

Talsma, T. "Prediction of hydraulic conductivity from soil-water retention data." Soil Science 140 (1985): 184-88.

Templeton, C. "A study of displacements in microscopic capillaries." Petroleum Transactions AIME 201 (1954): 162-68.

Thompson, P. A. and S. M. Troian. "A general boundary condition for liquid flow at solid surfaces." Nature 389 (1997): 360-62.

Tietje O, Hennings V, "Accuracy of the saturated hydraulic conductivity prediction by pedo-transfer functions compared to the variability within FAO textural classes" GEODERMA 69 (1-2), Jan (1996): 71-84.

Tindall J.A., Hemmen K., and Dowd J.F., "An Improved Method for Field Extraction and Laboratory Analysis of Large, Intact Soil Cores", Journal of Environmental Quality, 21 (2), (1992): 259-263.

Tomasella J, Hodnett MG, Rossato L, "Pedotransfer functions for the estimation of soil water retention in Brazilian soils" SOIL SCI SOC AM J 64 (1): 327-338 JAN-FEB (2000)

Tomasella J, Hodnett MG, "Estimating soil water retention characteristics from limited data in Brazilian Amazonia", SOIL SCI 163 (3): 190-202 MAR (1998)

Topp, G. C., J. L. Davis, and A. P. Annan. "Electromagnetic determination of soil water content: Measurements in coaxial transmission lines." Water Resources Research 16.3 (1980): 574-82.

Tsakiroglou, C. D. and A. C. Payatakes. "A New Simulator of Mercury Porosimetry for the Characterisation of Porous Materials." J.Coll.Int.Sci. 137.2 (1990): 315-39.

Van den Berg M., Klamt E., vanReeuwijk L.P., Sombroek W.G.,"Pedotransfer functions for the estimation of moisture retention characteristics of Ferralsols and related soils", Geoderma, 78 (3-4): 161-180 AUG 1997

van Geel, P. L. and J. F. Sykes. "Laboratory and model simulations of a LNAPL spill in a variably saturated sand. I. Laboratory experiments and image analysis techniques." Journal Of Contaminant Hydrology 17 (1994): 1-25.

van Geel, P. L. and J. F. Sykes. "The importance of fluid entrapment, saturation hysteresis and residual saturation on the distributions of a lighter-than-water non-aqueous phase liquid in a variably saturated sand medium." Journal Of Contaminant Hydrology 25 (1997): 249-70.

van Genuchten, M. Th. "A closed-form equation for predicting the hydraulic conductivity of unsaturated soils." Soil Science Society Of America Journal 44 (1980): 892-98.

van Genuchten, M. Th. And Wierenga, P.J., "A closed-form equation for predicting the hydraulic conductivity of unsaturated soils." Soil Science Society Of America Journal 40, (1976): 473-480.

Vangeel, P. J. and J. F. Sykes. "Laboratory and model simulations of a lnapl spill in a variably- saturated sand .1. laboratory experiment and image-analysis techniques." Journal Of Contaminant Hydrology 17 (1994): 1-25.

Vogel, H.J. and Roth K., "Moving Through Scales of Flow and Transport in Soil", Journal of Hydrology 272, (2003): 95-106.

Whalley, W. R. "Considerations on the use of time-domain reflectometry (TDR) for measuring soil water content." Journal of Soil Science 44 (1993): 1-9.

Wopereis,M.C.S.; Kropff,M.J.; Wosten,J.H.M.; Bouma,J. "Sampling strategies for measurement of soil hydraulic-properties to predict rice yield using simulation-models." Geoderma 59 (1993): 1-20.

Wosten, J. H. M., P. A. Finke, and M. J. W. Jansen. "Comparison of class and continuous pedotransfer functions to generate soil hydraulic characteristics." Geoderma 66 (1995): 227-37.

Copyright Statement

This copy of the thesis has been supplied on condition that anyone who consults it is understood to recognise that its copyright rests with its author and that no quotation from the thesis and no information derived from it may be published without the author's prior consent.

Signed..............................

17 Dec 2004.

Anthony Johnson, September 2004